RESOLVING THE THROUGH-GOING ACTIVE FAULT GEOMETRY AND FAULT STRENGTH PARAMETERS THROUGH STRESS MODELING: A STUDY OF THE NORTH ANATOLIAN FAULT (NAF)

by

Bobak Karimi

BS, University of Pittsburgh, 2008

Submitted to the Graduate Faculty of

the Kenneth P. Dietrich School of Arts & Sciences in partial fulfillment

of the requirements for the degree of

Doctor of Philosophy

University of Pittsburgh

2014

UNIVERSITY OF PITTSBURGH

Kenneth P. Dietrich School of Arts & Sciences

This dissertation was presented

by

Bobak Karimi

It was defended on

July 15th, 2014

and approved by

Jeen-Shang Lin, Associate Professor, Civil & Environmental Engineering

William Harbert, Professor, Geology & Planetary Science

Brian Stewart, Associate Professor, Geology & Planetary Science

Thomas Anderson, Professor Emeritus, Geology & Planetary Science

Dissertation Advisor: Nadine McQuarrie, Assistant Professor, Geology & Planetary Science

RESOLVING THE THROUGH-GOING ACTIVE FAULT GEOMETRY AND FAULT STRENGTH PARAMETERS THROUGH STRESS MODELING: A STUDY OF THE NORTH ANATOLIAN FAULT (NAF)

Bobak Karimi, PhD

University of Pittsburgh, 2014

RESOLVING THE THROUGH-GOING ACTIVE FAULT GEOMETRY AND FAULT STRENGTH PARAMETERS THROUGH STRESS MODELING: A STUDY OF THE NORTH ANATOLIAN FAULT (NAF)

Bobak Karimi, PhD

University of Pittsburgh, 2014

The North Anatolian Fault (NAF) was the source of the August 1999 M7.4 Izmit earthquake making it the focus of new research to understand its structure and processes that control earthquake ruptures. The zone of deformation (NAF system) widens westward, allowing for complications of the through-going active fault geometry of the NAF. We process simplified 2-D finite element models of possible through-going active fault geometries to develop a stress field. The stress orientations of the resulting field are compared to the maximum horizontal stress orientation as inferred from lineament analyses and focal mechanism data. The determined through-going geometry of the western NAF bifurcates into a northern and southern strand near Bolu, converging towards the Mudurnu Valley, through which they are linked. The northern strand bifurcates again in the Gulf of Izmit and bounds a principal deformation zone associated with the developing Marmara basin. It then converges as a single strand into the Gulf of Saros and the Aegean Sea. The southern strand bifurcates near Pamukova; its northern component follows the southern Marmara Sea coast to the Kapidag Peninsula, where it trends southwest across the Biga Peninsula into the Aegean Sea. The southern trace parallels the northern trace further south, and then converges on the northern trace through a linking structure.

To understand fault strength and constrain ranges of static and dynamic fault parameters, modeled fault rupture times and total slip are compared against recurrence intervals, as a proxy for the time it takes stress to rupture a fault from a relaxed state, and the maximum slip following the 1999 Izmit earthquake. We constrained values of static fault parameters - static coefficient of friction (μ_s) and cohesion (C) - and dynamic fault parameters - kinetic coefficient of friction (μ_k) and slip-weakening distance (D_c) - that satisfy the geologic constraints. Given the computationally expensive processing associated with dynamic fault models, we suggest the application of statically weak fault conditions ($\mu_s \leq 0.2$ and C=500 kPa) since they best represent laboratory experiments on the strength of fault gouge materials.

TABLE OF CONTENTS

LIST OF TABLES

LIST OF FIGURES

LIST OF EQUATIONS

ACKNOWLEDGEMENTS

This work would not have been possible without the guidance, support, and dedication of my dissertation advisor, Dr. Nadine McQuarrie, and my committee members, Dr. Jeen-Shang Lin, Dr. William Harbert, Dr. Brian Stewart, and Dr. Thomas Anderson. I cannot thank them enough for participating as mentors for my graduate journey. I thank Dr. Michael Ramsey for providing me with satellite imagery and insight on remote sensing techniques, and Drs. Alison Graettinger, Rachel Lee, and Topher Hughes for their time and support. A special thanks is extended to my colleagues, especially Daniel Williams, Charlie Horowitz, and lab mates Michelle Gilmore and Adam Rak. I would like to thank my friends, who helped me remember there was a real world outside of my research and helped to calm my nerves: Ida Chavoshan, Drew Wnuk, Julianna Allen, and Andrew Topp. My family deserves one of the biggest thanks I can give for supporting me through all the ups and downs that come with getting a graduate degree, especially my father and mother for their insight and rational thinking. Finally, I would like to extend thanks to the Computational Infrastructure for Geodynamics (CIG) listserv, colleagues at Geo Forschungs Zentrum (GFZ), and the PittGrid Network.

1.0 INTRODUCTION

The North Anatolian Fault (NAF) shares many similarities with the San Andreas Fault (SAF), such as age, slip rate, geometry, and length (Allen, 1982). However, a major difference is that the NAF produces more high-magnitude earthquakes (M>5) than the SAF (Allen, 1982). The NAF is the source for several devastating and high magnitude earthquakes in Turkey, particularly east of, and along, the northern boundary of the Marmara Sea (Bohnhoff et al., 2013; Parsons, 2004), which is densely populated and highly industrialized. The 1999 earthquake sequence of August 17th, located in the eastern Marmara region near Izmit, was initiated by a M_w 7.4 earthquake (Stein et al., 1997). This earthquake was one of the strongest earthquakes in Turkey detected by modern digital networks (Özalaybey et al., 2002) with a devastating death toll of over 17,000 people (Scawthorn and Johnson, 2000). This event has become the impetus for various new research activities in the Marmara region to understand the active structure and kinematics of the NAF, which are vital in assessing the seismic hazard along the NAF (Armijo et al., 2002; Ates et al., 2003; Hergert and Heidbach, 2010, 2011; Hergert et al., 2011; Hubert-Ferrari et al., 2000; Le Pichon et al., 2003; Le Pichon et al., 2001; Okay et al., 2000; Parsons, 2004). Additionally, fault strength plays an important role on the magnitude and timing of stress accumulation during interseismic periods, ultimately affecting the timing of rupture, recurrence, and magnitude of earthquakes.

The geometry of faults strongly influences the orientations and magnitudes of both stress and strain, metrics that are critical for modeling earthquake recurrence intervals and determining seismic hazards. A critical means towards understanding the links between the structure, or

geometry, of faults and the resulting stress and strain fields is through stress modeling paired with comparisons to data that record stress (Bilham and King, 1989; Lesne et al., 1998). Fault strength, which greatly affects the timing and magnitude of earthquakes, can also be explored through stress modeling by comparing resulting stress fields to a record of known stresses pre-, syn-, or post-seismic event (Chang et al., 2011; Chéry et al., 2004; Hergert and Heidbach, 2011). Alternatively, the kinematic aspects of models, such as the slip rates and magnitudes of faults or velocities of tectonic blocks can be compared to known values to constrain metrics for the strength of the fault (Jiménez-Munt et al., 2006; Kasapoglu and Toksöz, 1983; Provost et al., 2003). In this dissertation I constrain both the active fault geometry and fault strength of the NAF to provide more accurate input in future seismic hazard models. Half of my dissertation involves resolving the through-going geometry of the active NAF by comparing results from modeled stress fields to a record of stresses (Chapters 2 and 5). In Chapter 2, I discuss the interpretation of the active structure of the NAF east of the Marmara Sea and west of the city of Bolu. In Chapter 5, I address the active NAF structure in the Marmara Sea and Biga Peninsula and present the determined geometry for the entire western NAF for use in geophysical models to evaluate seismic hazard. In the second half of my dissertation I evaluate and explore the strength of the NAF through the use of stress models with comparison between modeled rupture times and total fault slip to those determined for the geologic record (Chapter 3 and 4). In Chapter 3, I constrain and analyze the estimates for static fault conditions, which must be overcome by the developing stress field for the fault to slip. In Chapter 4, I constrain the estimates for dynamic fault parameters that weaken the fault interface after slip has begun and explore fault weakness mechanisms for the NAF. Although both Chapters 2 and 5 evaluate fault geometry, the order of the chapters allows me to use the fault strength parameters determined in

Chapters 3 and 4 to more accurately model the stress field along the greater NAF system in Chapter 5. The introduction chapter (Chapter 1) provides a description of the NAF and its tectonic environment and well as an overview of the data that provide records of stress. I discuss how these data are compared and used to evaluate the modeled stresses in determining fault geometry (section 1.2) and fault strength (section 1.3).

1.1 THE NORTH ANATOLIAN FAULT

The NAF is a 1200 km fault contained within a dextral shear zone (known as the NAF system) paralleling the southern shore of the Black Sea (Şengör, 1979; Şengör et al., 2005). The NAF system is contained within westward-widening late Paleozoic to early Tertiary Tethyan accretionary complexes trapped between the Eurasian and Anatolian plates (Şengör, 1979; Şengör and Natal'in, 1996; Şengör et al., 2005). The sediments of these complexes were deposited during the open phases of the Paleo-Tethys and Neo-Tethys oceans, and were accreted during the Cimmeride and Alpide orogenies (Şengör et al., 2005). In Turkey, the two orogenies are treated as indistinct from one another due to the extreme dismemberment and width reduction of these accretionary complexes (Şengör et al., 2005). The relative weakness of the westward-widening accretionary complexes to the stronger Eurasian and Anatolian plates allows the plates to decouple along the NAF system. The shear zone broadens across the northern Aegean Sea into the southern and central mainland parts of Greece (the Grecian Shear Zone) (Şengör, 1979; Şengör and Natal'in, 1996) terminating at the Hellenic subduction zone (Dewey and Şengör, 1979; McKenzie and Jackson, 1983) (Figure 1.1). Due to the broad nature of the shear zone just west of the town of Bolu, the through-going NAF bifurcates into two main strands: a northern

strand bordering the northern shores of the Marmara Sea, and a poorly-defined southern strand, which trends towards the southern Marmara Sea edge (Şengör et al., 2005) (Figure 1.2). Analyses of basins resulting from pull-apart or negative flower structure associated with jogs or stepovers of the NAF and its strands west of Bolu provide an age for the NAF; the eastern through-going NAF structure initiated approximately 10-12 Ma, contemporaneously with the southern strand, whereas the northern strand formed in the Pleistocene (Şengör et al., 2005).

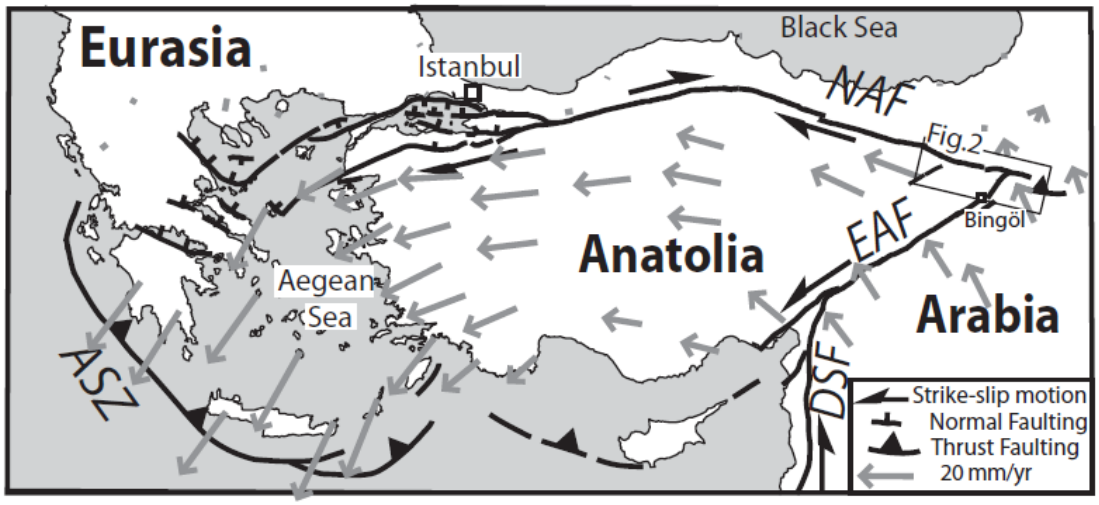

Figure 1.1 Tectonic environment of the Anatolian plate. Main features are the North Anatolian Fault (NAF), East Anatolian Fault (EAF), and the Aegean Subduction Zone (ASZ), which is often referred to as the Hellenic subduction zone. Image from Hubert-Ferrari et al. (2008).

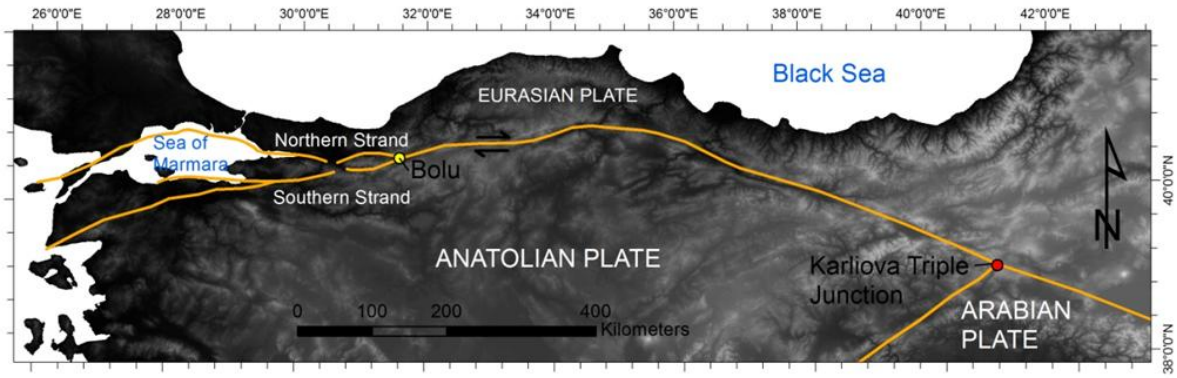

Figure 1.2 A simplified expression of the NAF and its bifurcation into the northern and southern strands west of the town of Bolu.

1.2 DETERMINING THE STRUCTURE OF THE WESTERN NAF

Fault geometry is sometimes hard to observe as a trace on the surface when little or no topographic expression is present, or if the fault has been covered by young sediments. One of the ways to understand the structure, or geometry, of faults such as the NAF is through stress modeling, because stress and strain fields are heavily influenced by the active fault geometry (Bilham and King, 1989; Lesne et al., 1998). The active fault geometry in a region can be evaluated by comparing modeled stress field orientations from various possible geometries to the known stress orientations within a region. Two methods of identifying the known stress orientations in a region are: (1) evaluation of earthquake focal mechanism data and (2) exploration of topographic data to interpret the paleostress orientation within a region.

Focal mechanisms are graphical representations of the observed pattern of first motions resulting from an earthquake (Figure 1.3). The directions of compression and tension are referred to as the P- and T-kinematic axes, which are oriented 45° to the fault plane and perpendicular to each other. An additional axis, known as the N-kinematic axis, is orthogonal to the P- and T-axes. The P- and T-kinematic axes of a single focal mechanism are not always representative of the orientation of the greatest (σ_1) and least (σ_3) compressive stress directions to the fault plane, as would be expected for the initial Coulomb failure; stress conditions and directions that produce the fault plane (described by Coulomb failure criterion) may differ from those that are caused by slip reactivation (Davis et al., 2012). However, aggregating kinematic axes from focal mechanism data over a larger region can provide a suitable statistical interpretation for the orientation of the primary stresses acting on that region (Hergert and Heidbach, 2011). With available focal mechanism data, I employ an analysis of aggregated focal mechanism kinematic axes to interpret the σ_1 orientation for modeled regions. Since the stress models of possible fault

geometries that I present are two dimensional, I model the maximum stress orientation in the horizontal plane. This is synonymous to the orientation of σ_1 if the plunge is <5°. When plunges are too great to consider the primary stress orientation as representative of the maximum horizontal stress, I develop a general focal mechanism for the entire region from the aggregated kinematic axes and use the most compressive, horizontal stress orientation as the orientation of maximum horizontal stress. This orientation is compared to the frequency orientation of the modeled stress field in order to identify the possible fault geometry which is most representative of the active fault geometry.

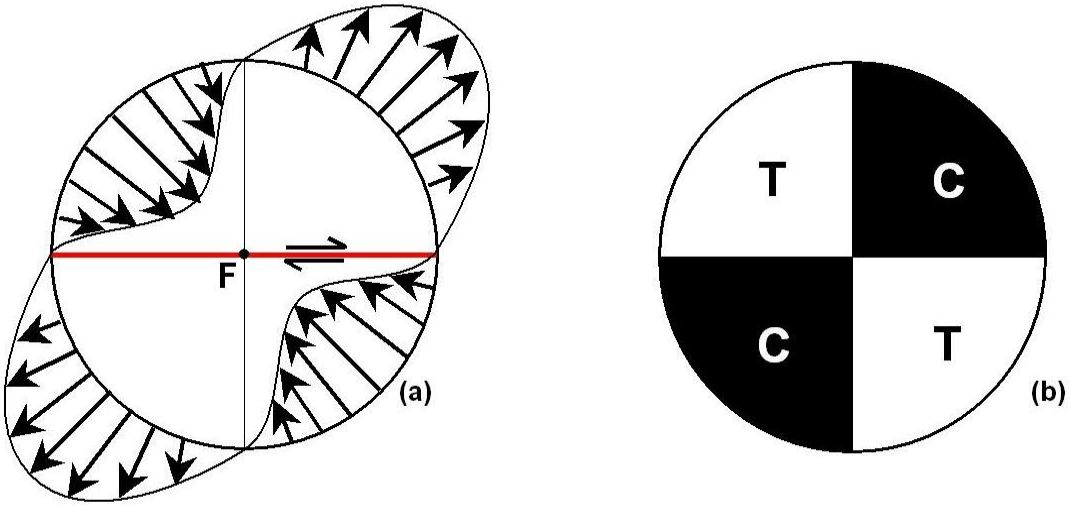

Figure 1.3 Schematic diagram of focal mechanism data. A) Direction of initial movement of particles around the focus (F) for an east-west trending dextral strike-slip fault (red). B) The zones of compression and tension. Maximum compression and tension occur 45° clockwise to the fault plane. Image from Davis et al. (2012)

Lineament analysis is another method that can be compared to the orientations of the modeled stress field to identify stress orientations in a region. Tectonic features such as faults, fracture systems, and joints may exert a strong control on topographic patterns due to these features creating pathways for weathering and erosion. These linear features can be mapped

using digital imagery of topography and other remote sensing data. The two types of digital imagery used for the lineament analysis in this dissertation are: (1) Digital Elevation Model (DEM) images from the Global Land Cover Facility (GLCF) (USGS, 2008) and (2) an Advanced Spaceborne Thermal Emission and Reflection radiometer (ASTER) product (AST14DMO). The DEM images are processed by applying hill-shades to highlight topographic changes at 45° azimuthal intervals. The hill-shades are performed at a 45° vertical sun-angle, as linear features were most evident at this angle. For the ASTER image, the bands with the highest spectral resolutions (15 meters) are necessary to use in image processing and lineament picking - specifically band 3N in the Very-Near InfraRed (VNIR) region. I applied directional filter to the ASTER image at 45° increments, creating a series of filtered images. The lineaments picked in these images specifically highlight the differences in surface feature Digital Number (DN) values, which vary between materials. These DN value differences highlight the main structures (such as fault displacement which juxtaposes two unique materials) and larger stream valleys. They could also further emphasize smaller scale linear features that may not be presented by the DEM, such as fluvial systems that do not exhibit prominent topographic valleys, but still take advantage of fractures and joints. I manually pick lineaments for both sets of images (DEM and ASTER), allowing me to preferentially pick lineaments that are not man-made structures such as roads or railways. It is, however, possible to pick lineaments that do not have a tectonic source. These lineaments are typically outnumbered and outweighed by lineaments which are parallel to mapped faults (see Chapters 2 and 5). The picked lineaments can exhibit some curvature, which can be handled by splitting the lineaments into 10 equal segments for which the azimuthal orientation of each segment is calculated and averaged to express the best possible orientation of each lineament. The results of the lineament analysis are plotted as frequency rose diagrams both

unweighted and weighted by the length of the lineaments to identify prominent features. A simple workflow for the lineament analysis is outlined in Figure 1.4.

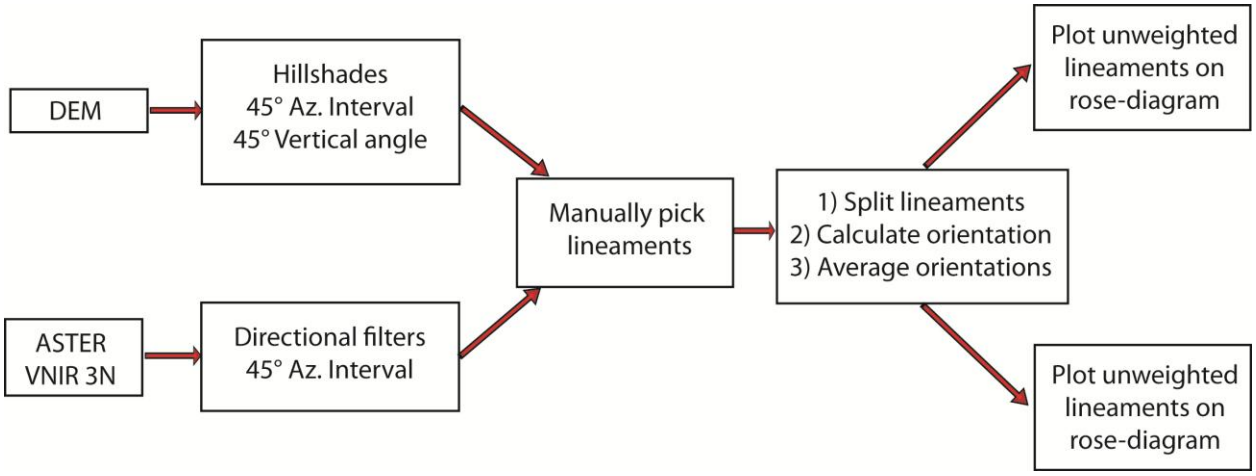

Figure 1.4 Lineament analysis workflow.

Riedel shearing is characteristic of, but not limited to, strike-slip faulting (Davis et al., 2012; Riedel, 1929), and can be used to interpret the results of the lineament analysis to infer the paleostress orientation. In fault shear zones, the imposed shear, or Main Fault (MF) orientation is accompanied by conjugate Riedel shears, R and R' (Figure 1.5). R is synthetic to the shearing motion, while R' is antithetic, meaning that dextral shear zones have dextral R-shears, but sinistral R'-shears. The two conjugate shear sets are 60° apart and bisected by σ_1, which is 45° clockwise from the MF, or imposed shear. An additional shear (P) is oriented 10° from the MF. Prominent orientations identified by the lineament analysis are compared to mapped MF orientations and found to share a common orientation. Secondary features also align with Riedel shear orientations, as well as with the orientation of σ_1 suggesting the presence of extensional fractures. Thus, prominent lineament orientations in the NAF zone of deformation are consistent with Riedel shear geometries. From the most prominent lineament orientation, or MF orientation, we infer a σ_1 orientation for the region 45° clockwise, as would be expected in fault zones with

Riedel shearing. I compare this inferred paleostress orientation to modeled stress field orientations to identify the fault geometry most representative of the active faults.

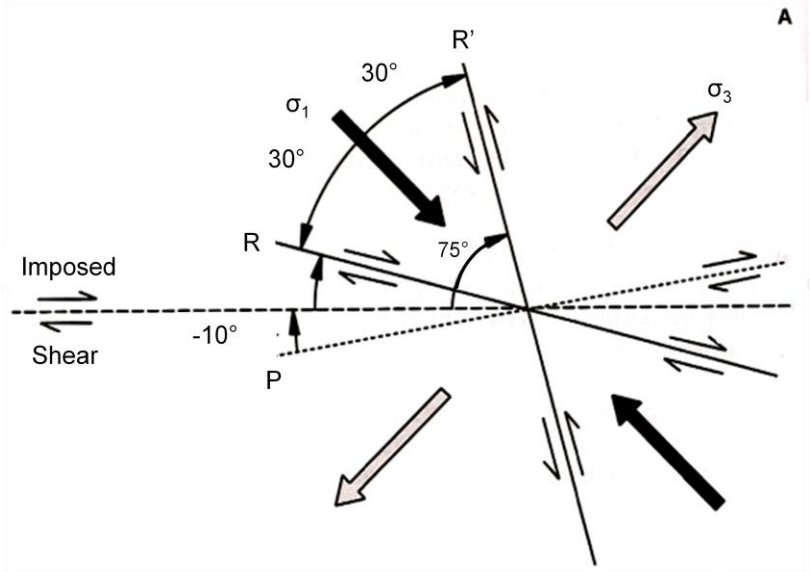

Figure 1.5 Riedel shearing for a dextral shear zone. The imposed shear is also the Main Fault (MF) orientation. Image adapted from Davis et al. (2012).

Where available, I employ an analysis of focal mechanisms and lineament analysis of topography or satellite imagery to determine geologic stress orientations. In Chapter 2, the active through-going geometry east of the Marmara Sea and west of Bolu is identified by comparing modeled stress field orientations to both focal mechanism data and a lineament analysis. In Chapter 5, the active through-going geometry in the Marmara Sea and Biga Peninsula regions are modeled. Focal mechanism data is available for both regions, but topographic data was only available for the Biga Peninsula region. From our results, I am able to propose a through-going active fault geometry for the western NAF structure as a working hypothesis for use in geophysical models by combining the determined active fault geometries for the regions studied in Chapters 2 and 5, and described further below.

1.2.1 East of the Marmara Sea (Chapter 2)

In the region impacted by the 1999 Izmit earthquake sequence, the through-going NAF splits into a northern and southern strand just west of the town of Bolu, and continue westward to bound the Marmara Sea (Figure 1.6 A) (Barka et al., 2002; Hergert and Heidbach, 2010; Şengör et al., 2005). For this region, two potential geometries of the active through-going strands of the NAF are proposed based on an evaluation of seismicity, topographic data, and a literature review discussed in further detail in Chapter 2. The first geometry suggests that the two strands almost converge (west of Bolu) towards the Mudurnu Valley, and then diverge as distinct fault traces (Figure 1.6 B) (Akyüz et al., 2002; Barka et al., 2002). The second geometry is similar, except that the southern and northern faults described above are linked by a fault through the Mudurnu Valley (Figure 1.6 A). To evaluate which geometry best represents the through-going active fault geometry, I process simplified two-dimensional viscoelastic models for each of the fault geometries with a finite element method to evaluate primary horizontal stress orientations for the region. The faults separate blocks/zones that require rock strength properties of density (ρ), compression wave velocities (V_p), and shear wave velocities (V_s), which are evaluated from geologic maps of the surface. Necessary input for the faults are static fault conditions - static friction coefficient (μ_s) and cohesion (C).

Narrowing the static fault conditions in the model proved to be very difficult, as numerical and laboratory experiments on the NAF and the SAF, with which the NAF shares many common attributes, resulted in a large range of proposed static friction coefficients (Table 1.1) (Carpenter et al., 2011; Carpenter et al., 2012; Chang et al., 2011; Chéry et al., 2004; Hergert and Heidbach, 2011; Jiménez-Munt et al., 2006; Johnson et al., 2006; Kasapoglu and Toksöz, 1983; Lockner et al., 2011; Provost et al., 2003; Stein et al., 1997; Tembe et al., 2006).

Furthermore, cohesion was assumed to be 0 kPa, or is never discussed as a parameter (Carpenter et al., 2011; Carpenter et al., 2012; Chang et al., 2011; Chéry et al., 2004; Hergert and Heidbach, 2011; Jiménez-Munt et al., 2006; Johnson et al., 2006; Kasapoglu and Toksöz, 1983; Lockner et al., 2011; Provost et al., 2003; Stein et al., 1997; Tembe et al., 2006). In Chapter 3 of this dissertation I discuss this non-consensus on the static fault parameters for the NAF and other tectonic strike-slip faults. However, for initial models, I chose μ_s=0.4, because it most closely matches rock strength experiments conducted by Byerlee (1978) while also considering a moderate pore pressure as a Skempton's coefficient value of 0.5. Additionally, I chose to assign C=0 kPa to the faults as the majority of researchers disregard the effects of cohesion from both numerical and laboratory experiments. I apply these values to all the faults within the region in both models.

Table 1.1 Proposed static friction and cohesion for the NAF and SAF based on rock experiments and numerical work.

Laboratory Rock Experiments				
Static Friction	**Cohesion (MPa)**	**Source**	**Fault**	**Note**
0.21	0	(Carpenter et al., 2011)	SAF	
0.09-0.25	0	(Carpenter et al., 2012)	SAF	Closer to SAF fault plane.
0.15	0	(Lockner et al., 2011)	SAF	
0.4-0.55	N/A	(Tembe et al., 2006)	SAF	
0.6	N/A	(Johnson et al., 2006)	SAF	Matches estimates derived from early lab work by Byerlee.
0.4*	N/A	(Stein et al., 1997)	NAF	
Numerical Models				
Static Friction	**Cohesion (MPa)**	**Source**	**Fault**	**Note**
<0.1	0	(Chéry et al., 2004)	SAF	Matches far-field and pilot hole stress data.
0.38	N/A	(Chang et al., 2011)	SAF	Co-seismic stress change/slip.
0.05-0.1	0	(Provost et al., 2003)	NAF	Required to replicate GPS velocity field.
<0.4	0	(Kasapoglu and Toksöz, 1983)	NAF	NAF locks at μ=0.4.
0.05	0	(Jiménez-Munt et al., 2006)	NAF	Required to match Anatolian block rotation to GPS measurements.
0.05*	0	(Hergert and Heidbach, 2011)	NAF	Based on assumption that tectonic SS faults are weak.

To develop the stress field, I push/pull boundaries of each zone at average rates of motion determined for each block based on an analysis of GPS velocities in the region (Ozener et al., 2009). The stress orientations from the two models are compared against the maximum horizontal stress orientation inferred from a lineament analysis and a record of focal mechanisms. The fault geometry that best replicates the geologic stress from focal mechanism data and inferred from a lineament analysis is the geometry which includes a linking fault between the northern and southern strands through the Mudurnu Valley. This research and its results have been published (Karimi et al., 2014) and are presented in further detail in Chapter 2 of this dissertation.

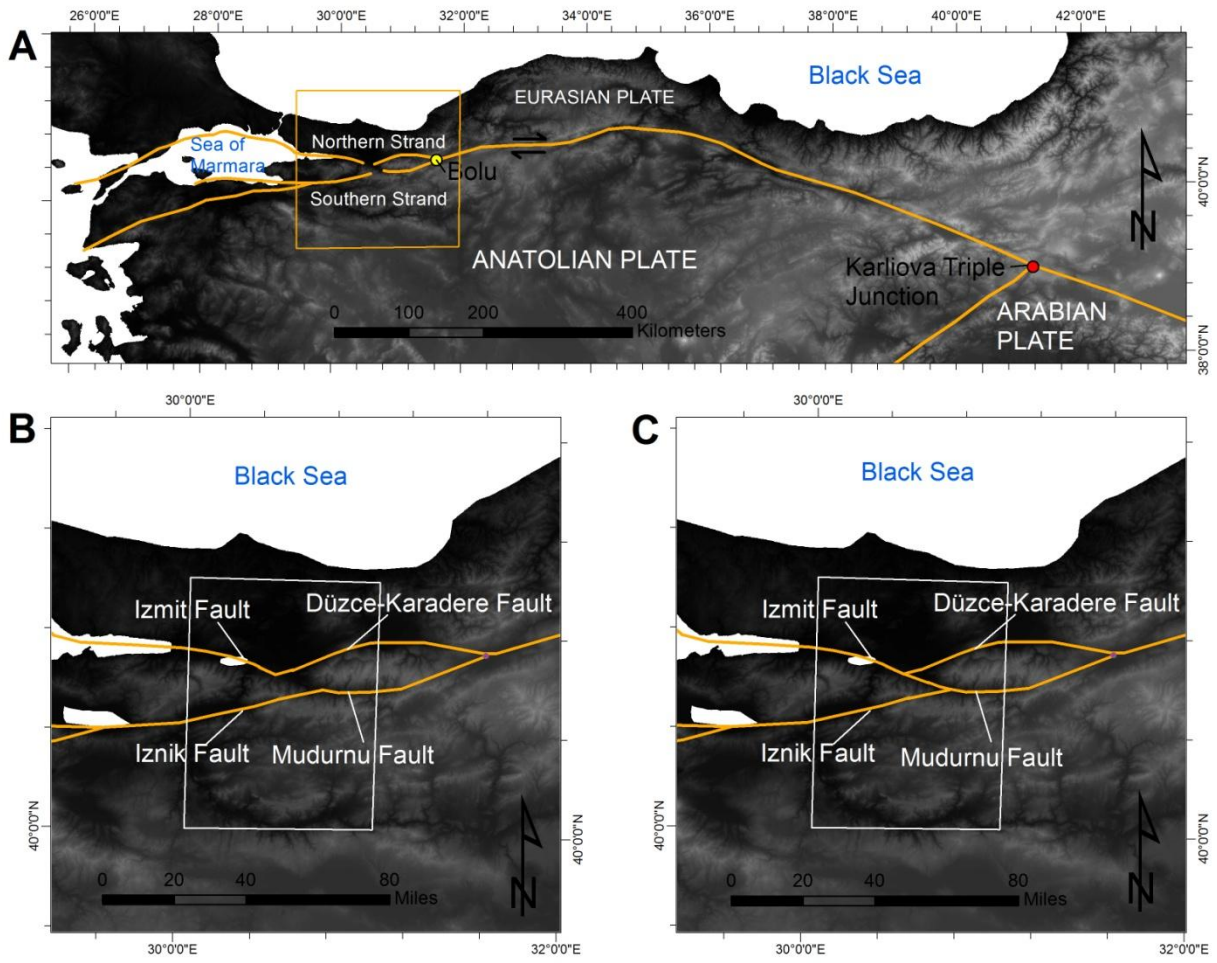

Figure 1.6 Tectonic setting and possible fault geometries of the NAF east of the Marmara Sea. A) Tectonic setting of the NAF. The NAF splits near the town of Bolu and continues on as two strands around the Sea of Marmara; B) Possible fault geometry where the northern and southern strand converge, then diverge; C) Second possible fault geometry where the two strands are linked.

1.2.2 Marmara and Biga Peninsula regions (Chapter 5)

West of the Mudurnu Valley, there are two additional areas where the active fault geometry of the NAF is debated: in the Marmara Sea, and in the Biga Peninsula. These two regions, particularly along the coasts of the Marmara Sea, are highly populated and host key port cities that facilitate trade between Asia, the Mediterranean. As such, they are also highly susceptible to

crippled infrastructures following high magnitude earthquakes, such as the August 1999 Izmit quake. Seismic hazard predictions and modeling, as mentioned earlier, are heavily dependent on the developing stress field, which is in turn affected by the active fault geometry. In Chapter 5, I develop stress models to determine the active fault geometry in the Marmara and Biga Peninsula regions and propose a through-going geometry for the western NAF. However, the stress models used in this chapter differ from my work in Chapter 2 in their fault strength properties. Having constrained static (Chapter 3) and dynamic fault parameters (Chapter 4), I utilize frictional fault parameters that are found to be more representative for the NAF interface to achieve my goal of proposing a more accurate fault geometry for the western NAF.

The faults modeled in Chapter 2, continue to diverge to the west, where the northern strand bifurcates in the Gulf of Izmit (north of the Armutlu Peninsula) (Figure 1.7). The faults in this region separate small crustal blocks due to fragmentation with the developing Marmara Sea basin (Aksu et al., 2000). Previous tectonic models attempting to describe the formation of the Marmara Sea adhere to classical models of pull-apart basin formation along releasing bends or stepovers within a dextral strike-slip fault system (Figure 1.8 A and B) (Aksu et al., 2000; Ergün and Özel, 1995; Okay et al., 1999; Wong et al., 1995). However, Aksu et al. (2000) suggest that fault patterns identified on a high-resolution bathymetric map and from seismic profiles point to an alternative deformation style and architecture for transtensional basins. The internal architecture of the flower structure above a deeply buried master fault depicts fault elements oriented opposite to the geometry expected for a dextral, releasing strike-slip system (Figure 1.8 B) (Aksu et al., 2000). Additionally, a flower structure oblique to the orientation of the master fault, as is the case in the classic pull-apart basin (Figure 1.8 A) (Dooley and McClay, 1997), is not identified in seismic profiles of the Marmara basin (Aksu et al., 2000). For the Marmara Sea

basin, Aksu et al. (2000) suggest an unconventional negative flower structure in-line with the buried NAF (master fault).

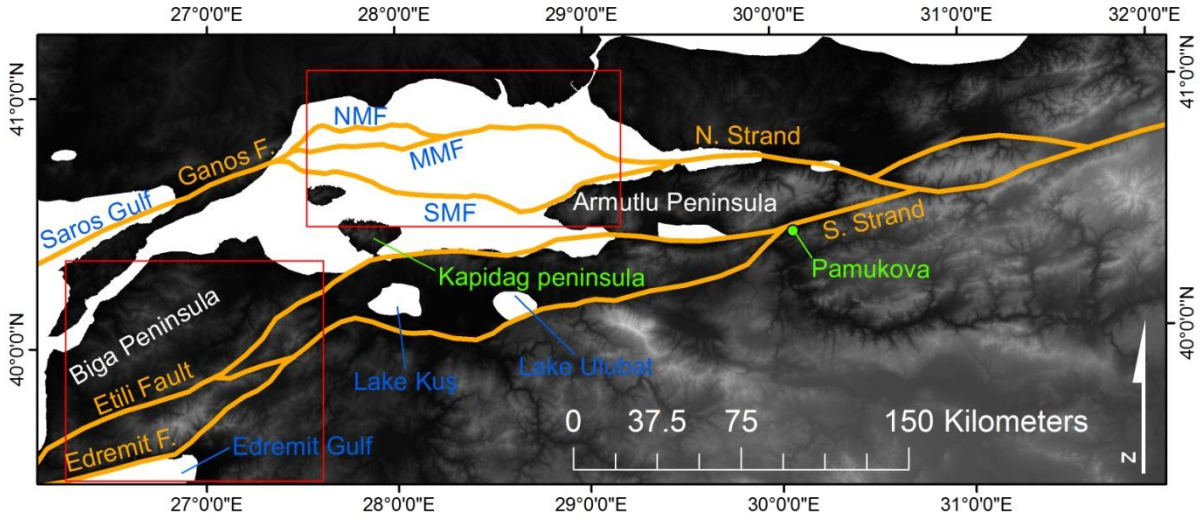

Figure 1.7 Possible complexity of the northern and southern strands of the western NAF. NMF is North Marmara fault, MMF is Main Marmara fault, and SMF is Southern Marmara fault. The regions bound in red are the Marmara region (in the north) and the Biga Peninsula region (in the south).

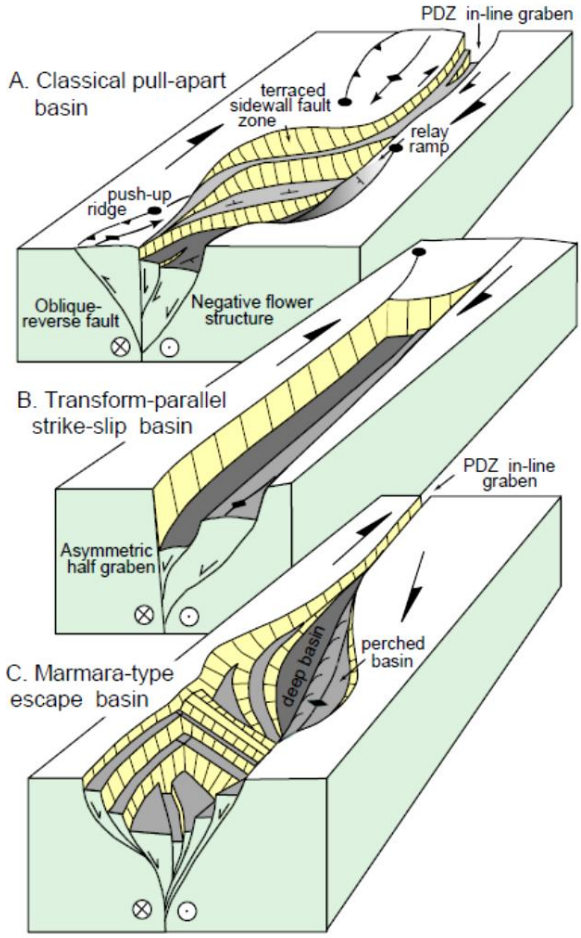

Figure 1.8 Contrasting geometries of strike-slip basins in a dextral fault system. A) Classic pull-apart basin with a negative flower structure oblique to the strike of the master fault. B) Strike-parallel basin with asymmetrical half-graben structures. C) Proposed Marmara-type escape basin with a flower structure in-line to a deep buried master fault (NAF). Image from (Aksu et al., 2000).

Through-going faults associated with the developing Marmara Sea basin are prominent features near the boundaries defining the basins principle zone of deformation (Aksu et al., 2000), and three geometries of active faults in the Marmara Sea are proposed (Figure 1.7). The southernmost trace parallels the northern Armutlu Peninsula then extends west-northwest across the Marmara Sea as the Southern Marmara Fault (SMF) (Aksu et al., 2000; Armijo et al., 2002; Barka and Kadinsky-Cade, 1988; Hergert and Heidbach, 2010, 2011; Hergert et al., 2011;

Şengör et al., 2014; Straub et al., 1997). The northernmost trace continues to parallel the northern shore of the Marmara Sea as the Main Marmara Fault (MMF) (Flerit et al., 2003; Hergert and Heidbach, 2010, 2011; Hergert et al., 2011; Le Pichon et al., 2001; Şengör et al., 2014). Another possible active fault geometry for the northern trace could be the MMF until its intersection with the Northern Marmara Fault (NMF), where it continues only as the NMF (Aksu et al., 2000). Lastly, the MMF and NMF traces are both part of the active fault geometry (Armijo et al., 2002). These various faults would intersect just off the coast of the western Marmara Sea and continue across to the Saros Gulf as the Ganos Fault (Aksu et al., 2000; Armijo et al., 1999; Armijo et al., 2002; Flerit et al., 2003; Hergert and Heidbach, 2010, 2011; Hergert et al., 2011; Le Pichon et al., 2014; Le Pichon et al., 2001; Şengör et al., 2005; Türkecan and Yurtsever, 2002). In Chapter 5 of this dissertation, I discuss further details and evidence for these three possible active fault geometries of the Marmara region.

The southern strand bifurcates at the town of Pamukova where both of its traces parallel the southern shores of the Marmara Sea until to the Kapidag Peninsula. At this location, the traces trend southwest into the Biga Peninsula (Figure 1.7), where several through-going active fault geometries are proposed. In one possible geometry, the southern trace could terminate at the intersection with the active fault geometry following the trace of the linking fault to continue slip along the northern trace (Konak, 2002). In a second possible active fault geometry, the linking structure is absent, and the southern trace continues until it reaches the Edremit Gulf and follows the southern coastline of the Biga Peninsula (Barka and Kadinsky-Cade, 1988; Boztepe-Güney et al., 2001; Konak, 2002; Şengör and Canıtez, 1982; Straub et al., 1997; Türkecan and Yurtsever, 2002; Yılmaz and Karacık, 2001). The third potential geometry has all faults as part of the active fault geometry in the Biga Peninsula region (Konak, 2002; Şengör et al., 2005; Türkecan and

Yurtsever, 2002). In Chapter 5, I provide further details and evidence behind these three possible fault geometries for the Biga Peninsula region.

To evaluate which geometry best represents the through-going active fault geometry, I develop simplified viscoelastic two-dimensional models for each of the fault geometries in both regions and process them with a finite element method to evaluate primary stress orientations for the region. As in the description of the model setup for Chapter 2, I apply velocity boundary conditions based on averages of GPS velocities for each fault separated block, which are assigned rock physics properties (ρ, V_p, and V_s) based on surficial rock maps (Biga Peninsula) and tomographic data (Marmara Sea). Additionally, based my prior work to constrain frictional parameters for the fault (Chapters 2 and 3), I applied static fault interface conditions of μ_s=0.2 and C=500 kPa. The stress orientations resulting from the models of the Marmara region are compared against the maximum horizontal stress orientation from a record of focal mechanisms, as there is no available topographic data on which to perform a lineament analysis. The results of the Biga Peninsula region stress models are compared against the maximum horizontal stress orientation, as inferred from a lineament analysis and a record of focal mechanisms. The proposed geometry of the western NAF is shown in Figure 1.9. In Chapter 5, I discuss the details and interpretations of the results for this research.

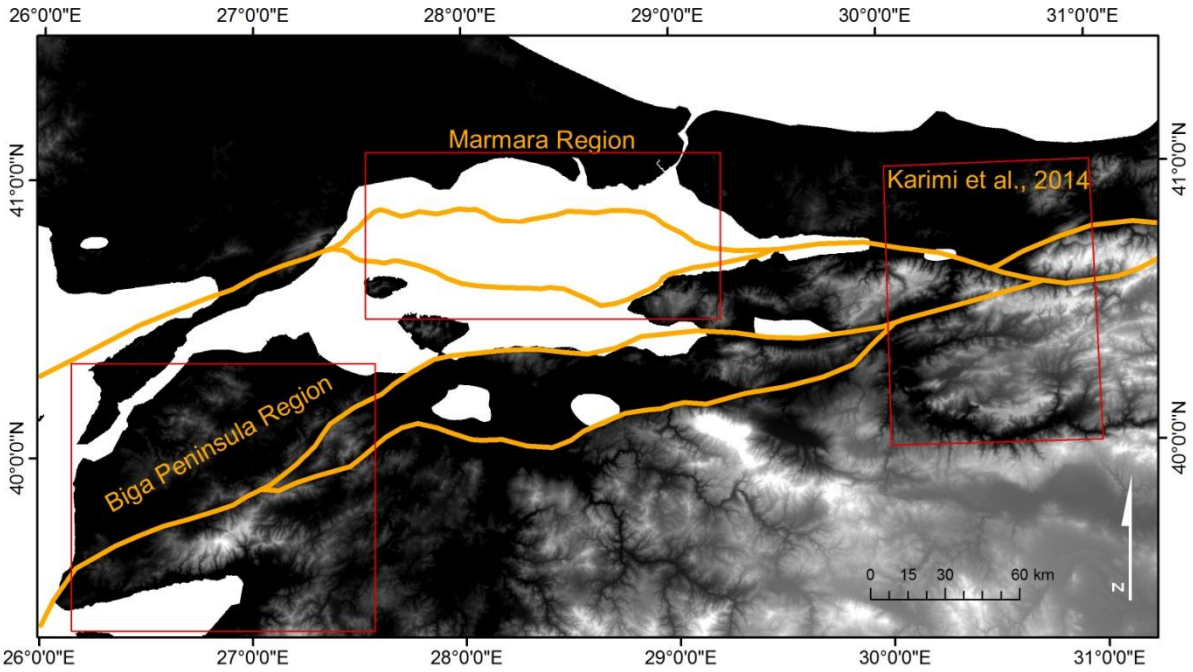

Figure 1.9 Proposed through-going active fault geometry of the western NAF..

1.3 FAULT PARAMETERS AND STRENGTH OF THE NAF

The magnitude and timing of stress accumulation during interseismic periods, is influenced by fault strength parameters, which also affect the timing of rupture, recurrence, and magnitude of earthquakes. Static fault parameters, static coefficient of friction (μ_s) and Cohesion (C), define the frictional strength of a fault that must be overcome by a particular stress magnitude, or fault traction, to cause rupture and subsequent slip at a steady rate. Generally, a weaker stress magnitude is required to maintain fault motion following rupture than is needed to initiate fault rupture (Rabinowicz, 1951). In the stick-slip friction model, slip begins when the static friction (μ_s) of the fault interface is overcome. Once slip motion commences, a fault loses strength, and this reduction of strength from static to a reduced kinetic (dynamic) (μ_k) friction is the most

simple constitutive relation used to describe a frictional interface in the classical "static-kinetic" friction law (Figure 1.10) (Rabinowicz, 1951; Rice and Tse, 1986). The fault strength transition from static to kinetic values does not occur instantaneously, but rather tends to occur over a window of time (Figure 1.10) (Rabinowicz, 1951). This rate of strength reduction can be characterized by a slip-weakening distance (D_c) (Hirose and Shimamoto, 2005). The decrease in friction on a fault interface is referred to as dynamic fault weakening and should not be confused with strain softening which refers to a material bodies (not fracture interfaces) susceptibility to deformation at lower stresses. The values of static and dynamic fault parameters are highly dependent on both the fault bounding materials and the fault gouge material, which may act as a lubricant to decrease the frictional coefficients (Barton, 1974; Wyllie, 1999).

In Chapters 3 and 4 of this dissertation I focus on constraining the estimates for static fault parameters and dynamic fault parameters for the NAF, and evaluate the strength of the NAF, by developing stress models of the faults east of the Marmara Sea and west of Bolu. Modeled rupture times (slip >1 m along 50% of fault lengths) are compared to recurrence intervals of M_w>6.0 earthquakes for the Mudurnu Valley and Düzce-Karadere faults, which are 100-150 years (Palyvos et al., 2007) and 300 years (Pantosti et al., 2008), respectively. The recurrence intervals are used as a proxy for the time it takes stress to build up from a relaxed state to fault rupture. Following the August 1999 Izmit earthquake sequence, a total maximum slip of 5 m was measured for the Izmit fault (Barka, 1999). When the rupture conditions are met, the total maximum slip on the Izmit fault is compared to this known 5 m of slip to constrain the data further. My work on constraining static fault parameters for the NAF is described in Chapter 3. My work on constraining dynamic fault parameters for the NAF is described in Chapter 4.

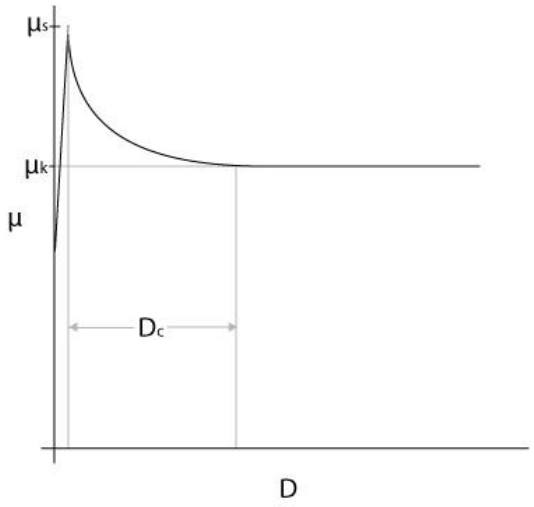

Figure 1.10 Simplified representation of a friction (μ) vs. displacement (D) curve from laboratory experiments.

1.3.1 Static fault parameters (Chapter 3)

Static fault conditions define the strength of a fault interface that must be overcome by the developing stress, as fault traction, to rupture the fault and cause it to slip. In Chapter 2, I discuss the problem regarding the diversity in range of static fault conditions that have been suggested for the NAF and similar tectonic strike-slip faults (e.g., SAF) based on numerical and laboratory experiments (Table 1.1). This range of weak to strong static friction coefficients raises the question regarding a suitable value of μ_s for the NAF. Additionally, no cohesive strength further assumes a rough, clean discontinuity surface with rock to rock contact and no infilling due to weathering or grinding of rocks (Wyllie, 1999). However, cohesion is developed on fault planes in many conditions, and even a small cohesion can have a significant effect on the strength of a fault, ultimately affecting the progression of slip and rupture times of faults (Wyllie, 1999).

To constrain ranges of static fault parameters for the NAF east of the Marmara Sea, I develop finite element stress models and simulate varying static friction coefficients and cohesions using rock physics parameters and velocity boundary conditions (see Chapter 2). In each simulation, I compare the rupture time of the Düzce-Karedere and Mudurnu faults, or when 50% of the fault length has ruptured >1 m, to their recurrence intervals (a proxy for the time it takes to build up stress from a relaxed state to fault rupture). When the final fault ruptures, I record the total slip on the Izmit fault and compare it to the maximum slip (5 m) of the Izmit fault following its 1999 earthquake sequence. Two important conclusions can be drawn from this research. The first is that at cohesion values below 200 kPa, the Düzce-Karadere fault ruptures before the Mudurnu Valley fault, which does not match the expected rupture pattern based on recurrence intervals. At higher cohesion values, the faults rupture in a sequence that matches this pattern. Thus, cohesion is necessary in the model to rupture the Düzce-Karadere and Mudurnu faults over their documented recurrence intervals. Secondly, a range of static friction coefficients for each cohesion interval, with static friction decreasing with increased cohesion, was also constrained by the simulations. To have the maximum slip on the Izmit fault match the recorded 5 m from the 1999 Izmit earthquake, the range of permissible cohesion decreased to C=300-500 kPa. By comparing both static friction coefficient and cohesion with the published estimates of cohesion from shear strength experiments (Barton, 1974) and from the most frequently documented values of static friction in literature on rock or numerical experiments on tectonic strike-slip faults, I recommend a static friction of $\mu \leq 0.2$ with a cohesion of C=500 kPa for geophysical models of the NAF. I discuss this research and its results in further detail in Chapter 3 of this dissertation.

1.3.2 Dynamic fault parameters (Chapter 4)

Data on fault surface heat flow (heat due to friction) and stress orientations around crustal-scale fault zones, such as the San Andreas Fault (SAF) in California (Lachenbruch and Sass, 1980; Zoback et al., 1987), and slip on low-angle normal faults (Collettini and Sibson, 2001; Sibson, 1994) indicate that they are much weaker than expected from laboratory models of friction (Holdsworth, 2004). This weakness may be due to: (1) the presence of statically weak minerals (Lachenbruch and Sass, 1980; Lockner et al., 2011; Moore and Rymer, 2007) or (2) fault weakening at high slip velocity (Boutareaud et al., 2008; Di Toro et al., 2006; Lachenbruch and Sass, 1980). The SAF is thought to be an example of such a weak fault, as it does not exhibit a frictional heat flow anomaly, and the direction of maximum principal stress (σ_1) is near-perpendicular to the fault trace (Faulkner et al., 2006; Holdsworth, 2004). The NAF shares many similarities with the SAF; length, age, slip rates, and geometry (Allen, 1982), but it does not exhibit near-perpendicular angles between its fault trace and the direction of σ_1, and there are no data regarding the stress magnitude or heat flow of the NAF, particularly west of the town of Bolu in the Marmara region (Dresen et al., 2007). This raises a question regarding the strength of the NAF, and what conditions best replicate the geologic record in stress models of the NAF.

To evaluate the effect of dynamic fault properties on the NAF, I develop stress models utilizing rock physics parameters and velocity boundary conditions for fault-separated blocks (see Chapter 2). Additionally, I prescribe varying kinetic friction coefficients and a slip-weakening distance for initial static fault conditions that match and exceed the geologic constraints (see Chapter 3). I evaluate estimates of dynamic fault parameters that produce modeled rupture times (Düzce-Karadere and Mudurnu faults) and total slip (Izmit fault) that best match the recurrence intervals (a proxy for the time it takes to build up stress from a relaxed state

to fault rupture) and the maximum slip of 5 m for the Izmit fault. I find that for static fault conditions constrained in Chapter 3, dynamic friction within 0.2 of static friction makes the fault too weak with lower slip-weakening distances. This changes at higher D_c, where the faults weaken too slowly to show significant change in rupture time with varying μ_k. At static friction and cohesion values that ruptured the faults too slowly to match the constraints, a range of kinetic friction weakened the faults to satisfy the rupture times. This range decreases with increasing D_c. From these observed trends, I am able to suggest dynamic fault parameter values for static frictions, μ=0.6-0.8, consistent with the results of rock strength experiments by Byerlee (1978). At lower cohesions, C=300 kPa, the value for kinetic friction should satisfy μ_s-$\mu_k \leq 0.2$ for slip-weakening distances less than or equal to 1 m, but the range of acceptable values should grow when the value of D_c is considered to be between 1 and 5 m. At 400 kPa, I infer that kinetic friction coefficients of $\leq$0.4 with D_c between 1 and 5 m satisfy the geologic constraints. For lower static frictions, a wider range of slip-weakening distances and kinetic frictions are permissible, but would require some component of weak fault interface materials to lower the static friction below the classic Byerlee (1978) experiments. I suggest using the static fault parameters discussed in Chapter 3 for future geophysical models of the NAF, given the computationally expensive nature of running dynamic models. I discuss this research and its results in further detail in Chapter 4 of this dissertation.

1.4 IMPLICATIONS AND FUTURE DIRECTIONS

The research described in this dissertation contributes to future geophysical and seismic hazard models for the NAF by providing a more accurate through-going active fault geometry and fault

strength parameters. The active fault geometry influences the stress and strain field, and fault strength impacts the recurrence interval and magnitude of earthquakes. The geometry of the western NAF, proposed in Chapter 5, is a working hypothesis. Further stress modeling of the entire western NAF will help evaluate if the proposed through-going active fault geometry is valid, as well as further constrain fault strength parameters and test whether the best fit fault parameters for the Bolu region are correct for the rest of the NAF system. Although the earthquake record will not permit matching fault recurrence intervals and slip magnitudes through most of the system, fault modeling can predict velocity directions and magnitudes of trapped lozenges in the NAF system that can be evaluated against measured GPS data. The results of the work on the fault strength parameters in this dissertation suggest that the NAF could be statically weak due to clay infilling present at the fault interface, but could also be statically strong and weakened dynamically. While no consensus could be made on the mechanism behind a potentially weak NAF, the work in this dissertation makes a strong case for pilot drill hole projects, similar to the San Andreas Fault Observatory at Depth (SAFOD), to bring samples from the fault interface into a laboratory environment for further testing.

2.0 DETERMINING THE GEOMETRY OF THE NORTH ANATOLIAN FAULT EAST OF THE MARMARA SEA THROUGH INTEGRATED STRESS MODELING AND REMOTE SENSING TECHNIQUES

The 1200 km long North Anatolian Fault (NAF) is part of an east-west striking dextral shear zone (NAF system), along the boundary between the Anatolian and Eurasian plates, that widens to the west. This widening zone of deformation complicates potential earthquake rupture paths and highlights the importance of understanding the geometry of active fault systems. In the central portion of the NAF system - just west of the town of Bolu - the NAF splits into two major faults: the northern and southern strands. These two faults diverge, almost converge, then diverge again to border the Marmara sea. Earthquake data from the region where the two faults converge indicate that they may be linked by an active fault. We model the active fault geometries with and without the linking fault to explore its impact on the output regional stress field (from a finite element model). These results are compared to focal mechanism records and lineament analyses to determine which geometry best simulate the stress field in a regional model. Our results show that a linking fault between the northern and southern strands of the NAF system is necessary to best match the primary stress orientations of the model with the maximum paleostress orientations inferred from deformation patterns, and observed in earthquake focal mechanisms. Furthermore, the linking fault should be a significant component in future models of the NAF system within the region.

2.1 INTRODUCTION

Due to the effect of fault geometry on modeled stress and strain fields, accurately representing the active fault geometry is a critical component of the modeling process (Bilham and King, 1989; Lesne et al., 1998). Longer, linked faults host the majority of earthquakes - particularly high magnitude earthquakes - in a fault system (Barka and Kadinsky-Cade, 1988; Slemmons and Depolo, 1986), and are the most influential in the development of the regional stress and strain field (Bilham and King, 1989; Lesne et al., 1998; Schwartz and Coppersmith, 1986). In strike-slip systems, short extensional faults linking echelon fault segments allow for long-term transfer of fault slip, thus affecting the stress field distribution, and may also act as kinetic barriers impeding or arresting rupture propagation (King, 1986; King and Nábělek, 1985; Sibson, 1986). Fault geometry is sometimes hard to observe as a trace on the surface when there is little to no topographic expression, or if the fault has been covered by young sediments. In this study we examine the relationship between fault geometry, and numerically determined stress and strain fields along a strike-slip fault in Turkey by utilizing a methodology adapted from McElfresh et al. (2002).

The North Anatolian Fault (NAF) system has seen several devastating and high magnitude earthquakes, particularly in the Marmara Sea region (Bohnhoff et al., 2013; Parsons, 2004). The 1999 earthquake of August 17th was of particular note for being the largest recorded earthquake in Turkey by modern digital networks (Özalaybey et al., 2002) with a devastating death toll of over 17,000 people (Scawthorn and Johnson, 2000). In the region impacted by the 1999 earthquake, the through-going NAF splits into two strands just west of the town of Bolu (Barka et al., 2002; Hergert and Heidbach, 2010; Şengör et al., 2005): the Düzce and Karadere faults (NE portion of the northern strand), which we refer to as a single fault called the Düzce-

Karadere and the Mudurnu fault (SE portion of the southern strand) (Figure 2.1). Two potential geometries of the active through-going strands of the NAF are proposed. One active fault geometry suggests that two strands almost converge (west of Bolu) and then diverge as distinct fault traces (Figure 2.1 C) (Akyüz et al., 2002; Barka et al., 2002). The fault strands continue on to border the Marmara Sea in the north and south respectively (Figure 2.1 B): the northern strand as the Izmit fault, and the southern strand as the Iznik fault (Armijo et al., 2002; Şengör et al., 2005). The second geometry is similar, except that the southern and northern faults described above are linked by a fault through the Mudurnu Valley (Figure 2.1 C). A study of fracture zones attributed to major earthquakes of the 20th century by Koulakov et al. (2010) shows this link, as does previous work to understand stress transfer on the NAF by Stein et al. (1997). Studies of dextral displacement of Eocene volcanic rocks in the region between the northern and southern also imply an extensional linking fault (Armijo et al., 1999; Hisarli et al., 2011; Yılmaz et al., 1997). Seismic data from the Mudurnu Valley show a normal sense of motion, indicating that the link may be an extensional fault between two major echelon fault segments (Mudurnu and Izmit faults) (Heidbach et al., 2008; International Seismological Centre, 2011; Neugebauer et al., 1997). A 100 year record of earthquakes (KOERI-UDIM, 2012) clusters around the northern strand, but also illustrates that the Mudurnu Valley is seismically active, suggesting a connecting fault and supporting the second geometry (Figure 2.2 A). Additionally, it is proposed that the rupture of the 1967 M7.1 Mudurnu earthquake, the most recent of a series of historical earthquakes at its location (Palyvos et al., 2007), reached Lake Sapanca (along the Izmit fault) as distributed deformation (Ambraseys and Zatopek, 1969; Muller et al., 2003). Elevation data from a 10 meter Digital Elevation Model (DEM) - courtesy of the (GLCF) (USGS, 2008) – highlight pronounced topographic features that are a result of the southern and northern fault strands. The

southern strand is located along narrow river valleys, whereas the northern strand controls the sharp transition from high to low topography (Figure 2.2 B). This fault-controlled topography has led to the inference of no connecting fault between the two segments. A potential linking fault from the Mudurnu fault to the Izmit fault can be traced through a narrow river valley, but loses any topographic expression as it nears the northern strand. Previous studies evaluating earthquake ruptures on this segment of the NAF system identify the Mudurnu fault in the southern Mudurnu Valley, but terminate the fault trace before it links to the northern strand (Akyüz et al., 2002; Barka et al., 2002). This raises a question regarding the significance of a fault linking the two strands as part of the through-going NAF geometry within the region, and which geometry will best duplicate the regional stress and strain in geophysical models.

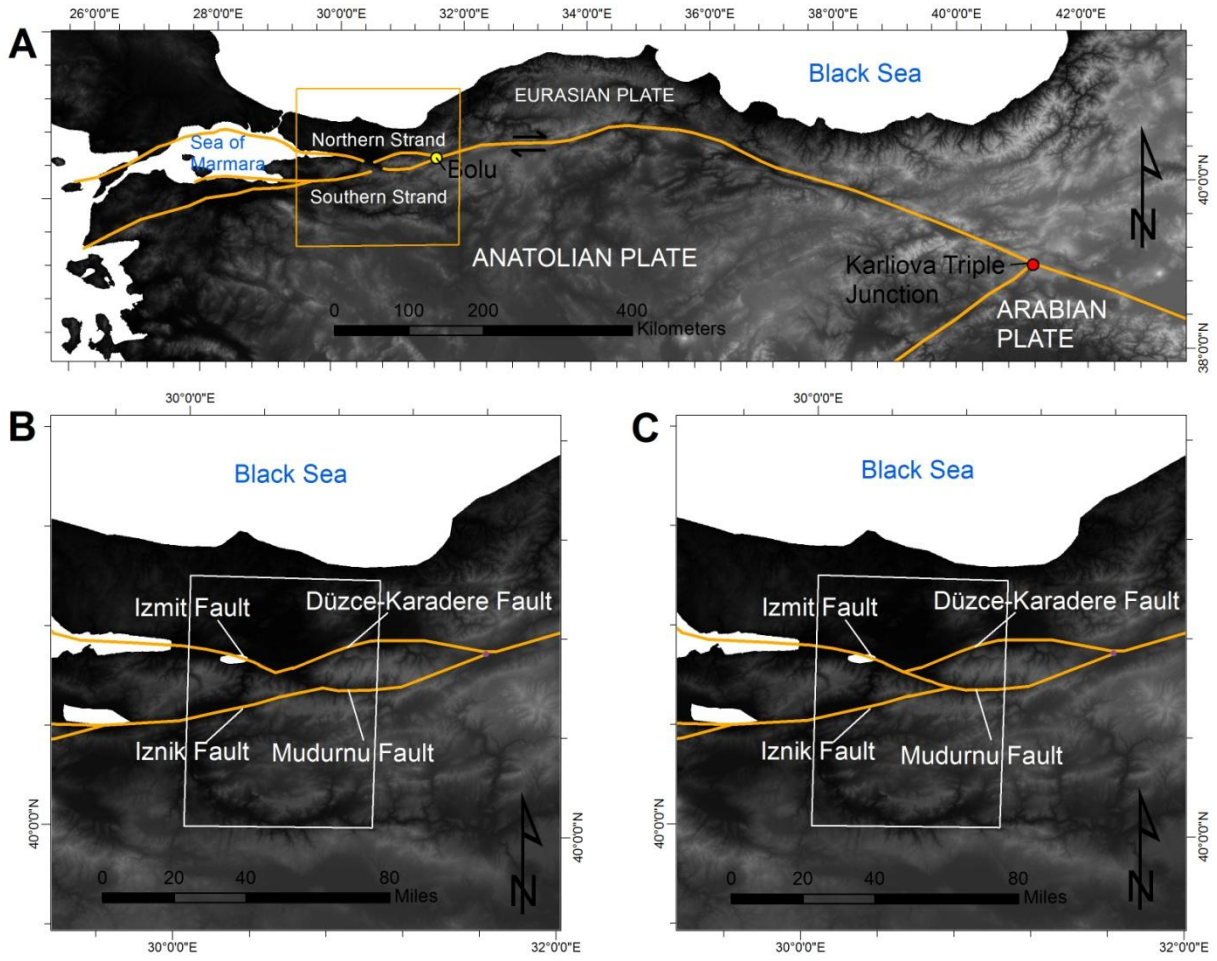

Figure 2.1 Tectonic setting and possible fault geometries of the NAF east of the Marmara Sea. A) Tectonic setting of the NAF. The NAF splits near the town of Bolu and continues on as two strands around the Sea of Marmara; B) Possible fault geometry where the northern and southern strand converge, then diverge (model 1); C) Second possible fault geometry where the two strands are linked (model2).

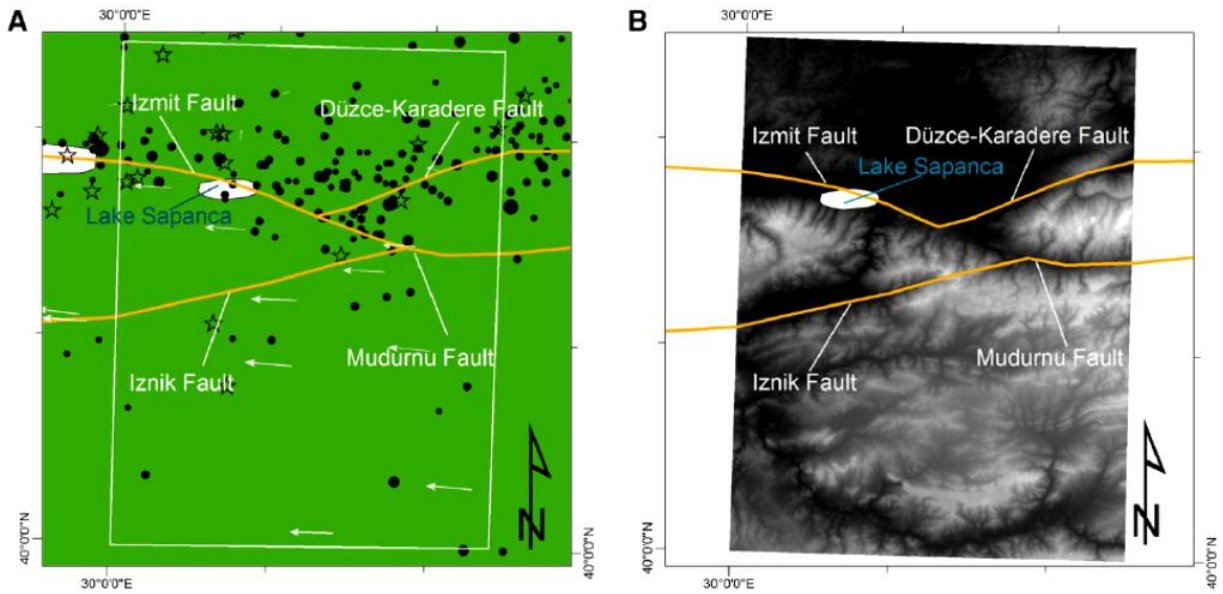

Figure 2.2 Possible fault geometries, GPS velocities, seismicity, and elevation data. A) A 100-year record of earthquakes (KOERI-UDIM, 2012) along the NAF sized according to magnitude with GPS vectors as arrows (Ozener et al., 2009), and location of focal mechanism data (Heidbach et al., 2008; International Seismological Centre, 2011) as stars. B) A 10 m resolution DEM of the region (USGS, 2008). The inferred linking fault can partially be traced along a river valley, but as it approaches the northern strand, the nature of the structure remains ambiguous.

Determining the geometry of the active fault system would allow for more detailed and accurate models of the stress accumulation along the NAF, one of the world's largest and most hazardous active strike-slip faults. Stress accumulation can be used to define a region with a higher probability for seismic risk (Bowman and King, 2001; Stein et al., 1997). This study utilizes simplified fault geometries and friction values, surficial geology, rock physics parameters, and GPS velocities as model inputs. We created simplified two-dimensional models for each of the fault geometries and processed them with a finite element method to evaluate primary stress orientations for the region. The stress orientations from the two models are compared to lineament analyses and a record of focal mechanisms from the region to determine

which geometry of active faults best reproduces the inferred stress field within an 85 km wide by 111 km long region centered around the Mudurnu Valley. We evaluate the accuracy of the generated stress field from the finite element model (FEM) by comparing it to regional focal mechanisms, and inferred paleostress orientations determined from relating lineaments to potential structures.

We utilize PyLith - a finite element code tectonic deformation software - (Aagaard et al., 2012) to calculate the stress field in the region of interest for both models and compare the σ_1 orientation frequency and magnitude of the stress field to the principal stress orientations suggested from lineament analyses and focal mechanisms. The overall goal of this study is to identify the active fault geometry of the NAF within the region of interest, which best duplicates the regional stress field as determined from focal mechanism data and lineament analyses.

2.2 GEOLOGIC BACKGROUND

The NAF forms the most prominent part of a strike-slip dominated belt of deformation between the Eurasian and Anatolian plates (Şengör et al., 2005). It extends from the junction of the NAF at the East Anatolian Fault (EAF) near the town of Karliova Turkey (Figure 2.1 A) to the north Aegean region (Şengör et al., 2005) nearly 1200 km, paralleling the southern margin of the Black Sea. East-west widening of a dextral shear zone associated with the NAF system continues across the northern Aegean sea, broadens across the northern and central mainland parts of Greece (the Grecian Shear Zone) (Şengör, 1979), and is postulated to link up with the Hellenic subduction zone (Dewey and Şengör, 1979; McKenzie and Jackson, 1983). The NAF system is mostly contained within late Paleozoic to early Tertiary age Tethyan accretionary complexes

(Şengör and Natal'in, 1996), which also widen from east to west (Şengör et al., 2005). The accretionary complex is bound by more resistant pan-African and Hercynian magmatic or metamorphic assemblages (Kröner and Stern, 2004): the Menderes and Kirşehir Massifs to the south, and the Istanbul zone and Eastern Pontides to the north (Şengör et al., 2005; Yılmaz et al., 1997). Magnitudes of fault displacement are not the same along the through-going NAF and generally decrease from east to west (Hubert-Ferrari et al., 2002; Şengör and Canıtez, 1982; Şengör et al., 2005). This implies that total displacement must be taken up by smaller faults within the greater NAF system that are not part of the through-going NAF. In addition, the age of fault initiation is older in the east than the west (Şengör et al., 2005). The bifurcation of the NAF west of Bolu is interpreted to be a result of westward widening in the zone of deformation that accompanied the westward development of the NAF. The Pleistocene northern strand borders the northern shores of the Marmara Sea, while the more poorly-defined late Miocene southern strand marks the southern sea edge (Şengör et al., 2005), and additionally splits and extends through the Bursa graben (Armijo et al., 2002). Şengör et al. (1985) and Le Pichon et al. (2003) note that the southern strand has yet to materialize a through-going main fault, and appears "fragmented". The complexity of such fragmentation can be seen within the Mudurnu Valley region of which we are modeling.

2.3 STRESS MODELING

2.3.1 Fault parameters

A wide range of proposed friction coefficients (μ) have been suggested for the NAF (Hergert and Heidbach, 2011; Jiménez-Munt et al., 2006; Kasapoglu and Toksöz, 1983; Provost et al., 2003; Stein et al., 1997). Provost et al. (2003) created a 3D mechanical model of the NAF and determined the friction coefficients (μ=0.05 to μ=0.1) necessary to match the calculated velocity field to the GPS velocity field. Stein et al. (1997) determine that the friction is μ=0.75 based on laboratory rock experiments, but also consider moderate pore pressure, as a Skempton's coefficient of B=0.5, which makes the effective friction (μ') 0.4. Early two-dimensional, plane-stress, finite element modeling of the NAF by Kasapoglu and Toksöz (1983) resulted in the faults locking at μ=0.4. This agrees with the thin-shell finite element tectonic model of the Mediterranean proposed by Jiménez and Sabadini (2006) who also predict that a very low friction (0.05) on the NAF is necessary to match the Anatolian block rotation seen by GPS measurements. Based on observations that large-offset plate boundary faults are weak, Hergert and Heidbach (2011) employ μ'=0.05 in their model of the NAF system in the Marmara sea. With so many discrepancies regarding the value of friction coefficient for the NAF, we use μ'=0.4, because it most closely matches experimentation by Byerlee (1978) while also considering a pore pressure value of 0.5. This value is applied to all the faults within the region in both models.

2.3.2 Geometry and rock properties

The faults defining the main strands of the NAF within our study area are nearly vertical (Ben-Zion et al., 2003) with strike-slip motion. As mentioned in section 1.1, two possible orientations of the active fault geometries exist within the region of interest: (Model 1) the two strands as distinct fault traces which don't interact west of Bolu, converge from east to west, but then diverge near the center of the region of interest and continue on to border the Marmara Sea in the north and south respectively (Armijo et al., 2002; Şengör et al., 2005), or (Model 2) that the southern strand links up with the northern fault through the Mudurnu Valley (Öztürk et al., 2009). West of the Mudurnu Valley, both models are identical as the northern strand and southern strands continue on to border the Marmara Sea (Figure 2.3).

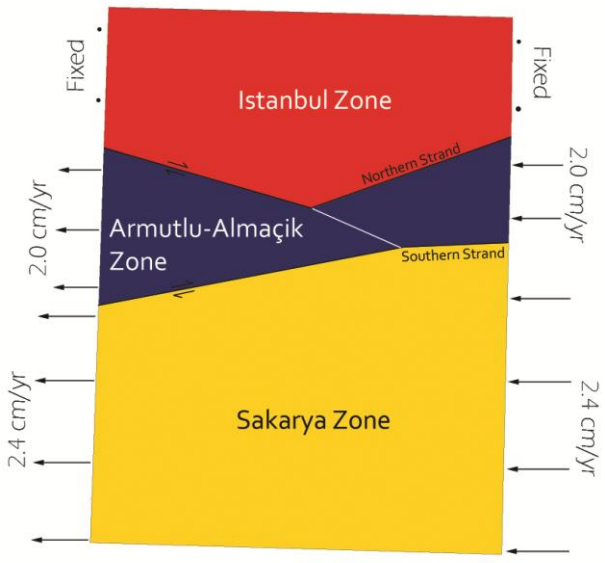

Figure 2.3 Simple geophysical model of the region of interest depicting the three zones, and the two strands of the NAF separating them. The white line (fault) connecting the two strands is the difference between Model 1 (without) and Model 2 (with).

We model the geometry of two distinct faults as boundaries which separate three distinct blocks/zones within the region of interest: the Istanbul zone north of the northern strand which is part of the Eurasian tectonic plate, the Armutlu-Almaçik zone between the two strands, and the Sakarya zone south of the southern strand (names adapted from Yılmaz et al. (1997)) (Figure 2.3). Each zone has distinct rock types exposed at the surface, which we use to determine average densities and seismic velocities - using empirical relationships - as inputs into our models. A breakdown of the surficial geology within each zone is provided in Table 2.1.

Table 2.1 Surficial geology and rock physics parameters - density, P-wave velocity, and S-wave velocity determined for the three blocks/zones within the region of interest using an empirical relationship between density and V_p at 10 MPa (DU/GSC, 2001), and a V_p/V_s ratio of 1.7 (Barton, 2007). The Istanbul Zone is mostly softer sedimentary rocks, the Armutlu-Almaçık zone is harder metamorphic and igneous packages, and the Sakarya Zone is mostly sedimentary units, but there are metamorphic and volcanic units present.

Zone	Surficial Geology	Density [kg/m^3]	Vp [m/s]	Vs (1.7) [m/s]
Istanbul	Devonian to Quaternary sedimentary units	2409	2323.9	1367.0
Armutlu-Almaçik	Nearly equal distributions of early Cenozoic sedimentary units, Paleozoic-Mesozoic metamorphic rocks, and Paleozoic-Early Cenozoic igneous rocks	2476	2913.9	1714.1
Sakarya	Mostly paleogene sedimentary units, some Paleozoic-Mesozoic metamorphic rocks, and Paleozoic igneous rocks	2501	3134.1	1843.6

Each block's density was calculated by weighting the general densities of the three rock types by their percentage of block area: 2,775 kg m^{-3} for igneous rocks (Bell, 2007), 2,400 kg m^{-3} for sedimentary rocks (Boyd, 2003), and 2,800 kg m^{-3} for metamorphic rocks (Boyd, 2003). The

densities calculated for each block were then used to extract compressional wave velocities (V_P) from the Database of Global Rock Properties by Dalhousie University/Geological Survey of Canada High Pressure Laboratory (DU/GSC, 2001). We used the V_P values for 10 MPa, as the 2-D model addresses the surface (near surface) geology, and we can assume a low confining pressure near the surface. From these compressional velocities we were able to calculate the shear wave velocities (V_S) using a V_P/V_S ratio of 1.7, which is the prescribed ratio for hard (zero-porosity) rocks (Barton, 2007). The empirically determined seismic velocities indicated a high-velocity for the Armutlu-Almaçik block relative to the Istanbul block, which is supported by local earthquake tomography by Koulakov et al. (2010). The resulting densities, V_P and V_S of each region were applied to their respective blocks in the model for processing with a finite element method.

2.3.3 Plate motions

The NAF, together with the conjugate East Anatolian Fault (EAF), accommodates the westward extrusion of the Anatolian plate toward the Aegean subduction zone (Hubert-Ferrari et al., 2008). The NAF and EAF meet near the town of Karliova at what is known as the Karliova triple junction of the Anatolian plate, the Eurasian plate, and the Arabian plate (Figure 2.1 A). Lateral forces acting upon the Anatolian plate include the NNW motion of the Arabian plate at its eastern flank, the northern motion of the African plate in the south and west (where it subducts beneath the Anatolian plate at the Cyprus and Hellenic trenches), and the fixed Eurasian plate in the north. The westward extrusion of the Anatolian plate likely started some 10-12 Ma during a late phase of collision between Arabia and Eurasia (Dewey et al., 1986; Hubert-Ferrari et al., 2008; McQuarrie et al., 2003) and initiating motion along the NAF (Barka, 1992; Şengör et al.,

1985). From GPS data, the Anatolian plate exhibits northwest motion along the East Anatolian Fault (EAF), and rotates counterclockwise to an orientation of southwest in the south Aegean region (McClusky et al., 2000; Reilinger et al., 2006). Current block motions of the Anatolian plate are 24 mm/yr in the central plate to 30 mm/yr in the SW part of the plate at the Hellenic trench (Gülen et al., 2002; McClusky et al., 2000; Reilinger et al., 2006).

Within the region of interest, the motions of each zone described in section 3.2 were determined from GPS campaigns conducted in Turkey. GPS measurements have been carried out at both campaign and permanent geodetic control points to measure/monitor crustal movements (Ergintav et al., 2002; McClusky et al., 2000; Ozener et al., 2009; Reilinger et al., 2006). We use the horizontal GPS velocities in a Eurasia-fixed reference frame of Ozener et al. (2009). In this reference frame the Istanbul zone is on the fixed Eurasian plate (0.0 cm/yr) the Armutlu-Almaçik zone moves westward at 2.0 cm/yr, and the Sakarya zone at 2.4 cm/yr west. These rates are used to push/pull the blocks past one another.

2.3.4 Simplified model

We simplified the potential fault geometries based on existing geologic maps and marked changes in topography identified on a DEM. The two potential geometries are identical except for the addition of a fault connecting the southern to northern strands at their bends in Model 2 (Figure 2.3). Each zone is assigned a density, P-wave velocity, and S-wave velocity (see Table 2.1). The northern and southern boundaries of the models are prescribed with roller conditions, and using the GPS velocities for each zone, the blocks are both pushed on their eastern boundary and pulled on their western boundary at their respective rates.

2.4 MODEL PROCESSING

We use PyLith (Aagaard et al., 2012), to process the models using finite elements. A triangular mesh over the region of interest was created with a grid spacing of 5 km along the outer boundaries and a finer grid of 2 km near the faults. The grid spacing are used as input to create a finer triangular mesh near the faults, which grades into a coarser mesh towards the outer boundaries. The models are processed using the rock physics and fault parameters described in section 2.3, and the block's respective velocities are applied as quasi-static dirichlet boundary conditions on the east and west bounds of the blocks. Once the friction is overcome, the blocks slip along the faults at a steady rate. The models are processed for a thousand years, at a five year time step interval, to allow the stress field to develop enough to cause slip along all the faults while avoiding large distortions within the model area due to displacements.

From the model we calculate the orientation and magnitude of the principal stresses at the center of each triangular cell. From this, rose-diagrams of σ_1 orientation frequencies for the two models were plotted to extract a general sense of the maximum principal component trends for the region (Figure 2.4). For model 1 (Figure 2.4 A), the largest peak associated with σ_1 can be seen at the interval from 055^o-060^o, with a second, almost equally large peak at 115^o-120^o. For model 2 (Figure 2.4 C), the largest peak can be seen at 120^o-125^o, with a second large peak at 100^o-105^o. Weighting the principal stress orientations by their respective magnitudes (as absolute values), we see that model 1 maintains its first strong peak, but the second peak appears at 125^o-130^o, with a minor peak at 90^o-105^o (Figure 2.4 B). This 'shift' in the location of the peaks are still within the same general azimuthal region $\pm 10^o$, except for addition of a 3rd, minor peak. Model 2 maintains its predominant peak, but the second peak becomes less prominent (Figure 2.4 D).

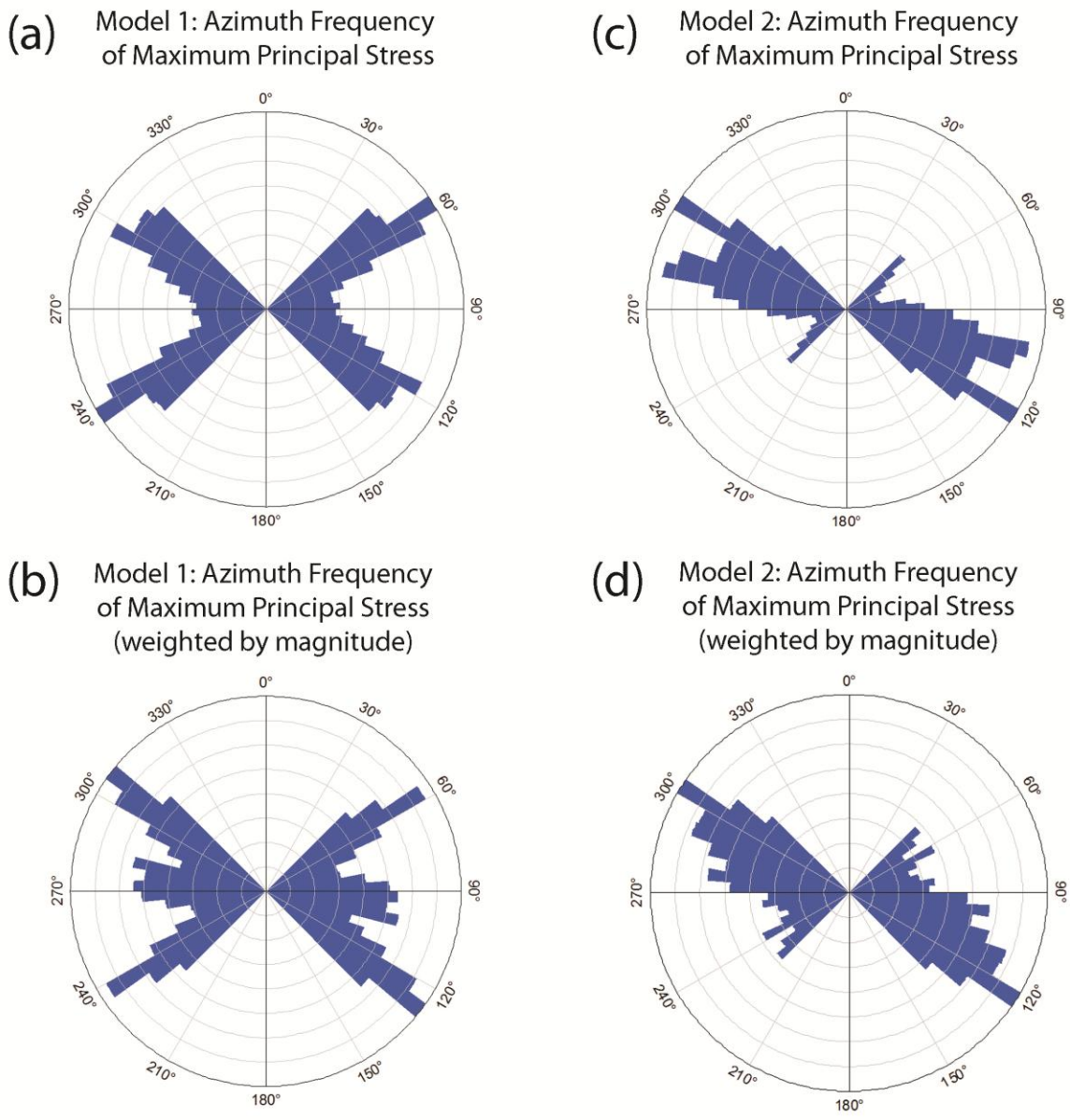

Figure 2.4 Rose diagrams of the model results depicting frequency and magnitude-weighted frequency of modeled azimuths of the maximum principal stress for model 1 (a,b) and model 2 (c,d). North is at 0°.

2.5 INFERRING MAXIMUM PALEOSTRESS ORIENTATIONS

Tectonic features such as faults and fractures may exert a strong control on topographic patterns due to these features creating pathways for weathering and erosion. Using digital imagery, we can highlight topographic lineaments and evaluate the potential control of tectonic induced deformation on topography. Tectonic features that may strongly influence topographic patterns include fault, large fracture systems and joints. These linear features can be mapped using digital imagery. Lineament mapping was manually performed using two sets of images: a 10-meter Digital Elevation Model (DEM) of Universal Transverse Mercator (UTM) zone 36N from the Global Land Cover Facility (GLCF) (USGS, 2008), and an Advanced Spaceborne Thermal Emission and Reflection radiometer (ASTER) product (AST14DMO) to highlight lineament patterns. The 10-meter DEM of the region was processed by applying hill-shades to highlight topographic changes. The hill-shades were performed at a 45^{o} vertical sun-angle, as linear features are most evident at this angle, and the azimuthal direction of the incoming solar radiation was rotated around the image at 45^{o} increments. For the ASTER image, the bands with the highest spectral resolutions (15 meters) are necessary to use in image processing and lineament picking - specifically band 3N in the Very-Near InfraRed (VNIR) region. A directional filter was applied at 45^{o} increments, creating a series of filtered images. The lineaments picked in these images specifically highlight differences in surface feature Digital Number (DN) values, which varies between materials. These DN value differences should highlight the main structures (such as fault displacement which juxtaposes two unique materials), and larger stream valleys, but also could further emphasize smaller scale linear features that may not show up in the resolution of the DEM, such as fluvial systems that do not exhibit prominent topographic valleys, but may take advantage of fractures and joints.

Lineaments were manually picked for both sets of images, allowing us to preferentially pick lineaments that are not man-made structures such as roads or railways. While there may be lineaments picked that do not have a tectonic source, they are outnumbered and outweighed by lineaments which are parallel to mapped faults (identified on geologic maps) (Akşay et al., 2002). To account for any curvature of lineaments we split each line into 10 sections and calculated the azimuth for each of those sections. Following this, an average azimuth and standard deviation were calculated for the orientation of each line. A very high majority of lineaments from both images had a standard deviation close to zero, but few exhibited higher deviations. The results of the average azimuths were plotted on rose diagrams (Figure 2.5). Work by Hisarli et al. (2011) on Eocene volcanic rocks indicated that there was counterclockwise rotation of the eastern half of the Armutlu-Almacık block (Almaçik) of 22.3^{o} and 17.7^{o} on the western half (Armutlu). We evaluated the impact of these rotations on the lineament analysis, and found there to be no changes to the prominent features in the rose plots of the lineament analyses.

The DEM lineament analysis results of orientation frequency (Figure 2.5 A), has its highest peaks between 80^{o}-90^{o}, which match the primary orientations of faults mapped within the region. Additionally, there is a region of strong frequencies between 60^{o}-130^{o} with the most predominant peaks at 60^{o}-65^{o} and 125^{o}-130^{o}. Without knowing if any faults within the region are reactivated structures, we assume that the structures that are reactivated are the ones optimally orientated in the driving stress field. Additionally, we assume the largest peak is indicative of the orientation of major strike-slip faults, and secondary peaks are likely to be associated with Riedel shear features such as R-shears, R'-shears, P-shears and extensional fractures. With this geometry, the maximum principal stress is 45^{o} clockwise (for right-lateral motion) from the main

faults and intersects two populations of lineaments interpreted to represent R-shears and R'-shears that are characteristic of strike-slip faulting (Davis, 1999; Riedel, 1929; Wilcox et al., 1973). Under this assumption, σ_1 would be at about 125^o-135^o. This inferred stress orientation overlaps with a secondary peak (125^o-130^o), that is at an appropriate orientation to represent extensional fracturing. By weighting the lineaments according to their length, (Figure 2.5 B), the dispersal of high frequencies disappears and we are left with a very strong feature trending 80^o-85^o, tightening our σ_1 orientation estimate to 125^o-130^o. The secondary peak, which corresponded with σ_1 almost disappears, which argues that if these are extensional fractures they are small and frequent. Plotting the location of our proposed extensional fractures on topographic and geologic maps indicate that they are oriented in stream valleys and around the edges of basins within the region. We propose that the 80^o feature is the "main fault" (MF) orientation and plot the potential orientation of Riedel shears (Figure 2.5 A/B); with R-Shears at 100^o, R'-shears at 160^o, and P-shears at 75^o. Both the average frequency as well as the frequency weighted by length show peaks in potential orientations of R and P shears. The presence of orientations corresponding to these shears helps validate the resolved orientation of σ_1.

The secondary peak at 60^o-65^o remains in both the unweighted and weighted cases (Figure 2.5 A/B), and does not correspond to any expected tensional or Riedel shear features. Since the lineaments oriented 60^o-65^o are less pronounced in the weighted rose plot (Figure 2.5 B), we analyze the distribution of these features, and additionally compare their orientation to mapped fault data. The DEM lineaments with this orientation are not centered in a particular region, and correspond to ridges and valleys that run nearly parallel to the Düzce-Karadere fault, the fault on the south east edge of the Istanbul zone (Figure 2.3). Mapped faults indicate that this

orientation further corresponds with southwest trending step-over portion of faults within the region.

Figure 2.5 C depicts the rose plot of the frequency average orientation of lineaments picked from the ASTER image. The ASTER image covered approximately a quarter the size of the DEM image near the center of the region of interest, but highlighted a greater number of lineaments (n=1835 versus n=1461 for the DEM). This lineament density increase is due to the smaller pixel size and DN value differences being highlighted rather than topography. Between 10^{o}-105^{o} there is a block of peaks, with major peaks are at 70^{o}-85^{o} and 55^{o}-65^{o}. The peak synonymous with the trend of mapped faults, 70^{o}-85^{o}, would predict an orientation of σ_1 between 115^{o}-130^{o}. The second major peaks are associated with portions of the NE-SW trending faults and step-over components of other faults. To a first order, all major peaks (and σ_1 orientations), overlap with those identified in the DEM lineament analysis. Weighting the results by the lengths of the lineaments (Figure 2.5 D), we continue to see a very strong feature at 70^{o}-85^{o}, but the second feature at 55^{o}-65^{o} diminishes to background levels. The possibility of Riedel shears is also present in the ASTER lineament data, but is more uncertain (Figure 2.5 C/D).

Combining the frequency of lineament orientations from the two datasets for the region (Figure 2.5 E), we see can see peaks at 60^{o}-65^{o}, 75^{o}-85^{o}, and 125^{o}-130^{o}. The peak at 125^{o}-130^{o} is once again attributed to small extensional fractures parallel to σ_1. When we weight the combined lineaments by their length (Figure 2.5 F), we are left with a strong peak parallel to the orientation of the mapped faults at 80^{o}-85^{o} (45^{o} from the inferred orientation of σ_1). Overall the combined (weighted) rose plot is very similar to the rose plot of the weighted DEM lineament analysis, indicating that though the density of lineaments from the DEM analysis were low, their lengths

helped them outweigh the smaller, lineament dense ASTER image. The potential of Riedel shears also exists within the combined dataset (Figure 2.5 E/F).

With agreement between the DEM and ASTER lineament analyses - and their combined dataset - the spread for the inferred maximum paleostress orientation is between 115^{o}-130^{o}, with a more likely orientation of 125^{o}-130^{o}. This is based on a dominant orientation of lineaments at around 80^{o}-85^{o} in the DEM and combined datasets, which correlates with the major orientation of mapped faults within the region. As a preliminary step to understanding the fault geometry in tectonically active areas with limited fault maps, we suggest that prominent features from a lineament analysis provide orientations that represent dominant fault populations. Thus, we can use the determined orientation for σ_1 from our lineament analyses to compare with the orientation of σ_1 based on the processed FEM to determine which model best represents the geometry of the through-going faults within the region.

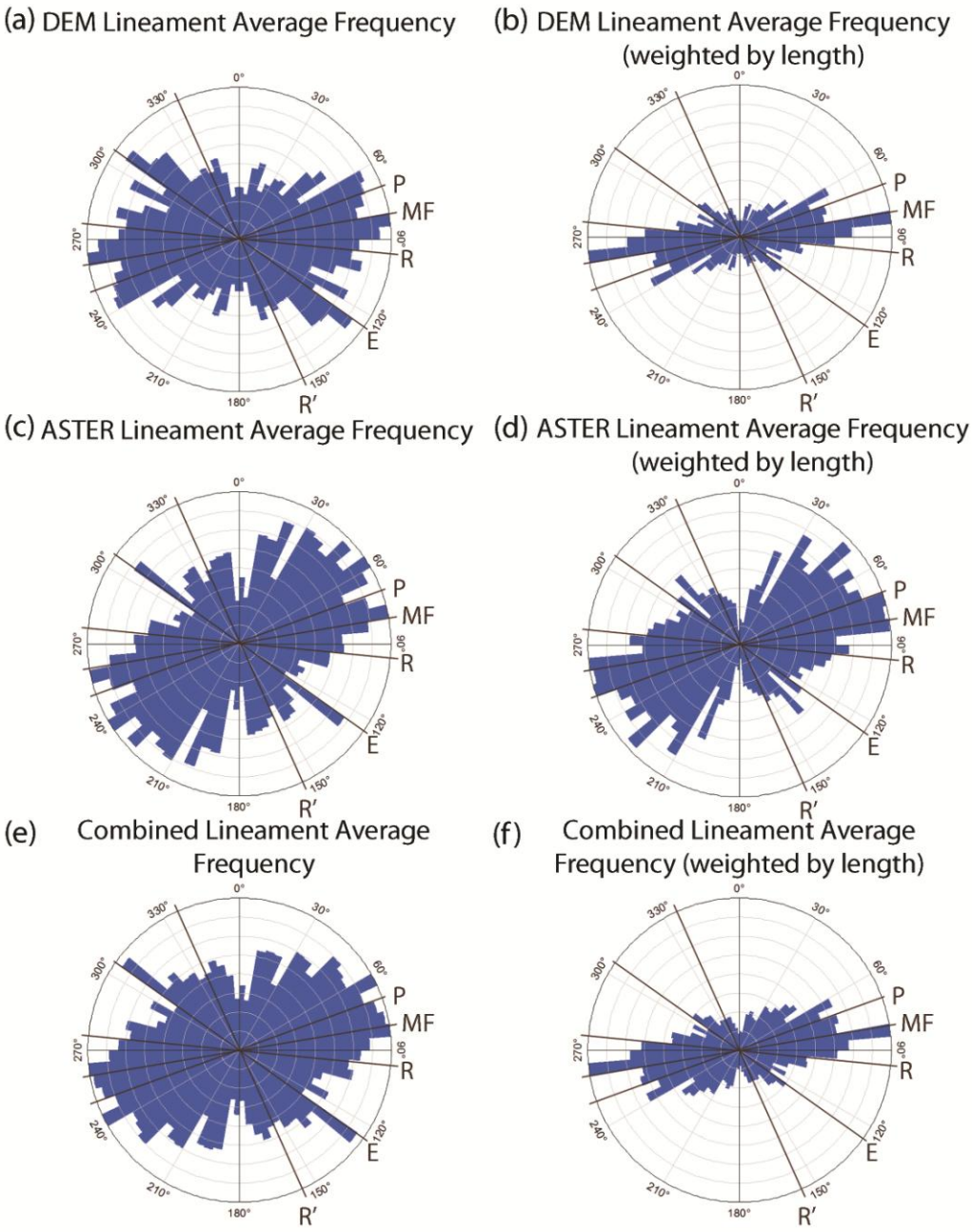

Figure 2.5 Rose-diagrams of lineament orientation frequencies and length-weighted frequencies for (a,b) the DEM lineament analysis, (c,d) the ASTER image lineament analysis, and (e,f) a combined lineament analysis. North is at 0°. Riedel Shears (R and R') are imposed on the images with the "main fault" (MF) at 80°. P shears are labeled with "P", and "E" represents the extensional fracture orientations. North is at 0°.interpretation

To evaluate which of the two models best represents the active fault geometry, we compare the maximum principal stress axes orientations from the finite element method results with the inferred principal stress axes from the lineament analysis. The maximum principal stress orientations of model 1 (115°-120°) and model 2 (120°-125°) have peaks that nearly coincide with the spread of inferred directions of σ_1 from the lineament analyses (115°-130°); however, model 2 results in a σ_1 orientation most close to the more likely orientation of 125°-130°. Model 1 shows a very large trend for σ_1 from 55^o-60^o. This orientation is located on the Armutlu-Almaçik block just south of the Düzce-Karadere fault portion of the northern strand, at which we would expect it to host a σ_1 orientation of 105^o. To evaluate how this orientation occurred, we looked into the time series deformation of the blocks. As the blocks are pushed/pulled, the lack of a fault linking the bends in the northern and southern strands allows for the eastern part of the Armutlu-Almaçik zone to be pulled and distorted by the western portion of the Sakarya zone, subsequently rotating clockwise away from the Istanbul zone. This creates an extensional opening due to counterclockwise block rotation along the NE-SW trending portion of the northern strand (Düzce-Karadere Fault). Additionally, this unexpected σ_1 trend occurs as a dominant orientation from the center of the Armutlu-Almaçik block to the western most portion, particularly along the Iznik portion of the southern strand, at which we would expect a σ_1 orientation of 105^o (based on the fault orientation). Model 2, displays only one principal stress orientation (120°-125°) that overlaps with the inferred orientation from the combined lineament analysis (115°-130°), and while Model 2 shows a fan of principle stress orientations from 135° to 45°, when these orientations are weighted for magnitude, they are notably smaller than the peak centered between 135° and 95°. While there is still a peak at 55^o-60^o, the peak is rather small and distributed within the bodies of the blocks, rather than bounding the faults. Though the lineament

analyses indicate that both models reproduce the inferred maximum stress orientation, the additional maximum stress orientations in the model 1 output are not observed, indicating that model 2 is the most likely candidate for best representation of fault geometry. To confirm this we will compare the FEM stress orientation results with data from seismic events.

We collected thirty-four focal mechanism data (Figure 2.2 A) associated with several seismic events and/or their aftershocks (1943 Adapazarı-Hendek, 1957 Abant, 1967 Mudurnu, and 1999 Izmit earthquakes) located in our study area from the International Seismological Centre (International Seismological Centre, 2011) and the World Seismic Map (Heidbach et al., 2008). Data from these two sources are recordings from global stations. We determined the trend of the maximum principal stress axis, which is assumed to be synonymous with the P kinematic axis. Applying density contours to the P kinematic axes, we were able to procure a nearly horizontal ($<5^o$) orientation for the regional P axis at approximately 125^o. As this value is nearly horizontal, we can assume that the derived regional orientation of the P kinematic axis is synonymous to the orientation of the maximum horizontal stress. The orientation of 125^o also matches the σ_1 orientation (low to no plunge) determined by Kiratzi (2002), Bohnhoff et al. (2006), and Örgülü (2011). This orientation falls within the range for the orientation of maximum principal stress determined from both FEM models. To further analyze the focal mechanism data, we looked at each focal mechanism separately and compared it to the immediate FEM stress orientations from both models within a buffer of 10 km around the epicenter. While both models exhibited stress orientation values similar to the individual focal mechanisms they corresponded to, Model 1 orientations showed the greatest deviation from focal mechanism orientations of σ_1, particularly along the Düzce-Karadere fault. Deviations from the focal mechanism data can be associated with the comparison of 3D focal mechanisms, with 2D

model results. In the latter, orientations are assumed to have no plunge, and this could subsequently increase the deviation of model stress orientations as compared to focal mechanisms, especially when focal mechanism P-axis attitudes exhibit a plunge greater than 30^{o}. In addition, the majority of focal mechanisms are deeper than what the 2D model represents, which is the upper 0.5-1.0 kilometers of crust. The focal mechanisms of the earthquakes are as deep as 15 km, at which point the fault geometry could potentially vary. However, based on the smaller deviation exhibited, model 2 best represents the fault geometry within the region.

2.6 CONCLUSION

The methodology presented in this paper can be used to remotely identify approximate active fault geometries, which may not have well-developed surface expressions. Through an integrative approach of stress modeling with remote sensing techniques, the active fault geometry with the linking fault in model 2 best explains the primary stress orientations as observed from deformation patterns and earthquake focal mechanisms within the region of interest. The absence of a linking fault (model 1) led to multiple maximum stress orientations not evident in the inferred paleostress or earthquake focal mechanism data, and is attributed to clockwise rotation away from the Istanbul zone of the eastern Armutlu-Almaçik zone as its western portion pulled and distorted it. The presence of the linking fault in the model removes distortion, and allows for transfer of displacement, thus playing an important role in the development of the regional stress field. Although the valley in the southern portion of the Mudurnu region has previously been interpreted to host a fault with both extensional and strike-slip kinematics based on both topographic and seismic data (Armijo et al., 1999; Şengör et al.,

2005), we show that it continues northward and it is an important linking feature of the NAF system. As a linking structure, this fault must be a significant component in future models of the NAF system in this region. It is predicted to facilitate long-term slip transfer and future modeling will help determine if the linking structure impedes or facilitates earthquake rupture propagation.

3.0 THE IMPORTANT ROLE OF COHESION IN GEOPHYSICAL MODELS THROUGH MODELING ESTIMATES OF STATIC FAULT PARAMETERS: A STUDY OF THE NORTH ANATOLIAN FAULT EAST OF THE MARMARA SEA

Experimental and numerical methods determining the strength of faults explore the static coefficient of friction (μ) and cohesive strength (C) of interfaces comprised of various materials. While generally accepted that weak faults have low friction coefficients ($\mu \leq 0.25$), there has been no consensus on the role of cohesion of fault gouge material on the strength of tectonic faults, and most studies simply neglect cohesive strength completely. We develop numerical models to evaluate estimates of static friction and cohesion along a portion of the NAF east of the Marmara Sea. Using a viscoelastic finite element analysis, we found that a minimum cohesion, in the range of 300 to 500 KPa, is needed to match both fault recurrence intervals, and magnitudes of slip on the NAF given a high variation of static friction coefficient between 0 and 1. Without cohesion, rupture times occur too quickly to match the geologic record for all values of static friction. Our study shows that cohesion, even of small magnitude, plays a significant role in the strength of a fault, especially when the coefficient of friction is low. We compare our results of cohesion and coefficient of friction, which best match the recurrence interval and total slip of faults, to numerical and laboratory experiments on the strength of faults and their gouge material. This leads us to suggest a static friction coefficient of $\mu \leq 0.2$, and a cohesion of C=500 kPa for numerical modeling of the NAF.

3.1 INTRODUCTION

Plate tectonic boundaries source the majority of earthquakes and deformation at the Earth's surface, so understanding the strength of faults and the processes that control earthquake rupture - particularly at plate boundaries - is crucial. The strength of a fault is best described by the parameters which define when it will fail. Fault failure depends on the static coefficient of friction (μ) and the cohesive strength (C). Assuming no cohesive strength - which further assumes a rough, clean discontinuity surface with rock-to-rock contact and no infilling (Wyllie, 1999) - the ratio of shear stress to the normal stress required to initiate sliding on the fault plane is the static coefficient of friction. However, cohesion is developed on fault planes in many conditions, and even a small cohesion can have a significant effect on the strength of a fault (Wyllie, 1999). To determine the static coefficient of friction and cohesion of a fault, two approaches are typically used: rock friction experiments in a laboratory, and numerical modeling of the fault system.

There has been no consensus on the role of cohesion of fault gouge material on the strength of tectonic faults. Rock friction experiments generally take samples from the fault zone and simulate stresses acting on the fault until it slides, thus determining the frictional resistance of the interface from the velocity of sliding. One of the most intensively studied plate boundary strike-slip faults is the ~1,300 km long dextral San Andreas Fault (SAF). In 2007, the San Andreas Fault Observatory at Depth (SAFOD) borehole intersected a creeping segment of the SAF, recovering samples of the fault zone from seismogenic depths (Carpenter et al., 2012). These samples have undergone a series of laboratory experiments to determine the fault parameters for the SAF. Carpenter et al. (2011) describe a friction of μ=0.21 with an assumed 0.0 MPa cohesion. Further experimentation resulted in a range of μ=0.09 to μ=0.25 for the friction of

the fault zone material with the lowest values being closest to the fault plane (Carpenter et al., 2012), again assuming no cohesion. Experimentation on fault zone rocks by Lockner et al. (2011) indicated a low friction of μ=0.15 from velocity-stepping sliding experiments, while also assuming the fault to be cohesionless. The weakness of the fault was attributed to presence of smectite within the fault gouge. Frictional sliding experiments on reconstituted gouge (lacking in-situ fabric) at room temperatures by Tembe et al. (2006) resulted in a range of friction of μ=0.4 to μ=0.55, but without any mention of cohesion. To describe the Coulomb stress change for the ~1200 km dextral North Anatolian Fault (NAF) in Turkey, Stein et al. (1997) assume an effective friction (μ') of 0.4 based on laboratory rock experiments by Byerlee (1978), with a moderate pore pressure, as a Skempton's coefficient of B=0.5 (Stein et al., 1997). Again, no mention is made regarding cohesion along the NAF interface (Stein et al., 1997).

Coefficients of friction derived from numerical models, or utilized in them, vary greatly for the SAF. Using modeled versus pilot hole stress data, work by Chéry et al. (2004) showed that μ<0.1 applied to their model is required to match both the far field and the pilot hole stress data, assuming no cohesion. Chang et al. (2011) determine an average frictional estimate of μ=0.38 following the 2004 Mw 6.0 Parkfield, California earthquake, using a co-seismic slip model constrained from seismological and geodetic data to compute the co-seismic stress change on the SAF, and predict the time evolution of slip. One of the highest values of friction utilized to model the SAF is by Johnson et al. (2006), who assume a friction of μ=0.6, matching estimates derived from early laboratory work by Byerlee (1978).

A 3D mechanical model of the NAF by Provost et al. (2003) determined a range of friction coefficients (μ=0.05 to μ=0.1) necessary to match the calculated velocity field to the GPS velocity field. Although Stein et al. (1997) assumed a friction of μ'=0.4 to determine the

Coulomb stress change, early two-dimensional, plane-stress, finite element modeling of the NAF by Kasapoglu and Toksöz (1983) resulted in the faults locking at μ=0.4 due to the developing stress field being unable to overcome the strength of the fault. Jiménez et al. (2006), through modeling of the NAF using a thin-shell finite element tectonic model of the Mediterranean, agree that the NAF locks at friction values above μ=0.4. In addition, they predict that a very low friction of μ=0.05 is necessary to match the Anatolian block rotation seen by GPS measurements. Based on observations that large-offset plate boundary faults are weak, Hergert and Heidbach (2011) employ μ'=0.05 in their model of the NAF system in the Marmara sea. None of the numerical models that evaluated the NAF employ non-zero values for cohesion. Similarly, numerical models of other large strike-slip faults indicate a low static friction coefficient, and assume no cohesion (Jolivet et al., 2013), or do not mention cohesion (Ellis et al., 2006; Lachenbruch and Sass, 1980).

From the numerical methods described above, the range of possible friction values for tectonic strike-slip faults is quite large. Furthermore, previous numerical and experimental work did not evaluate the impact of cohesion; however, cohesion is developed on fault planes in many conditions, and even a small cohesion could have a significant effect on the strength of a fault (Wyllie, 1999). By "tuning" friction estimates in their model and comparing modeled slip rates to geologically determined slip rates along the SAF, Chéry et al. (2001) determined that a value of friction less than <0.18, assuming a cohesion of 1 MPa, best matched geologic slip rates. This paper will follow a similar approach and evaluate which estimates of the static coefficient of friction and cohesion produce modeled rupture times and total slip that best match recurrence intervals - a proxy for the time it takes to build up stress from a relaxed state to fault rupture - and slip magnitudes along the NAF. We show that cohesion is a necessary value, which must be

included in geophysical models. While we only discuss tectonic strike-slip faults, the methodology and implications are applicable to other types of faults.

3.2 GEOLOGIC BACKGROUND

The NAF forms the most prominent part of a strike-slip dominated belt of deformation (shear zone) between the Eurasian and Anatolian plates (Şengör et al., 2005), paralleling the southern margin of the Black Sea. The dextral shear zone associated with the NAF system widens further west, and continues to broaden across the northern Aegean sea into Greece (the Grecian Shear Zone) (Şengör, 1979), and is postulated to link up with the Hellenic subduction zone (Dewey and Şengör, 1979; McKenzie and Jackson, 1983). The NAF system is mostly contained within late Paleozoic to early Tertiary Tethyan accretionary complexes (Şengör and Natal'in, 1996), which also widen from east to west (Şengör et al., 2005). Due to the broad nature of the shear zone west of the town of Bolu, the through-going NAF bifurcates into two main strands: a northern strand bordering the northern shores of the Marmara Sea, and a poorly-defined southern strand which trends towards the southern Marmara sea edge (Şengör et al., 2005) (Figure 3.1 A). The eastern through-going NAF structure initiated approximately 10-12 Ma ago, contemporaneously with the southern strand, while the northern strand formed at approximately 200 ka (Şengör et al., 2005). Decreases in fault displacement westward along the northern and southern strands of the NAF imply that total displacement in the west must be taken up by smaller faults within the greater NAF system that are not part of the through-going NAF (Hubert-Ferrari et al., 2002; Şengör and Canıtez, 1982; Şengör et al., 2005).

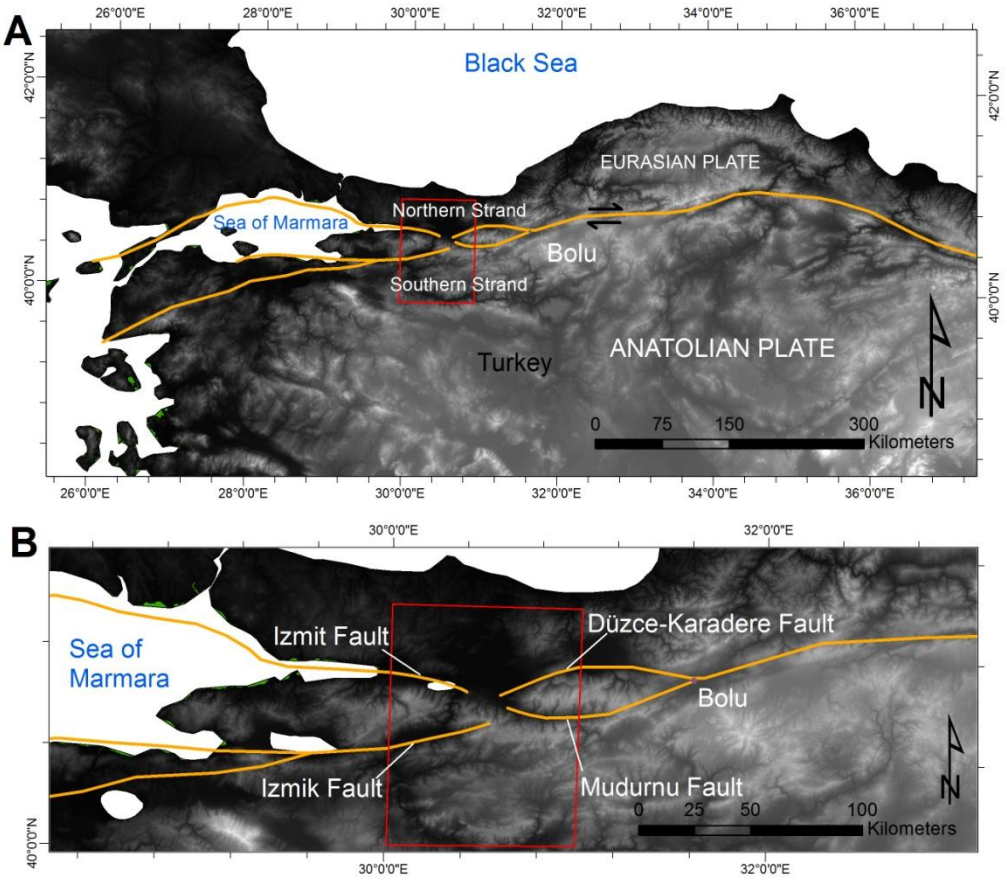

Figure 3.1 Tectonic setting of the NAF and region east of the Marmara Sea. A) The NAF and its bifurcation into the northern and southern strands west of the town of Bolu, and B) fault names within the region of interest at the Mudurnu valley. The red box represents the modeled region of interest.

The complexity of fault fragmentation along the western NAF can be seen around the Mudurnu valley region, where the two strands almost converge. Our region of interest is an 85 km wide by 111 km long region centered on the Mudurnu valley, containing the northern strand comprised of the Düzce and Karadere faults (simplified as the Düzce-Karadere fault) and the Izmit fault, while the southern strand is comprised of the Mudurnu and Iznik faults (Figure 3.1 B). The strike-slip faults of the NAF within our study area are nearly vertical (Ben-Zion et al., 2003). Recurrence intervals of M_w>6.0 earthquakes for the Mudurnu Valley and Düzce-Karadere and faults are 100-150 years (Palyvos et al., 2007) and 300 years, respectively. The Düzce-

Karadere fault displayed an earthquake recurrence interval of 360-560 years pre ~1 ka while the three most recent earthquakes recurred at intervals of 140-250 years (Pantosti et al., 2008). We simplify the earthquake record by utilizing a median of 300 years for the this fault. The recurrence intervals are used as a proxy for the length of time required to build up stress to rupture the faults from a relaxed condition. We evaluate the range of viable values for static friction and cohesion by comparing the recurrence intervals for the Mudurnu and Düzce-Karadere faults to the time it takes the modeled faults to rupture >1 m along at least 50% of their lengths. Additionally, we compare the modeled fault slip to the maximum fault slip (5 m) on the Izmit fault following the August, 1999 Izmit earthquake sequence, which was the largest sequence recorded by modern digital networks in the history of Turkish earthquakes (Özalaybey et al., 2002). The M 7.4 earthquake, which originated along the Izmit fault at the boundary of our region of interest, exhibited a maximum slip of 5 m (Barka, 1999). By comparing rupture times of the Mudurnu and Düzce-Karadere faults in our model to their recurrence intervals and the modeled slip on the Izmit fault to its documented slip magnitude, we evaluate the range of viable values for static friction and cohesion along the NAF.

3.3 GEOPHYSICAL MODEL

We employed a 2-dimensional simplified fault model, representing the upper kilometer of crust, with velocity boundary conditions describing the active NAF system near the Mudurnu valley. We simplified the geometry of the two distinct fault strands as boundaries which separate three distinct blocks/zones within the region of interest: the Istanbul zone above the northern strand which is part of the Eurasian tectonic plate, the Armutlu-Almaçik zone between the two strands

and the Sakarya zone below the southern strand (names adapted from Yılmaz et al. (1997)) (Figure 3.2). The Mudurnu portion of the southern strand and the Izmit fault are linked completely through the Mudurnu valley (Karimi et al., 2014) (Figure 3.2). We consider the linking feature to be a NW extension of the Mudurnu fault. In strike-slip systems, these short extensional faults linking echelon fault segments allow for long-term transfer of fault slip, thus affecting the stress field distribution, and may also act as kinetic barriers impeding or arresting rupture propagation (King, 1986; King and Nábělek, 1985; Sibson, 1986).

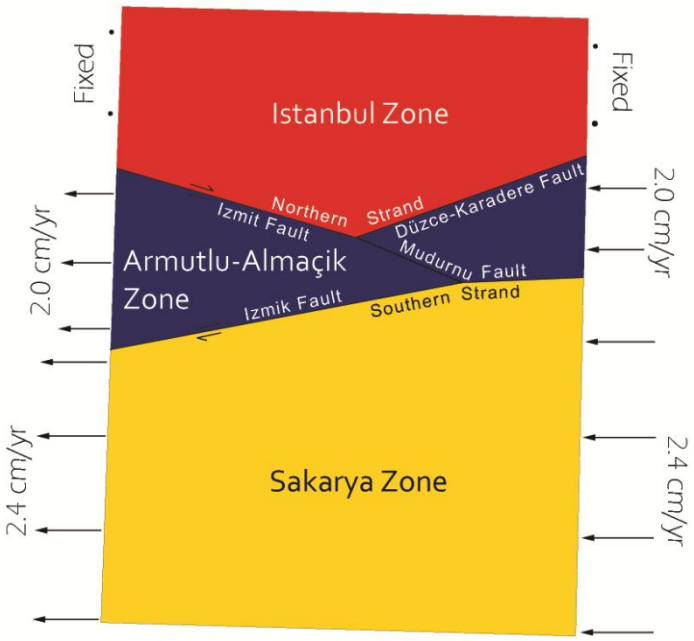

Figure 3.2 Simplified fault model. Location of the Izmit, Izmik, Düzce-Karadere, and Mudurnu faults along the northern and southern strands within the simplified fault model, as well as the velocity boundary conditions applied to the model. The Istanbul remains fixed while the two zones below are pushed and pulled westward at different rates.

Each of the three zones has distinct rock types exposed at the surface. We simplified the geology at the surface to the three basic rock types: igneous, sedimentary and metamorphic.

Their average densities were used to calculated rock physics parameters for each zone. Each block's density was calculated by weighting the densities of the three rock types by their percentage of block area. The densities determined for each block were then used to extract compressional wave velocities (V_P) from the Database of Global Rock Properties by Dalhousie University/Geological Survey of Canada High Pressure Laboratory (DU/GSC, 2001). We used the V_P values for 10 MPa, as the 2-D model addresses the surface (the upper kilometer) geology. From these compressional velocities we evaluated the shear wave velocities (V_S) using a V_P/V_S ratio of 1.7, which is the prescribed ratio for hard (zero-porosity) rocks (Barton, 2007). The resulting densities, V_P and V_S of each region were applied to their respective blocks in the finite element model.

Velocity boundary conditions were determined from GPS campaigns conducted in Turkey. GPS measurements have been carried out at both campaign and permanent geodetic control points to monitor crustal movements since 1994 (Ozener et al., 2009). Additional GPS campaigns were performed by a collaborative project of Boğaziçi University (BU), Massachusetts Institute of Technology (MIT), Turkish Scientific and Technological Research Council (TUBITAK), General Command of Mapping (GCM), and Istanbul Technical University (ITU) (Ozener et al., 2009). Information about this collaboration and the network(s) they deployed can be found in Ergintav et al. (2002). We use the horizontal GPS velocities in a Eurasia-fixed reference frame of Ozener et al. (2009). In this reference frame, the Istanbul zone is on the fixed Eurasian plate (0.0 cm/yr), the Armutlu-Almaçik zone moves westward at 2.0 cm/yr, and the Sakarya zone at 2.4 cm/yr west. These rates were assigned to the model blocks to push them at their eastern boundaries and pull them at their western boundaries (Figure 3.2).

3.4 METHODS

We applied a triangular mesh over the region of interest with a grid spacing of 5 km along the outer boundaries and a finer grid of 2 km near the faults. The grid spacing is used as input to create a finer triangular mesh near the faults, which grades into a coarser mesh towards the outer boundaries. We use PyLith (Aagaard et al., 2012) to process the viscoelastic finite element model. The GPS-determined velocities were applied to their boundaries as quasi-static dirichlet boundary conditions on the east and west bounds of the blocks. The simplified fault geometry, block boundary velocities, and associated rock physics parameters remain unchanged, while the fault parameters - static friction coefficient and cohesion - are changed in every simulation. We tested friction values of μ=0.0 to μ=1.0 at an interval of 0.05 for cohesion values from C=0 kPa to C=700 kPa at an interval of 100 kPa. Each simulation was processed for 400 years at 5 year time step intervals.

The output of each simulation were analyzed to determine at what time step the Mudurnu and Düzce-Karadere faults experienced enough stress to cause a slip >1 m along 50% of the modeled fault lengths. The time steps were recorded and compared to the recurrence interval for each fault - used as a proxy of the time it takes for stress to build up from a relaxed state and rupture the fault. Rupture times considered "probable" for the Mudurnu fault ranged from 100-150 years, and 275-325 years for the Düzce-Karadere fault. A 25 year additional buffer beyond the upper and lower limits were considered "potential." When constraints on the rupture time of the Mudurnu and Düzce-Karadere fault are met by the model results, the total slip along the Izmit fault for comparison to the maximum slip inferred from the geologic record is also recorded. Where maximum modeled slip is 5 m, we are able to constrain the results further. It is important to note that our model is of a long-term slip study, and does not including any sort of

healing; therefore, once rupture occurs on a fault, slip continues at a steady rate. Fault healing at the fault interface would require some sort of slip maximum, slip-rate, or time interval at which healing is applied. Since we compare model results to slip magnitude and rupture time, healing factors would be redundant as both an input and evaluation of the model.

3.5 RESULTS

The time steps at which the Düzce-Karadere and Mudurnu faults ruptured >1 m along 50% of their lengths for each of the various cohesion and static friction coefficient pairs are recorded in Table 3.1. By comparing the amount of time for rupture in the model to the documented earthquake recurrence intervals for the faults, we find that conditions are met when cohesive values are between C=300 kPa and C=700 kPa. At C=300 kPa, the conditions are met at higher static friction coefficient values, whereas with higher cohesive strengths, the range of possible static friction coefficient values decrease. Table 3.1 includes the results of the maximum slip experienced on the Izmit fault when both rupture time conditions had been met. The range of friction values decreases for each cohesion interval.

Table 3.1 Rupture time and slip of static fault condition simulations.Time (in years) of >1 m rupture along 50% the Düzce-Karadere (D-K) and Mudurnu (MV) faults for each static friction coefficient and cohesion pair simulation. Green represents the probable results, while orange represents the potential results. Maximum slip on the Izmit fault is recorded for the probable and potential results. Bold borders highlight the additionally constrained ranges of maximum slip along the Izmit fault based on the 1999 Izmit earthquake.

Static Friction Coeff.	Cohesion (kpa)																							
	Izmit Slip (m)	D-K	MV	Izmit Slip (m)	D-K	MV	Izmit Slip (m)	D-K	MV	Izmit Slip (m)	D-K	MV	Izmit Slip (m)	D-K	MV	Izmit Slip (m)	D-K	MV	Izmit Slip (m)	D-K	MV	Izmit Slip (m)	D-K	MV
	0			100			200			300			400			500			600			700		
0.00		65	175		100	215		145	200		185	165		225	145	5	265	140	6	305	140	7	345	135
0.05		65	180		105	215		145	190		185	160		230	140	5	270	140	6	310	140		355	135
0.10		65	185		105	215		150	190		190	155		235	140	5	275	135	6	320	145		360	135
0.15		70	190		110	215		155	190		195	150		240	140	5	280	135	6	325	135		370	135
0.20		70	195		110	215		160	185		200	150		245	140	5	290	140	6	330	140		375	135
0.25		70	195		115	205		160	175		205	150	5	250	140	5	295	140	6	340	135		385	135
0.30		70	200		115	200		165	175		210	145	5	255	140	6	300	135	6	345	135		395	135
0.35		75	205		120	195		170	165		215	145	5	265	140	6	305	135		355	135		400	135
0.40		75	205		120	190		170	165		220	140	5	270	140	6	320	135		365	135		>400	135
0.45		75	205		125	190		175	165		225	140	5	275	140	6	325	140		380	135		>400	135
0.50		75	210		130	180		185	155		235	140	5	280	135	6	335	135		390	135		>400	130
0.55		75	210		130	180		185	155		240	140	5	290	135	7	350	135		400	140		>400	135
0.60		80	210		135	175		190	155		245	140	6	300	135		360	135		>400	135		>400	135
0.65		80	210		135	175		195	150	5	255	140	6	310	140		370	135		>400	135		>400	135
0.70		80	210		140	175		200	150	5	260	135	6	320	135		380	135		>400	135		>400	135
0.75		80	205		145	170		205	145	5	270	135	6	330	135		385	135		>400	135		>400	135
0.80		85	205		150	170		215	145	5	280	135	6	345	135		400	135		>400	135		>400	135
0.85		85	205		155	165		220	145	5	290	135		355	135		>400	135		>400	135		>400	135
0.90		85	205		160	165		230	140	6	300	135		370	135		>400	135		>400	140		>400	135
0.95		85	200		165	160		240	140	6	310	135		380	135		>400	135		>400	140		>400	140
1.00		85	195		170	155		245	140	6	320	135		390	135		>400	130		>400	140		>400	145

3.6 DISCUSSION

Assuming constant shear and normal stresses, the relationship between the static friction coefficient and cohesion is inverse; if we increase cohesion, the value for the static friction coefficient must decrease. This inverse relationship is seen in our results. As the cohesion increases the range of permissible values of static friction coefficient decreases. This indicates that our results are not due to random error because they match the prescribed Coulomb failure criterion along the faults.

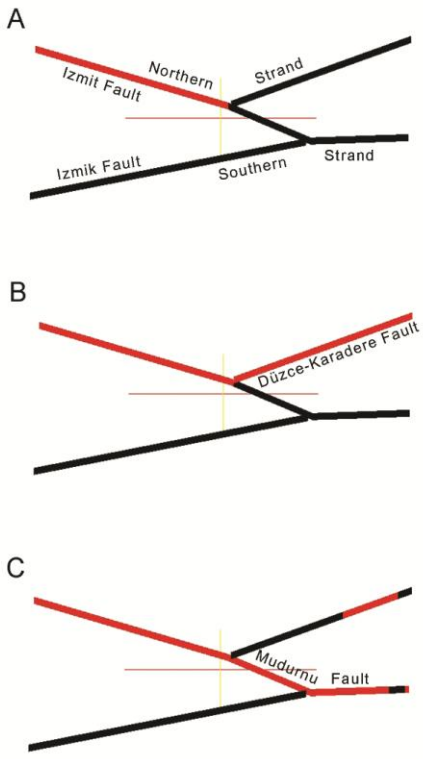

Figure 3.3 Progression of slip on modeled faults. Fault model depicting slip >1 m (red). (A) At early time steps the slip progresses eastward along the Izmit fault, at which point it will (B) continue along the Düzce-Karadere fault, or (C) continue down to the southern strand along the Mudurnu fault, leaving the Düzce-Karadere fault to independently rupture.

Our model assumes that the previous earthquakes on the Düzce-Karadere and Mudurnu faults occurred simultaneously at time zero. This coincidence is not always representative of the typical earthquake pattern in the region, as is seen by the last major rupture of the Düzce-Karedere (Akyüz et al., 2002), and Mudurnu faults (M_w 7.1, 1967) (Palyvos et al., 2007). In our model, slip begins at the western end of the Izmit fault and progresses eastward until the junction of the Izmit, Düzce-Karadere, and linking faults (Figure 3.3 A). At this point two slip patterns emerge. In the first, the leading edge of slip progresses immediately from the Izmit to the Düzce-Karadere fault and continues to propagate eastward, leaving the Mudurnu fault to rupture independently from the stresses acting on the leading edge of slip progression in the northern strand (Figure 3.3 B). This happens with low cohesion values (0-200 kPa). In the second, the leading edge of slip migrates southward along the Mudurnu fault, leaving the Düzce-Karadere segment to rupture independently (Figure 3.3 C). At higher cohesion values (>300 kPa), the junction facilitates fault slip from the Izmit fault to the Mudurnu fault (Figure 3.3 C), and at lower cohesions it impedes this pattern, instead favoring slip from the Izmit fault to the Düzce-Karadere fault (Figure 3.3 B). It is expected that short extensional faults linking echelon fault segments allow for the long-term transfer of fault slip, and may also act as kinetic barriers impeding or arresting rupture propagation (King, 1986; King and Nábělek, 1985; Sibson, 1986).

To match this observation, our simulations for the constrained static friction coefficient and cohesion should allow for the long-term transfer of slip along the linking portion of the Mudurnu fault, while impeding or arresting slip at its junction with the Düzce-Karadere fault portion of the northern strand. The slip pattern for the model simulations within the constrained ranges of static friction and cohesion for the NAF indicate that the junction of the northern strand

with the Mudurnu fault does arrest the progression of slip from the Izmit fault for several time steps before continuing down the Mudurnu fault. Thus it allows for long-term stress transfer from the Izmit fault portion of the northern strand to the southern strand. Additionally, within simulations of the constrained ranges of our fault strength parameters, this junction impedes fault slip propagation along the Düzce-Karadere fault portion of the northern strand (Figure 3.3 C).

A very important implication of our constrained results is that cohesion is a necessary component in geophysical models of the NAF. Without cohesion, the Düzce-Karadere fault ruptures earlier than the Mudurnu fault (Table 3.1), suggesting its recurrence interval would be more frequent than that of the Mudurnu fault. This is in contrast to the EQ recurrence interval of 300 yrs on the Düzce-Karadere and 100-150 yrs on the Mudurnu fault. The cohesion necessary to predict fault rupture times consistent with earthquake recurrence intervals suggests that even with small cohesions, up to C=200 kPa, the modeled Düzce-Karadere fault still ruptures first. A lack of cohesion force suggests a fully ruptured fault with no healing along the fault plane, and no infilling. The cohesion necessary to constrain ranges of modeled static friction that match the geologic constraints suggest that discontinuities between the fault blocks are filled with some sort of cohesive material. According to Wyllie (1999), the material formed in fault and shear zones in rocks can contain clays as well as granular fragments. These materials will still exhibit a low cohesion (up to C=380 kPa) (Wyllie, 1999). However, calculations based on rock experiments by Muhuri et al. (2003) indicated a strengthening of the cohesion up to 8 MPa along a fault during hold times between simulated fault ruptures. Additionally, experimental work by Tenthorey and Cox (2006) on samples over a range of temperatures and pore fluid pressures tested, indicated that their experimental fault zones exhibited an increase of cohesion to 5-30 MPa due to the presence of clay-infilling developing in the fault gouge. Our results are at least

one order of magnitude less than those suggested by Muhuri et al. (2003) and Tenthorey and Cox (2006), but slightly higher than averages suggested by Wyllie (1999). Barton's (1974) comprehensive review of experimentally derived shear strengths of filled discontinuities indicates that our results most resemble the cohesions (C≈400kPa) of clay infilling associated with schists, quartzites, and siliceous schists with higher friction values (μ≈0.6), and with montmorillonite (smectite group) clay infillings with lower friction values (μ≈0.25). Low fault friction values (μ=0.15) are attributed to the presence of smectite clays within the fault gouge along the SAF (Lockner et al., 2011), which should have a cohesive strength of ~400 kPa (Barton, 1974). Along a similar tectonic strike-slip system such as the NAF, the same factors might be contributing to a lower static friction coefficient.

The most agreed upon static friction coefficients for the extensively studied SAF based on experimental results is μ≤0.2. Our model results, constrained by recurrence intervals and slip magnitude, indicate that values for static friction that are compatible with measured values of μ≤0.2 require a cohesion of C=500 kPa (Table 3.1). For this cohesion, the static friction coefficients of μ=0.1 to μ=0.2 are considered probable while values μ<0.1 are considered potential. Carpenter et al. (2012) indicated a lower-end friction of μ=0.09 for the SAF at the fault plane. This value falls in the potential range for our results, but near the cusp between potential and probable results (Table 3.1). Numerical modeling results of fault friction for tectonic strike-slip faults extend as low as μ<0.1 (He and Chéry, 2008; Hergert and Heidbach, 2011; Provost et al., 2003) to μ<0.7 (Jolivet et al., 2013). Based on the evidence of the extensive rock experiments done to constrain fault strength parameters along the SAF, and the majority of friction values from numerical models on tectonic strike-slip faults, we suggest that the NAF has a static friction coefficient μ≤0.2. However, our results indicate that the NAF also requires a cohesion of C=500

kPA for this range of static friction coefficients. This combination of friction and cohesion are likely attributed to clay infilling as they best replicate the shear strengths determined through the numerical modeling techniques of this research.

3.7 CONCLUSION

Using a geophysical finite element model of active fault geometry along a portion of the NAF system, we were able to constrain the permissible fault strength parameters (cohesion and static friction coefficient) that matched the measured recurrence interval and slip magnitude. Matching the data required fault cohesion values of 300-500 kPa, suggesting the necessity of cohesion in geophysical models. The predicted fault strength parameters compared to experimental results indicate potential infilling materials that may be controlling the fault strength. For our study on a portion of the northern and southern strand system of the NAF around the Mudurnu valley, we were able to constrain the required cohesion to a range of C=300-700 kPa. This is that cohesion is necessary in the model to rupture the Düzce-Karadere and Mudurnu faults over documented recurrence intervals. The modeling also constrained a range of static friction coefficient for each cohesion interval, with static friction decreasing with increased cohesion. To have the maximum slip on the Izmit fault match the recorded 5 m displacement from the 1999 Izmit earthquake, permissible cohesion values were constrained to a narrower range of C=300-500 kPa. By comparing both static friction coefficient and cohesion to published estimates of cohesion from shear strength experiments (Barton, 1974) and from the most frequently documented values of static friction in literature on rock or numerical experiments on tectonic strike-slip faults, we

recommend a static friction of $\mu \leq 0.2$ with a cohesion of C=500 kPa for geophysical models of the NAF.

4.0 STRESS MODELING TO CONSTRAIN THE KINETIC FRICTION AND FAULT WEAKENING PARAMETER: AN EXAMPLE FROM THE NORTH ANATOLIAN FAULT EAST OF THE MARMARA SEA

Fault weakness can be attributed to (1) the presence of weak materials at the fault interface, or (2) dynamic fault weakening. Weak minerals would contribute to a statically weak fault, whereas dynamic fault weakening could weaken a fault that is initially statically strong. We explore dynamic fault parameters - kinetic friction coefficient (μ_k) and a slip-weakening distance (D_c) - through the use of fault stress models on a portion of the North Anatolian Fault (NAF) east of the Marmara Sea. We constrain ranges of permissible dynamic fault parameters by comparing the rupture time of faults to a record of recurrence intervals for the Düzce-Karadere (300 years) and Mudurnu (100-150 years) faults, and the total modeled slip on the Izmit fault to that following the August 1999 Izmit earthquake sequence (5 m). With initial static fault conditions (static friction coefficient (μ_s) and cohesion (C) of 0.5-0.8 and 400 - 300 kPa respectively), dynamic fault parameters of μ_s-$\mu_k \geq 0.2$ and D_c of 0 and 1 m cause the faults weaken too quickly to satisfy geologic constraints. Above cohesions of 500 kPa, weakening occurs too slowly to match geologic constraints, regardless of dynamic fault parameters. At cohesions of 400-500 kPa, with kinetic friction between 0.6 and 0.8, the faults still weaken too slowly. However, at kinetic frictions below this range, the faults weaken enough to satisfy the fault constraints. For static frictions (μ_s) of 0.6-0.8, which match laboratory experiments on the strength of rocks, a cohesion

of 300-400 kPa is required. With a 300 kPa cohesion, the value for kinetic friction should satisfy μ_s-$\mu_k \leq 0.2$ for $D_c \leq 1$ m, but the range of acceptable values grows when we consider D_c between 1 and 5 m. Based on our results, we infer that at 400 kPa kinetic friction coefficients of ≤0.4 with D_c between 1 and 5 m would satisfy the geologic constraints. However, given the computationally expensive processing of dynamic fault weakening models, we recommend using $\mu_s \leq 0.2$ and C=500 kPa for long-term stress models of the NAF, as these weaker static fault conditions also satisfy the geologic constraints.

4.1 INTRODUCTION

Data on fault surface heat flow (heat due to friction) and stress orientations around crustal-scale fault zones such as the San Andreas fault (SAF) in California (Lachenbruch and Sass, 1980; Zoback et al., 1987), and slip on low-angle normal faults (Collettini and Sibson, 2001; Sibson, 1994) indicate that they are much weaker than expected from laboratory models of friction (Holdsworth, 2004). This weakness could be separated into two classes: (1) the fault is weak all of the time due to the presence of weak minerals (Lachenbruch and Sass, 1980; Lockner et al., 2011; Moore and Rymer, 2007) or (2) it is weak only during large earthquakes due to fault weakening at high slip velocity (Boutareaud et al., 2008; Di Toro et al., 2006; Lachenbruch and Sass, 1980). The SAF is thought to be an example of such a weak fault, as it does not exhibit a frictional heat flow anomaly, and the direction of maximum principal stress (σ_1) is near-perpendicular to the fault trace (Faulkner et al., 2006; Holdsworth, 2004). The North Anatolian fault (NAF) shares many similarities with the SAF; length, age, slip rates, and geometry (Allen, 1982). However, the NAF does not exhibit near-perpendicular angles between its fault trace and

the direction of σ_1, and there are no data regarding the stress magnitude or heat flow of the NAF, particularly west of the town of Bolu in the Marmara region (Dresen et al., 2007). This raises a question regarding the strength of the NAF, and what conditions best replicate the geologic record in stress models of the NAF.

The stress magnitude required to set a fault at rest into motion is often greater than the stress required to maintain motion (Rabinowicz, 1951). In the stick-slip friction model, slip begins when the static friction (μ_s) of the fault interface is overcome (Andrews, 1976). Once slip motion commences, a fault loses strength, and this reduction of strength from static to a reduced kinetic (dynamic; μ_k) friction is the most simple constitutive relation used to describe a frictional interface in the classical "static-kinetic" friction law (Rabinowicz, 1951; Rice and Tse, 1986). The values of static and kinetic friction coefficients for fault interfaces is highly dependent on both the fault bounding materials, and the fault gouge material, which may act as a lubricant to decrease the frictional coefficients (Barton, 1974; Wyllie, 1999). Furthermore, the fault strength transition from static to kinetic values does not occur instantaneously, but rather tends to occur over a window of time (Figure 4.1) (Rabinowicz, 1951). This rate of strength reduction can be characterized by a slip-weakening distance (D_c) (Hirose and Shimamoto, 2005). To determine the slip-weakening distance, two approaches are typically used: friction experiments and seismological (numerical) studies.

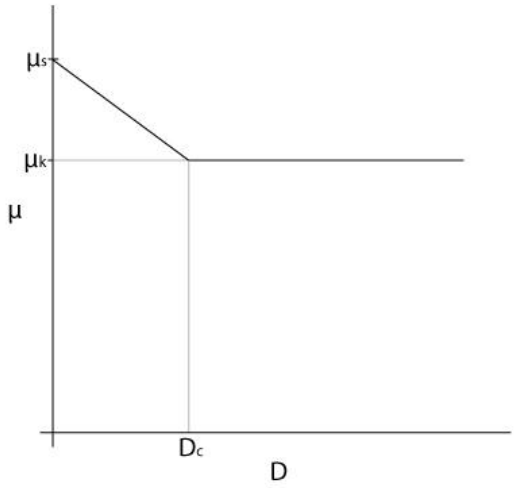

Figure 4.1 Simplified representation of the variation of coefficient of friction with distance.On the plot of friction coefficient (μ) to displacement (D), μ_s is the static friction, μ_k the kinetic friction, and D_c the slip-weakening distance.

Laboratory measured slip-weakening distances from rotary shear experiments in a high pressure apparatus have yielded D_c in the range of 10^{-5}-10^{-3} m (Dieterich, 1978; Dieterich, 1979, 1981; Hirose and Shimamoto, 2005; Marone and Kilgore, 1993; Ohnaka, 1992; Tullis and Weeks, 1986). These type of experiments measure the shear (τ) and normal stress (σ_n), whose ratio (τ/σ_n) yields friction, and compare it to the displacement along the simulated fault interface to determine D_c (Figure 4.2) (Hirose and Shimamoto, 2005). The peak friction is static friction (μ_s), and the displacement occurring until the friction settles to a lower limit (μ_k) is D_c.

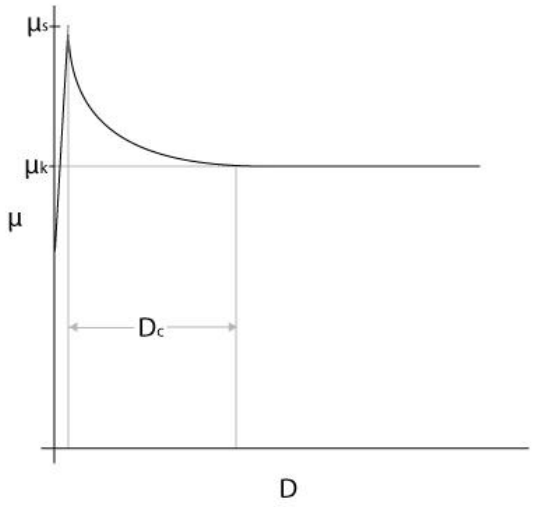

Figure 4.2 Simplified representation of a friction (μ) vs. displacement (D) curve from laboratory experiments.

Seismological, or numerical, studies determine the spatiotemporal distribution of slip on a fault plane by the inversion of data from near-field strong-motion seismograms, and determine the stress field associated with slip at various times (Fukuyama et al., 2003; Ide and Takeo, 1997; Mikumo et al., 2003). D_c is determined from the slip magnitude, slip rate, and shear stress using a constitutive slip-weakening law, and has typical values in the range of 10^{-1}-10^{0} m (Fukuyama et al., 2003; Hirose and Shimamoto, 2005; Ide and Takeo, 1997; Mikumo et al., 2003). The discrepancy between laboratory experiments and seismological studies is often attributed to the fact that rupture on natural faults is not limited to a specific contact area that exists in laboratory specimens (Scholz, 1988). In addition, continued co-seismic slip on natural faults at high velocities yields much larger values of D_c than friction experiments as a result of frictional melt lubricating the fault surface (Tsutsumi and Shimamoto, 1997).

The decrease from μ_s to μ_k over D_c can be described mathematically as in Equation 4.1:

$$T_s = C - \left(\mu_s - (\mu_s - \mu_k)\frac{D}{D_c}\right)T_n$$

Equation 4.1 Mathematical representation of the "static-kinetic" friction model.

where T_s is the shear traction, T_n is the normal traction, C is the cohesion on the fault interface, and D is the fault slip at any given time following the initiation of fault rupture. At a specific point on the fault surface immediately following the initiation of fault rupture at that location, the fault weakens gradationally from μ_s to μ_k as slip occurs (Figure 4.2). When enough slip has occurred so that the frictional force acting on the point is that of μ_k, the value of total slip is known as the slip-weakening distance. Once the total slip exceeds the slip-weakening distance, the only resisting force acting on the fault interface at that point is kinetic friction. At some critical slip-weakening distance the effect of μ_k over the entire fault interface will be negligible, because the fault weakens too slowly.

Using stress models, this paper will evaluate which estimates of dynamic fault parameters produce modeled rupture times and total slip that best match recurrence intervals - a proxy for the time it takes to build up stress from a relaxed state to fault rupture - and slip magnitudes along the NAF east of the Marmara Sea. We evaluate dynamic fault parameters for a range of static fault conditions that produce modeled rupture times and slip which match available data for the NAF (Karimi et al., in revision), as well as static fault conditions that are too strong to match fault rupture times and slip. Our goal is to explore the potential strength of the NAF, evaluate the permissible range of static fault conditions that will facilitate slip when aided by fault weakening parameters, and determine the importance of using kinetic friction and slip-weakening distance parameters on future long-term stress models of the NAF system.

4.2 GEOLOGIC BACKGROUND

The NAF is a 1200 km fault contained within a dextral shear zone (NAF system) that parallels the southern shore of the Black sea (Şengör, 1979; Şengör et al., 2005). This fault system is contained within a westward-widening late Paleozoic to early Tertiary Tethyan accretionary complex trapped between the Eurasian and Anatolian plates (Şengör, 1979; Şengör and Natal'in, 1996; Şengör et al., 2005). The relative weakness of the accretionary complex to the stronger Eurasian and Anatolian plates facilitates the decoupling of the two plates along the NAF system. The dextral shear zone continues to broaden across the northern Aegean sea into the southern and central mainland parts of Greece (the Grecian Shear Zone) (Şengör, 1979; Şengör and Natal'in, 1996), terminating at the Hellenic subduction zone (Dewey and Şengör, 1979; McKenzie and Jackson, 1983). Due to the broad nature of the shear zone west of the town of Bolu, the through-going NAF bifurcates into two main strands: a northern strand bordering the northern shores of the Marmara Sea, and a poorly-defined southern strand which trends towards the southern Marmara sea edge. (Şengör et al., 2005) (Figure 4.3 A). The eastern portion of the NAF initiated approximately 10-12 Ma, contemporaneously with the southern strand, while the northern strand formed in the Pleistocene (Şengör et al., 2005). Westward decreasing fault displacements along both the northern and southern strands of the NAF imply that total displacement in the west must be taken up by smaller faults within the greater NAF system that are not part of the through-going NAF (Hubert-Ferrari et al., 2002; Şengör and Canıtez, 1982; Şengör et al., 2005).

Our study area is an 85 km wide by 111 km long region centered on the Mudurnu Valley, where complexity of fault fragmentation along the western NAF can be seen as two strands of the NAF almost converge, and then diverge (Figure 4.3 A). Within this area, the northern strand

is comprised of the Düzce and Karadere faults (simplified as the Düzce-Karadere fault) and the Izmit fault, while the southern strand is comprised of the Mudurnu and Iznik faults (Figure 4.3 B). The strike-slip faults of the NAF within our study area are nearly vertical (Ben-Zion et al., 2003). Recurrence intervals of M_w>6.0 earthquakes for the Mudurnu fault are 100-150 years (Palyvos et al., 2007). The Düzce-Karadere fault displayed an earthquake recurrence interval of 360-560 years pre ~1 ka while the three most recent earthquakes recurred at intervals of 140-250 years (Pantosti et al., 2008). We simplify the earthquake record by utilizing a median of 300 years for this fault. The recurrence intervals are used as a proxy for the length of time required to build up the stress necessary to rupture the faults from a relaxed condition. We evaluate the range of viable values for kinetic friction and length of a slip-weakening distance along the NAF by comparing the recurrence intervals for the Mudurnu and Düzce-Karadere faults to the time it takes the modeled faults to rupture >1 m along at least 50% of their lengths (Karimi et al., in revision). In addition to recurrence interval and rupture time, we also compare maximum fault slip along the Izmit fault, which exhibited a maximum slip of 5 m following the Izmit earthquake sequence of August, 1999 (Barka, 1999). The M_w 7.4 earthquake, originating the sequence, occurred along the Izmit fault at the western boundary of our study area (Barka, 1999).

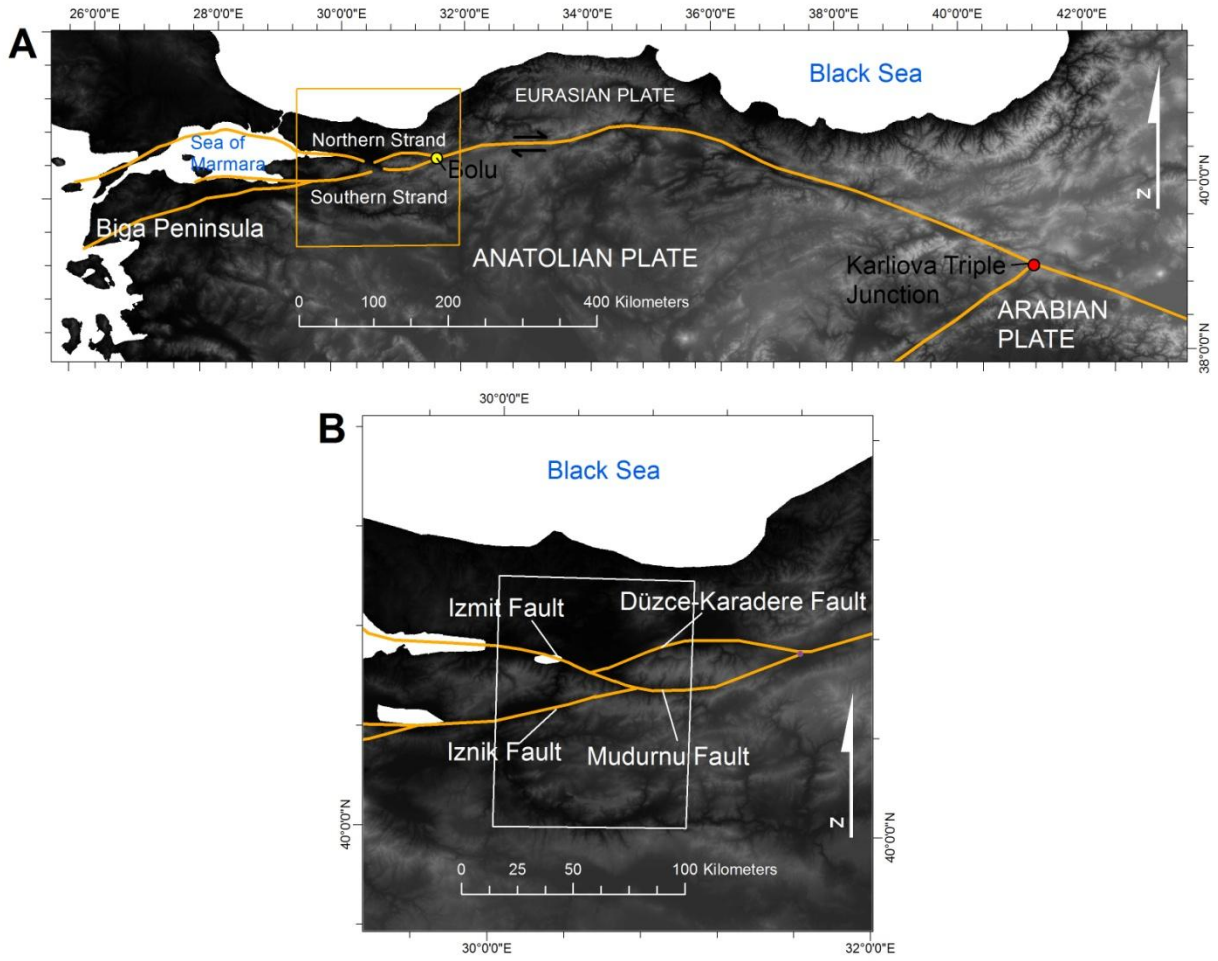

Figure 4.3 Tectonic setting of the NAF and eastern Marmara region. A) The NAF and its bifurcation into the northern and southern strands west of the town of Bolu, and B) fault names within the region of interest at the Mudurnu valley. The white box represents the modeled region of interest.

4.3 GEOPHYSICAL MODEL

We employed a 2-dimensional simplified fault model with velocity boundary conditions describing the active NAF system near the Mudurnu valley. We simplified the geometry of the northern and southern strands as boundaries which separate three distinct blocks/zones within the region of interest: the Istanbul zone north of the northern strand and part of the Eurasian tectonic

plate, the Armutlu-Almaçik zone between the two strands, and the Sakarya zone south of the southern strand (names adapted from Yılmaz et al. (1997)) (Figure 4.4). The Mudurnu portion of the southern strand and the Izmit fault are linked completely through the Mudurnu valley (Karimi et al., 2014) (Figure 4.3 B). We consider the linking feature to be a NW extension of the Mudurnu fault. In strike-slip systems, short extensional faults linking echelon fault segments allow for long-term transfer of fault slip, thus affecting the stress field distribution, and may also act as kinetic barriers impeding or arresting rupture propagation (King, 1986; King and Nábëlek, 1985; Sibson, 1986). Geophysical modeling of the linked northern and southern strands highlights both of these features (Karimi et al., in revision). The linking of the Mudurnu fault with the Izmit fault allowed for long-term transfer of fault slip, thus influencing the overall stress field orientation. In addition, the junction of the two faults momentarily arrested the progression of modeled slip from the Izmit fault before continuing down the Mudurnu Fault and completely impeded fault slip propagation to the Düzce-Karadere fault (Karimi et al., in revision).

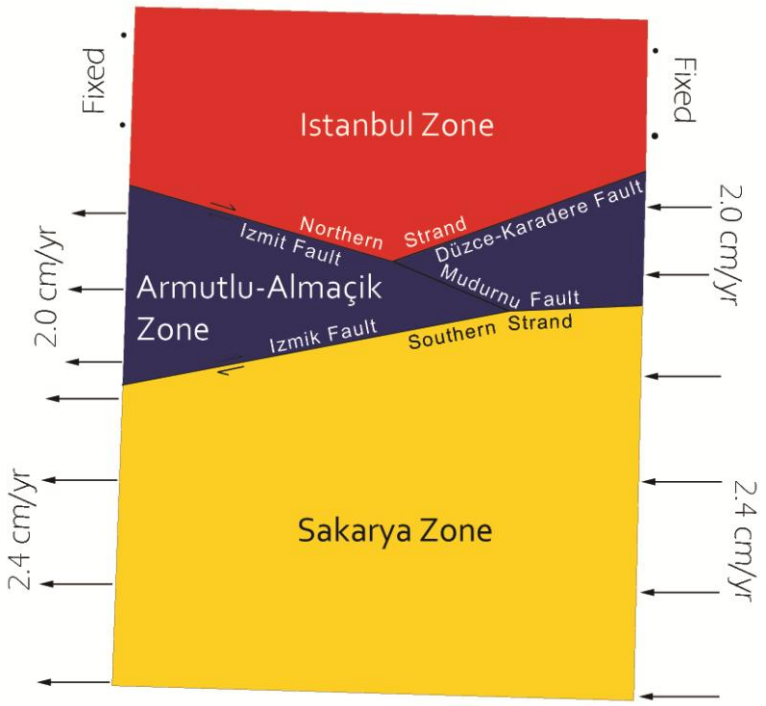

Figure 4.4 Simplified fault model. Location of the Izmit, Izmik, Düzce-Karadere, and Mudurnu faults along the northern and southern strands within the simplified fault model, as well as the velocity boundary conditions applied to the model. The Istanbul remains fixed while the two zones below are pushed and pulled westward at different rates.

Each of the three zones has distinct rock types exposed at the surface. We simplified the geology at the surface to the three basic rock types (igneous, sedimentary, and metamorphic). Average densities of the three rock types were utilized to empirically calculate rock physics parameters for each zone - specifically compressional wave velocities (V_P) and shear wave velocities (V_S). The density of each block was calculated by weighting the densities of the three rock types by their percentage of block area. The densities determined for each block were then used to extract compressional wave velocities (V_P) from the Database of Global Rock Properties by Dalhousie University/Geological Survey of Canada High Pressure Laboratory (DU/GSC,

2001). We used the V_P values for 10 MPa, as the 2-D model addresses the surface (upper 1 kilometer) geology. From these compressional velocities we evaluated the shear wave velocities (V_S) using a V_P/V_S ratio of 1.7, which is the prescribed ratio for hard (zero-porosity) rocks (Barton, 2007). The resulting densities, V_P and V_S of each region were applied to their respective blocks in the finite element model (Karimi et al., in revision; Karimi et al., 2014).

Velocity boundary conditions were determined from GPS campaigns and permanent geodetic control points to measure/monitor crustal movements in Turkey (Ozener et al., 2009). In addition, additional GPS campaigns were performed by a collaborative project of Boğaziçi University (BU), Massachusetts Institute of Technology (MIT), Turkish Scientific and Technological Research Council (TUBITAK), General Command of Mapping (GCM), and Istanbul Technical University (ITU) (Ozener et al., 2009). Information about this collaboration and the network(s) they deployed can be found in Ergintav et al. (2002). We use the horizontal GPS velocities in a Eurasia-fixed reference frame of Ozener et al. (2009). In this reference frame, the Istanbul zone is on the fixed Eurasian plate (0.0 cm/yr), the Armutlu-Almaçik zone moves westward at 2.0 cm/yr, and the Sakarya zone moves westward at 2.4 cm/yr. These rates were assigned to the model blocks to push them at their eastern boundaries and pull them at their western boundaries (Figure 4.3) (Karimi et al., in revision; Karimi et al., 2014).

4.4 METHODS

We applied a triangular mesh over the region of interest with a grid spacing of 5 km along the outer boundaries and a finer grid of 2 km near the faults. The grid spacing is used as input to create a finer triangular mesh near the faults, which grades into a coarser mesh towards the outer

boundaries. We use PyLith (Aagaard et al., 2012), to process the finite element model, using Coulomb failure criterion along the faults. The GPS determined velocities were applied to their boundaries as quasi-static dirichlet boundary conditions on the east and west bounds of the blocks. The simplified fault geometry, block boundary velocities, and associated rock physics parameters remain unchanged, while fault parameters are changed between each simulation. We explore the effects of various dynamic fault properties at three previously constrained estimates of μ_s and C: μ_s of 0.8, 0.5, and 0.2 with cohesion values of 300, 400, and 500 kPa, respectively (Karimi et al., in revision). For each static fault strength we decrease μ_k at 0.1 increments from an initial value equal to μ_s to 0.0 and test values of D_c at 0, 1, 5, 10, 20, 30, and 40 m. Additionally, we explore the effects of various dynamic fault properties for initial static conditions that ruptured too slowly to match earthquake recurrence intervals for the region (Karimi et al., in revision): μ_s of 0.8 and 0.6 at cohesions of both 500 and 700 kPa. For μ_s of 0.8, we test μ_k values of 0.8, 0.7, 0.4, and 0.0 with Dc values of 0, 1, and 5 m, and for μ_s of 0.6, we test μ_k values of 0.6, 0.5, 0.4, and 0.0, again with Dc values of 0, 1, and 5 m. Each simulation was processed for 400 years at 5 year time step intervals.

The output of each simulation were analyzed to determine at what times step the Mudurnu and Düzce-Karadere faults experienced enough stress to cause a slip >1 m along at least 50% of the modeled fault lengths. The minimum slip of 1 m is chosen to diminish the error associated with smaller values in such a large scale model. The recorded time step is assumed to be equivalent to the length of time that it would take to build up stress to rupture the fault. We further make an assumption in our model that both faults begin building up stress from a relaxed state simultaneously. The time steps were then recorded and compared to the recurrence interval for each fault, which are used as a proxy for the time between stress accumulation from a relaxed

state to rupture. Values considered "probable" for the Mudurnu fault ranged from 100-150 years, and 275-325 years for the Düzce-Karadere fault. A 25 year additional buffer beyond the upper and lower limits was considered "potential." The total slip on the Izmit fault is recorded at the timestep associated with the final rupture of either the Mudurnu, or Düzce-Karadere faults to further constrain the results by comparing them to the known maximum slip of the Izmit fault following the August 1999 Izmit earthquake sequence.

4.5 RESULTS

Karimi et al. (in revision) find that cohesion is necessary in geophysical models of the NAF, and their results matched the expected inverse trend between static friction and cohesion. Additionally, slip begins at the western end of the Izmit fault and progresses eastward until the junction of the Izmit, Düzce-Karadere, and Mudurnu faults (Karimi et al., in revision). In all simulations with cohesion >200 kPa, the leading edge of slip migrates down along the Mudurnu fault, leaving the Düzce-Karadere segment to rupture independently (Karimi et al., in revision). This is identical to the slip pattern seen in our simulations.

Results of changing dynamic parameters for initial static fault conditions, which best replicated fault rupture times and total slip - μ_s of 0.2, 0.5, and 0.8 for cohesions of 500, 400 and 300 kPa, respectively (Karimi et al., in revision), are presented in Table 4.1. Where fault rupture times agreed with the time constraints based on recurrence intervals, the total slip on the Izmit fault matched that of the geologic record. When rupture times were not met, the total slip was less than the 5 m. With μ_s=0.2 and C=500 kPa, all simulations satisfy the constraints of fault rupture time for the Mudurnu and Düzce-Karadere faults, and maximum total slip on the Izmit

fault. With μ_s=0.5 and C=400 kPa, and with μ_s=0.8 and C=300 kPa, the faults weaken quickly until a critical slip-weakening distance around 5 m is reached. This weakening leads to simulations falling outside of the rupture time constraints within 0.2 of the initial static friction for slip-weakening distances from 0 to 1 m. At Dc≥5 m all simulations satisfy the fault rupture time and slip constraints. Furthermore, above this critical slip-weakening distance, the amount of fault weakening (identified as kinetic friction) decreases as the slip-weakening distance increases, which can be seen as more simulations become "probable" (green) rather than "potential" (orange) in Table 4.1.

Table 4.1 Dynamic results for constrained static fault conditions. Timestamps (in years) of >1 m rupture along 50% the Düzce-Karadere (D-K) and Mudurnu (MV) faults for each μ_k and D_c for μ_s of 0.2, 0.5, and 0.8 for cohesions of 500, 400 and 300 kPa, respectively (Karimi et al., in revision). Green represents the probable results, while orange represents the potential results. Maximum slip on the Izmit fault is at the time the final fault ruptured.

STATIC FRIC.	0.8																				
COHESION	300 kPa																				
	SLIP WEAKENING PARAMETER (m)																				
	0			1			5			10			20			30			40		
KIN. FRIC.	Slip (m)	DK	MV	Slip (m)	DK	MV	Slip (m)	DK	MV	Slip (m)	DK	MV	Slip (m)	DK	MV	Slip (m)	DK	MV	Slip (m)	DK	MV
0.8	5	280	135	5	280	135	5	280	135	5	280	135	5	280	135	5	280	135	5	280	135
0.7	5	260	135	5	260	135	5	275	145	5	275	145	5	275	135	5	275	135	5	275	135
0.6	4	245	140	5	250	135	5	270	135	5	275	140	5	275	135	5	275	140	5	275	135
0.5	4	230	140	4	235	140	5	265	135	5	270	135	5	275	135	5	275	135	5	275	135
0.4	4	220	140	4	225	140	5	265	140	5	270	140	5	275	140	5	275	140	5	275	135
0.3	4	210	155	4	215	140	5	260	140	5	270	140	5	270	140	5	275	140	5	275	140
0.2	3	195	150	4	205	135	5	255	135	5	265	135	5	270	135	5	270	140	5	275	135
0.1	3	190	150	4	200	140	5	255	135	5	265	135	5	270	135	5	270	135	5	270	135
0	3	180	140	3	190	140	5	250	140	5	265	135	5	270	135	5	270	135	5	270	135

STATIC FRIC.	0.5																				
COHESION	400 kPa																				
	SLIP WEAKENING PARAMETER (m)																				
	0			1			5			10			20			30			40		
KIN. FRIC.	Slip (m)	DK	MV	Slip (m)	DK	MV	Slip (m)	DK	MV	Slip (m)	DK	MV	Slip (m)	DK	MV	Slip (m)	DK	MV	Slip (m)	DK	MV
0.5	5	280	135	5	280	135	5	280	135	5	280	135	5	280	135	5	280	135	5	280	135
0.4	5	270	140	5	270	140	5	280	140	5	285	135	5	285	140	5	270	135	5	285	135
0.3	5	255	140	5	255	135	5	280	135	5	280	140	5	285	135	5	285	140	5	285	135
0.2	4	240	140	4	245	135	5	275	135	5	280	140	5	285	140	5	285	135	5	285	135
0.1	4	230	135	4	235	140	5	270	140	5	275	135	5	280	140	5	280	135	5	285	135
0	4	220	140	4	230	135	5	265	140	5	275	135	5	275	135	5	280	140	5	280	135

STATIC FRIC.	0.2																				
COHESION	500 kPa																				
	SLIP WEAKENING PARAMETER (m)																				
	0			1			5			10			20			30			40		
KIN. FRIC.	Slip (m)	DK	MV	Slip (m)	DK	MV	Slip (m)	DK	MV	Slip (m)	DK	MV	Slip (m)	DK	MV	Slip (m)	DK	MV	Slip (m)	DK	MV
0.2	5	290	140	5	290	140	5	290	140	5	290	140	5	290	140	5	290	140	5	290	140
0.1	5	275	135	5	275	135	5	280	140	5	280	140	5	285	140	5	285	135	5	285	140
0	5	260	135	5	260	135	5	275	130	5	280	140	5	285	140	5	285	135	5	285	140

The results of increased initial static conditions to where rupture times exceeded the fault earthquake recurrence interval (μ_s of 0.8 and 0.6 with cohesions of 500 and 700 kPa) (Karimi et al., in revision), are shown in Tables 4.2 and 4.3. For initial static conditions where μ_s=0.8 and C=500 kPa, fault rupture times are met as either "probable" (green), or "potential" (orange) for

lower values of kinetic friction (0 and 0.4) and for Dc values of 0 or 1 m. As the slip-weakening parameter increases, the range of permissible values for kinetic friction decreases, matching the expected trend from Equation 4.1. This same trend is seen when μ_s=0.6 and C=500 kPa, where more simulations match the rupture time constraints at higher values of μ_k (up to 0.5). The critical slip-weakening distance identified for both sets of initial static fault conditions is less than or equal to 5 m when static friction is 0.8, and may be greater than 5 m when the static friction is 0.6 (Table 4.2). In the results of both static friction values, the total slip on the Izmit fault exceeds the 5 m maximum measured for the August 1999 Izmit earthquake sequence. At very low kinetic frictions coefficients, the minimum total slip recorded for the Izmit fault is 6 m at slip-weakening distances of 0 and 1 m.

Table 4.2 Dynamic results at cohesions of 500 kPa. Timestamps (in years) of >1 m rupture along 50% the Düzce-Karadere (D-K) and Mudurnu (MV) faults for each μ_k and D_c for μ_s of 0.8 and 0.6 with a cohesion of 500 kPa. Green represents the probable results, while orange represents the potential results. Maximum slip on the Izmit fault is at the time the final fault ruptured.

STATIC FRIC.	0.8								
COHESION	500 kPa								
	SLIP WEAKENING PARAMETER (m)								
	0			1			5		
KIN. FRIC.	Slip (m)	DK	MV	Slip (m)	DK	MV	Slip (m)	DK	MV
0.8	9	400	135	9	400	135	9	400	135
0.7	8	380	140	8	385	140	8	395	135
0.4	7	320	135	7	330	140	8	385	135
0	6	265	135	6	285	135	8	365	135

STATIC FRIC.	0.6								
COHESION	500 kPa								
	SLIP WEAKENING PARAMETER (m)								
	0			1			5		
KIN. FRIC.	Slip (m)	DK	MV	Slip (m)	DK	MV	Slip (m)	DK	MV
0.6	8	360	135	8	360	135	8	360	135
0.5	7	335	135	7	340	140	8	355	135
0.4	7	315	135	7	325	140	8	345	135
0	6	265	135	6	280	140	7	330	135

Table 4.3 depicts the results of changing dynamic fault conditions for the strongest modeled static fault conditions, μ_s of 0.8 and 0.6, both with a cohesion of 700 kPa (Karimi et al., in revision). When initial static conditions of μ_s=0.8 and C=700 kPa are applied to the simulations, rupture times never satisfy the fault constraints; however, some weakening does occur at very low kinetic friction coefficients associated with D_c of 0 and 1 m. At a D_c of 5 m for both static fault conditions, the fault does not weaken at all; thus the critical slip-weakening distance is less than or equal to 1 m. With initial static conditions of μ_s=0.6 and C=700 kPa, only the simulation with kinetic friction and slip-weakening distance of zero weakens enough to be

evaluated as "potential." In the results of both static frictions, the total slip on the Izmit fault exceeds and never nears the 5 m maximum measured for the August 1999 Izmit earthquake sequence.

Table 4.3 Dynamic results at cohesions of 700 kPa. Timestamps (in years) of >1 m rupture along 50% the Düzce-Karadere (D-K) and Mudurnu (MV) faults for each μ_k and D_c for μ_s of 0.8 and 0.6 with a cohesion of 700 kPa. Green represents the probable results, while orange represents the potential results. Maximum slip on the Izmit fault is at the time the final fault ruptured.

STATIC FRIC.	0.8								
COHESION	700 kPa								
	SLIP WEAKENING PARAMETER (m)								
	0			1			5		
KIN. FRIC.	Slip (m)	DK	MV	Slip (m)	DK	MV	Slip (m)	DK	MV
0.8	9	>400	135	9	>400	135	9	>400	135
0.7	9	>400	130	9	>400	135	9	>400	135
0.4	9	>400	135	9	>400	140	9	>400	135
0	8	355	135	8	365	140	9	>400	140

STATIC FRIC.	0.6								
COHESION	700 kPa								
	SLIP WEAKENING PARAMETER (m)								
	0			1			5		
KIN. FRIC.	Slip (m)	DK	MV	Slip (m)	DK	MV	Slip (m)	DK	MV
0.6	9	>400	135	9	>400	135	9	>400	135
0.5	9	>400	130	9	>400	135	9	>400	140
0.4	9	>400	135	9	>400	135	9	>400	135
0	8	350	135	8	360	135	9	>400	135

4.6 DISCUSSION

Based on Equation 4.1, at a given static friction, cohesion, shear stress and normal stress, the relationship between μ_k and D_c should be inverse. When $\mu_{k=}\mu_s$, there should be no variation in the

simulation results regardless of the D_c value. Because this expected trend between μ_k and D_c is seen in our results, as is the constancy of results when $\mu_{k=}\mu_s$, the trends in our results are not due to random error, but rather are the expected product of the assigned Coloumb failure criterion.

The fact that the NAF does not exhibit the high angle of maximum principal stress to the fault trace like the SAF (Faulkner et al., 2006; Holdsworth, 2004) does not preclude it from being a weak fault, as there are no data regarding the stress magnitude or heat flow along the NAF in the Marmara region. Should the NAF be weak, the mechanism behind it could be due to (1) the presence of weak minerals contributing to a statically weak fault (Lachenbruch and Sass, 1980; Lockner et al., 2011; Tembe et al., 2006), or (2) weakening during large earthquakes due to high-slip velocity (Boutareaud et al., 2008; Di Toro et al., 2006; Lachenbruch and Sass, 1980).

4.6.1 Statically weak NAF

Karimi et al. (in revision) constrain ranges of static friction and cohesion by comparing model rupture times to fault recurrence intervals for the Mudurnu and Düzce-Karadere faults, and maximum slip on the Izmit fault to the known slip resulting from the 1999 Izmit earthquake sequence. They find that static friction coefficients ≤ 0.85 can be used to satisfy the fault constraints if paired with the appropriate cohesion (Karimi et al., in revision): high static friction of 0.65-0.85 requires a cohesion of 300 kPa, static friction from 0.25-0.55 requires a cohesion of 400 kPa, and weak static friction of 0.0-0.2 requires a cohesion of 500 kPa (Karimi et al., in revision). Barton's (1974) comprehensive review of experimentally derived shear strengths of filled discontinuities found clay infilling to have a cohesion $C \approx 400$kPa. This clay infilling is associated with schists, quartzites, and siliceous schists with higher friction values ($\mu \approx 0.6$), and with montmorillonite (smectite group) clay infillings with lower friction values ($\mu \approx 0.25$) (Barton,

1974). It is believed that this clay infilling - weaker than the fault blocks - helps explain tectonic faults as "weak" (Moore and Rymer, 2007). For the SAF, which shares many similarities with the NAF (Allen, 1982), low fault friction values (μ=0.15) are attributed to the presence of smectite clays within the fault gouge (Lockner et al., 2011). By comparing their ranges of static friction and cohesion to the strength of weak fault gouge material for other faults, Karimi et al. (in revision) suggest that if the NAF is weak, the static fault conditions for the NAF could be μ_s=0.2 and C=500 kPa.

4.6.2 Dynamic fault weakening

With a constant cohesion (Tables 4.2 and 4.3), we can evaluate the impact of increasing static friction on the slip-weakening distance. In both Tables 4.2 and 4.3, which evaluate simulations with initial static frictions of 0.6 and 0.8, the range of slip-weakening distances that satisfy the geologic constraints decrease with increasing static friction. By comparing the results of simulations at an initial static friction of 0.8 in Tables 4.1, 4.2, and 4.3, we can evaluate the impact of cohesion on the range of permissible slip-weakening distances, which decreases as cohesion increases.

Fault weakening occurs as μ_s evolves to μ_k over the range of slip defined by D_c. The critical slip-weakening distance is a value of D_c, above which, μ_k for the entire fault interface is negligible because the fault weakens too slowly. The results of the dynamic fault simulations, with estimates of initial static conditions constrained by Karimi et al. (in revision), indicate critical slip weakening distances of greater than or equal to 5 m (Table 4.1) are necessary to satisfy the geologic constraints. Slip weakening distances that are less than 5 m allow the fault to weaken too quickly to satisfy earthquake recurrence intervals. With initial static conditions of

μ_s=0.8 and C=500 kPa (Table 4.2) and μ_s=0.8 and C=700 kPa (Table 4.3), the critical slip-weakening distance must be less than or equal to 5 m for the faults to weaken fast enough to satisfy the geologic constraints. With the initial static conditions of μ_s=0.6 and C=500 kPa (Table 4.2), the critical slip-weakening distance can be greater than 5 m, as is seen by the range of permissible results at low kinetic friction values. When cohesion is 700 kPa (Table 4.3), the critical slip-weakening distance may only be less than 1 m.

For estimates of initial static fault conditions constrained by Karimi et al. (in revision), increasing values of μ_k allow for modeled fault rupture time and slip constraints to match geologic constraints at low slip-weakening distances ($\leq$5m) by allowing fault weakening to occur more slowly (Table 4.1). Above this critical slip-weakening distance, all kinetic friction value simulations satisfy the geologic constraints, because fault weakening occurs much more slowly (Table 4.1). While all simulations satisfy the geologic constraints, as D_c increases, the range of "probable" (green) values increases to encompass a greater range of μ_k (Table 4.1). Above the critical slip-weakening distance, the effects of varying μ_k on the fault rupture times and total slip is negligible because fault weakening occurs too slowly. This slow weakening is similarly seen for simulations with initially strong static conditions that caused fault rupture to occur too slowly to match the geologic constraints (Tables 4.2 and 4.3).

4.6.2.1 Dynamically weak NAF

Laboratory experiments on the strength of rocks by Byerlee (1978) indicated that the static friction of rocks is generally between 0.6 and 0.8. At these high static frictions, the NAF would need to be weakened by some mechanism other than the presence of a statically weak material on the fault interface to match earthquake recurrence intervals and measured fault rupture slip distances. Dynamic weakening (Lachenbruch and Sass, 1980), identified in high

speed laboratory friction experiments that show friction decreasing above a threshold slip rate (Boutareaud et al., 2008; Collettini et al., 2009; Di Toro et al., 2006; Wibberley and Shimamoto, 2005), is a viable mechanism to weaken a fault and match laboratory static friction measurements. Our results indicate that in simulations with a high static friction (0.8) and cohesion (700 kPa) there are no viable dynamic weakening parameters that satisfy the geologic constraints of the region (Table 4.3). When static friction is decreased to the lower limit (0.6) proposed by Byerlee (1978), the simulations only satisfy the geologic constraints at a slip-weakening distance of 0 m, paired with a kinetic friction of 0.0. When cohesion is decreased to 500 kPa for static frictions of 0.8 and 0.6, dynamic weakening can produce permissible results (Table 4.2). The permissible values of kinetic friction for an initial static friction of 0.8 occur below 0.7 for a D_c of 0 m, and continue to decrease as the slip-weakening distance is increased. At an initial static friction of 0.6, permissible values of kinetic friction occur at 0.5 for both 0 and 1 m of slip-weakening distance, and decrease as D_c increases. While strong (0.6-0.8) static friction and moderate-strong cohesion values of 500 kPa match the recurrence interval for earthquakes along the NAF, the total slip predicted for the Izmit portion of the fault (≥6 m) does not match the 5 m maximum slip determined from the 1999 Izmit earthquake sequence. At low kinetic friction coefficients (≤0.2) the total slip predicted for the Izmit portion is 6 m, the closest value to the expected 5 m (Table 4.2). As cohesion increases, the range of kinetic friction coefficients that satisfy the fault rupture time constraints shifts down to accommodate lower μ_k (Tables 4.1 and 4.2). Since a cohesion of 300 kPa at high static frictions resulted in total slips ≤5 m, and the total modeled slip at 500 kPa was ≥6 m, we infer that the modeled fault slip on the Izmit fault will reach 5 m and satisfy the fault rupture time constraints at a cohesion of 400 kPa. This would occur at kinetic friction coefficients ≤0.4 with D_c between 1 and 5 m.

4.7 CONCLUSION

While the similarities between the NAF and SAF are numerous, we cannot assume that weak fault interface materials are present for the NAF, as postulated by Karimi et al. (in revision), to allow for a low static friction (≤0.2) with moderate cohesion (500 kPa). An alternative mechanism that results in a weak fault, is dynamic fault weakening. Using the geologic constrains of recurrence interval as a proxy for the time it takes stress to build up from a relaxed state to rupture the Düzce-Karadere and Mudurnu faults, and the total slip on the Izmit fault following its 1999 earthquake sequence, we were able to constrain estimates of permissible dynamic fault weakening properties for the NAF. For static frictions of 0.6-0.8 with a 300 kPa cohesion, the value for kinetic friction should satisfy μ_s-$\mu_k \leq 0.2$ for slip-weakening distances less than or equal to 1 m, but the range of acceptable values should grow when we consider D_c between 1 and 5 m. At 400 kPa we infer that kinetic friction coefficients of ≤0.4 with D_c between 1 and 5 m satisfy the geologic constraints. For lower static frictions, a wider range of slip-weakening distances and kinetic frictions are permissible, but would require some component of weak fault interface materials to lower the static friction below the classic Byerlee (1978) experiments. Without some sort of fault zone project on the NAF - similar to that of the San Andreas Fault Observatory at Depth (SAFOD) pilot hole project - a complete understanding of the mechanism(s) driving the weakness of the NAF will remain unknown. However, the question regarding the necessity of kinetic friction and a fault weakening parameter on future stress models of the NAF system can be addressed. We can match the geologic parameters of earthquake recurrence intervals and slip magnitude with either a statically strong fault with low kinetic friction coefficients and slip-weakening distances, or a statically weak fault ($\mu_s \leq 0.2$, C=500 kPa) with no kinetic fault weakening parameters associated with clay infilling material

(smectite). Coupling this result with the computationally expensive processing of dynamic fault models, there is no need to require dynamic fault properties in future long-term stress models of the NAF system.

5.0 DETERMINING THE THROUGH-GOING ACTIVE FAULT GEOMETRY OF THE WESTERN NORTH ANATOLIAN FAULT THROUGH STRESS MODELING

The North Anatolian Fault (NAF) is a 1200 km long dextral strike-slip fault which is part of an east-west trending dextral shear zone (NAF system) between the Anatolian and Eurasian plates. The North Anatolian shear zone widens to the west, complicating potential earthquake rupture paths and highlighting the importance of understanding the geometry of active fault systems. In the central portion of the NAF system - just west of the town of Bolu - the NAF bifurcates into the northern and southern strands, which converge, then diverge to border the Marmara Sea. At their convergence east of the Marmara Sea, these two faults are linked through the Mudurnu Valley. The westward continuation of these two fault traces is marked by further complexities in potential active fault geometry, particularly in the Marmara Sea for the northern strand, and towards the Biga Peninsula for the southern strand. We evaluate potential active fault geometries for both strands of the NAF by comparing stress models of various fault geometries in these regions to a record of focal mechanisms and inferred paleostress from a lineament analysis. For the Marmara region, two of the three possible geometries matched the maximum horizontal stress determined from a record of focal mechanisms. Of these two geometries, one represented the northern and southern side walls associated with the principal zone of deformation of the developing Marmara basin, leading us to suggest that it is the most likely representation of the active through-going fault geometry in the region. In the Biga Peninsula region, the active

geometry of the southern strand has the southern component approaching and intersecting the northern component through a linking feature in a narrow topographic valley. This geometry was selected over the other two as it overlaps the maximum horizontal stresses determined from focal mechanism data and a lineament analysis. Additionally, this geometry does not develop a prominent mis-oriented northeast-southwest stress feature observed in the stress model results of the other two geometries, and otherwise absent in the focal mechanism data or inferred from a lineament analysis.

5.1 INTRODUCTION

The North Anatolian Fault (NAF) system in Turkey has seen several devastating high magnitude earthquakes, particularly east of, and along, the northern boundary of the Marmara Sea (Bohnhoff et al., 2013; Parsons, 2004). The NAF shares many similarities with the San Andreas Fault (SAF), such as age, slip rate, geometry, and length; however, the NAF produces more high-magnitude earthquakes (M>5) than the SAF (Allen, 1982). This increased seismicity poses a significant risk to the densely populated and highly industrialized Marmara region. The 1999 earthquake sequence of August 17th, located in the eastern Marmara region near the city of Koçaeli, was initiated by a M7.4 earthquake (Stein et al., 1997) - one of the largest recorded earthquakes in Turkey by modern digital networks (Özalaybey et al., 2002) - with a devastating death toll of over 17,000 people (Scawthorn and Johnson, 2000). This event initiated numerous new research activities in the Marmara region to understand the structure and kinematics of the NAF with a broader goal of assessing the seismic hazard along the NAF (Armijo et al., 2002;

Ates et al., 2003; Hergert and Heidbach, 2010, 2011; Hergert et al., 2011; Hubert-Ferrari et al., 2000; Le Pichon et al., 2003; Le Pichon et al., 2001; Okay et al., 2000; Parsons, 2004).

One of the ways to understand the structure, or geometry, of faults such as the NAF is through stress modeling, because stress and strain fields are heavily influenced by the active fault geometry (Bilham and King, 1989; Lesne et al., 1998). Fault geometry, however, is sometimes hard to observe as a trace on the surface when little to no topographic expression is present, or if the fault has been covered by young sediments. In the region impacted by the 1999 earthquake sequence, the through-going NAF splits into two strands just west of the town of Bolu (Barka et al., 2002; Hergert and Heidbach, 2010; Şengör et al., 2005): a northern strand and southern strand that converge at the Mudurnu Valley, then diverge to bound the northern and southern shores of the Marmara Sea (Figure 5.1 A). Karimi et al. (2014) determined that there are two possible active fault geometries: (1) the two strands converge and then diverge as distinct fault traces, or (2) that the two strands are linked through the Mudurnu Valley (Figure 5.1 B). By developing stress models for both geometries and comparing them to a record of focal mechanism data and the maximum horizontal paleostress orientation as inferred from a lineament analysis of satellite imagery, Karimi et al. (2014) were able to confirm that the two strands are linked through the Mudurnu Valley.

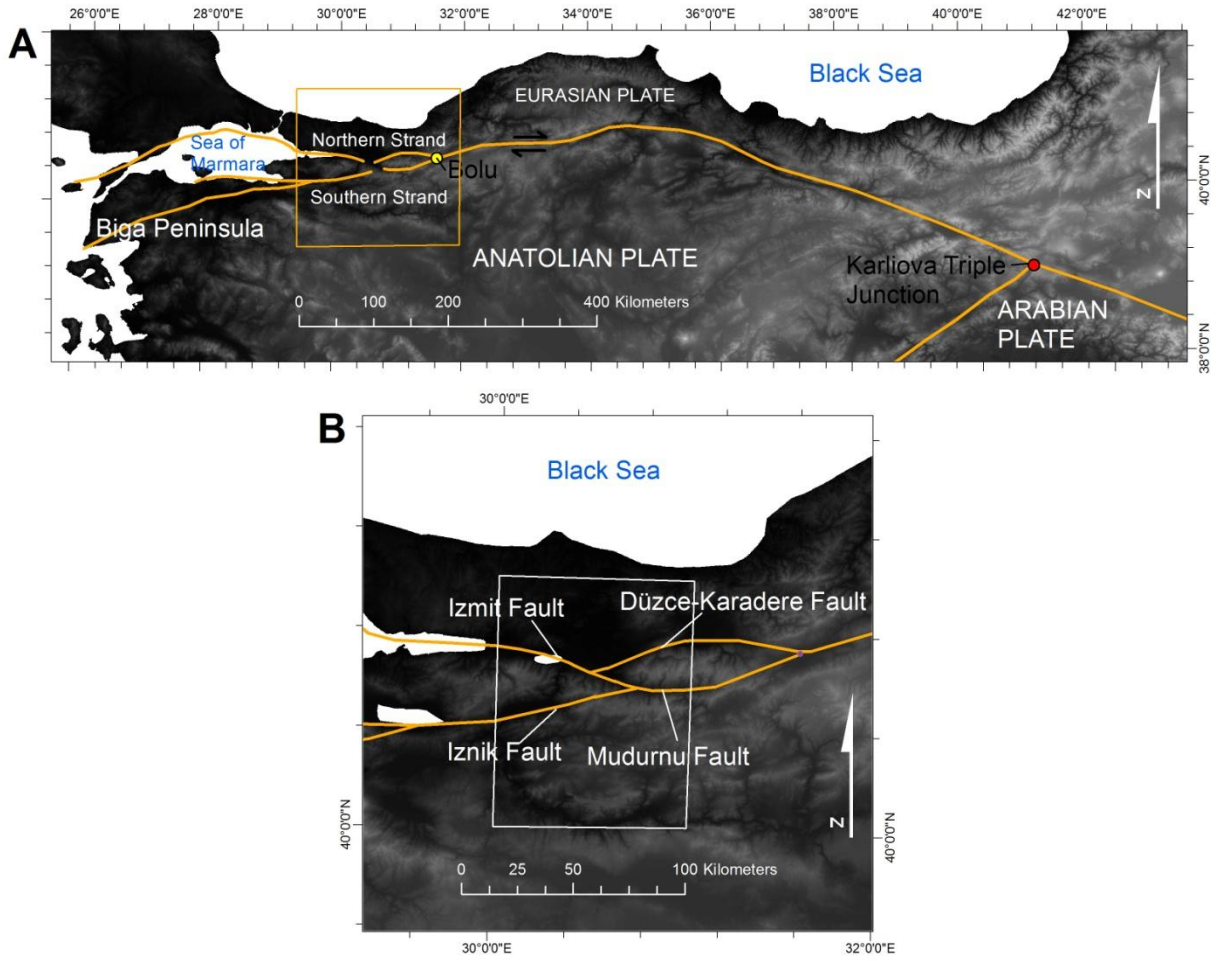

Figure 5.1 Tectonic setting of the NAF and eastern Marmara region. A) The NAF and its bifurcation into the northern and southern strands west of the town of Bolu, and B) fault names within the region of interest at the Mudurnu Valley. The white box represents the region modeled by Karimi et al. (2014).

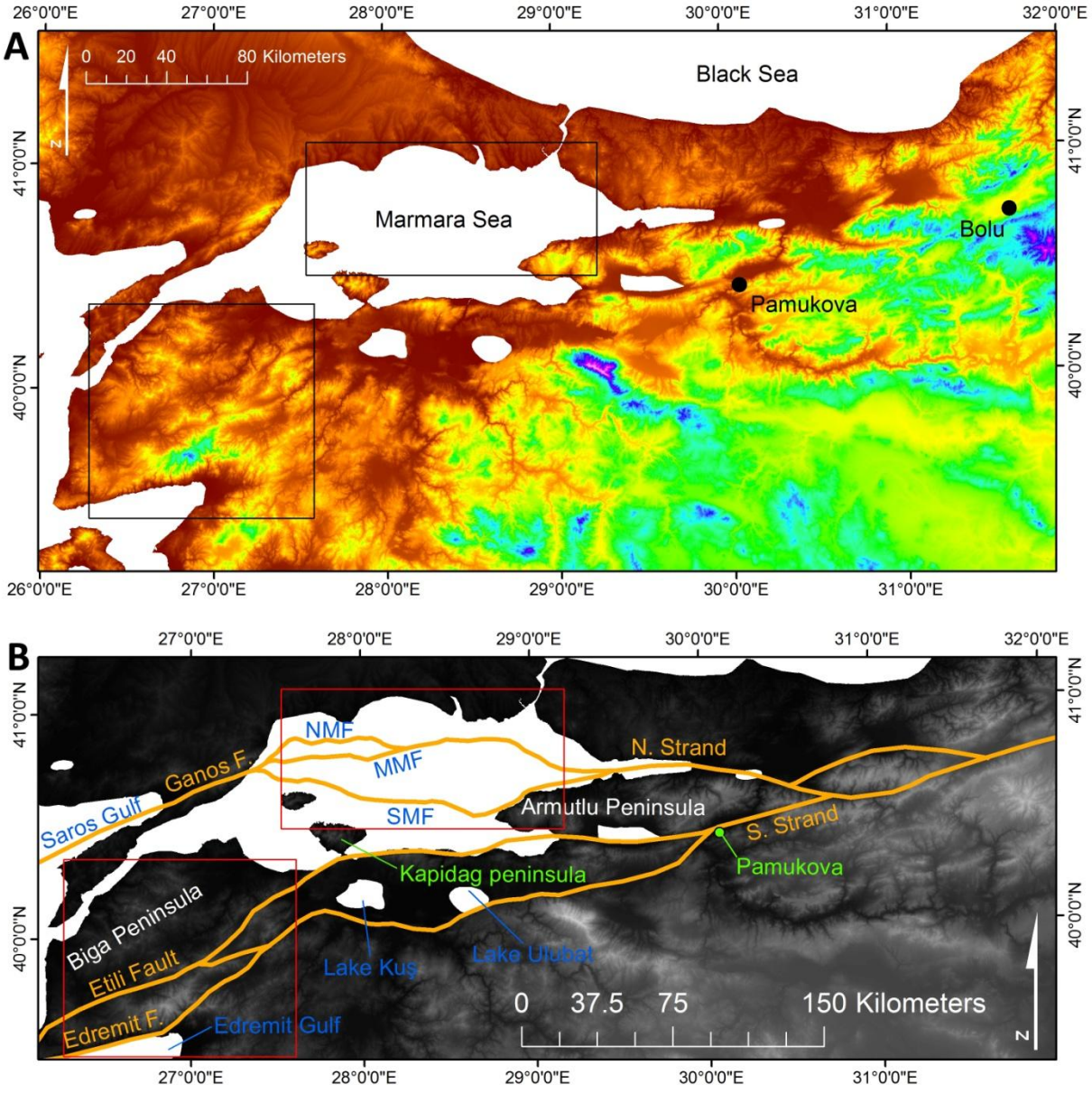

Figure 5.2 Topography and complexity of the northern and southern strands in the Marmara and Biga Peninsula region. A) Topographic data highlighting the trace of the NAF as narrow river valleys and rapid transition from high to low topography. B) complexity of all possible fault geometries in the western NAF. NMF is North Marmara Fault, MMF is Main Marmara Fault, and SMF is Southern Marmara Fault. The regions bound in red are the Marmara region (in the north) and the Biga Peninsula region (in the south).

West of the region studied by Karimi et al. (2014), the two strands roughly parallel the northern and southern coasts of the Marmara Sea; however, several complexities arise for both strands, with various active fault geometries proposed for the northern strand in the Marmara region and for the southern strand in the Biga Peninsula region. Where there is topographic data available, faults are most often expressed as narrow river valleys or the rapid transition from high to low topography (Figure 5.2 A). In the Marmara region, the northern strand bifurcates again within the gulf of Izmit (Figure 5.2 B). The southernmost trace parallels the northern Armutlu Peninsula then extends west-northwest across the Marmara Sea as the Southern Marmara Fault (SMF) (Aksu et al., 2000; Armijo et al., 2002; Barka and Kadinsky-Cade, 1988; Hergert and Heidbach, 2010, 2011; Hergert et al., 2011; Şengör et al., 2014; Straub et al., 1997). In one scenario, the northernmost trace continues to parallel the northern shore of the Marmara Sea as the Main Marmara Fault (MMF) (Flerit et al., 2003; Hergert and Heidbach, 2010, 2011; Hergert et al., 2011; Le Pichon et al., 2001; Şengör et al., 2014). Another possible active fault geometry for the northern trace could be the MMF until its intersection with the Northern Marmara Fault (NMF), where it continues only as the NMF (Aksu et al., 2000). Lastly, the MMF and NMF traces could both be part of the active fault geometry (Armijo et al., 2002). These various faults would intersect just off the coast of the western Marmara Sea, and continue across to the Saros Gulf as the Ganos Fault (Figure 5.2 B) (Aksu et al., 2000; Armijo et al., 1999; Armijo et al., 2002; Flerit et al., 2003; Hergert and Heidbach, 2010, 2011; Hergert et al., 2011; Le Pichon et al., 2014; Le Pichon et al., 2001; Şengör et al., 2005; Türkecan and Yurtsever, 2002).

Part of the complication of the southern strand begins where it bifurcates at the town of Pamukova east of the Marmara sea, but it becomes more complicated in the Biga Peninsula region (Figure 5.2 B). The northernmost trace follows the southern coast of the Marmara sea

until the Kapidag Peninsula where it trends southwest through the Biga Peninsula as the Etili Fault (Akşay et al., 2002; Flerit et al., 2003; Konak, 2002; Le Pichon et al., 2014; Şengör et al., 2005; Türkecan and Yurtsever, 2002). The southernmost trace parallels the northern trace, along the southern shores of Lakes Kuş and Ulubat (Akşay et al., 2002; Barka and Kadinsky-Cade, 1988; Boztepe-Güney et al., 2001; Konak, 2002; Şengör and Canıtez, 1982; Şengör et al., 2014; Straub et al., 1997; Türkecan and Yurtsever, 2002; Yılmaz and Karacık, 2001), then trends southwest as the Edremit fault. In the southwestern region of the Biga Peninsula, Le Pichon et al. (2014) and Şengör et al. (2005) show a potential step-over (linking feature) from the southern Edremit fault towards the Etili fault. In one possible geometry, the southern trace could terminate at the intersection, with the active fault geometry following the trace of the linking fault to continue slip along the northern trace (Konak, 2002). In a second geometry, the linking structure is absent, and the southern trace continues until it reaches the Edremit Gulf and follows the southern coastline of the Biga Peninsula (Barka and Kadinsky-Cade, 1988; Boztepe-Güney et al., 2001; Konak, 2002; Şengör and Canıtez, 1982; Straub et al., 1997; Türkecan and Yurtsever, 2002; Yılmaz and Karacık, 2001). The third potential geometry would have all faults as part of the active fault geometry in the Biga Peninsula region (Konak, 2002; Şengör et al., 2005; Türkecan and Yurtsever, 2002).

The variety of potential active fault geometry in the Marmara and Biga Peninsula region must be understood, as the active fault geometry is vital in determining areas of greatest seismic risk along the NAF system. We develop finite element models (FEM) for these two regions. This approach allows for greater resolution in the regions of interests and decreases the computational time that would be associated with modeling the entire western NAF. Using the methodology of Karimi et al. (2014), we examine the relationship between fault geometry and

the numerically determined stress fields for the regions by comparing stress outputs to a record of focal mechanisms and the maximum horizontal paleostress orientation as inferred from a lineament analysis (where topographic data is available). Based on our results, we suggest a geometry for the through-going active faults of the western NAF system.

5.2 GEOLOGIC SETTING

The 1200 km NAF is the most prominent part of a dextral shear zone (NAF system) paralleling the southern shore of the Black Sea (Şengör, 1979; Şengör et al., 2005). The NAF system is contained within a westward-widening late Paleozoic to early Tertiary Tethyan accretionary complex trapped between the Eurasian and Anatolian plates (Şengör, 1979; Şengör and Natal'in, 1996; Şengör et al., 2005). The relative weakness of the accretionary complex to the stronger Eurasian and Anatolian plates facilitates the decoupling of the two plates along the NAF system. The shear zone continues to broaden across the northern Aegean sea into the southern and central mainland parts of Greece (the Grecian Shear Zone) (Şengör, 1979; Şengör and Natal'in, 1996), terminating at the Hellenic subduction zone (Dewey and Şengör, 1979; McKenzie and Jackson, 1983). Due to the broad nature of the shear zone west of the town of Bolu, the through-going NAF bifurcates into two main strands: a northern strand roughly bordering the northern shores of the Marmara Sea, and a poorly-defined southern strand which trends towards the southern Marmara sea edge. (Şengör et al., 2005) (Figure 5.1 A). The eastern through-going NAF structure initiated approximately 10-12 Ma, contemporaneously with the southern strand, while the northern strand formed much later in the Pleistocene (Şengör et al., 2005). Decreasing fault displacements westward along the northern and southern strands of the NAF imply that total

displacement in the west must be taken up by smaller faults within the greater NAF system that are not part of the more prominent through-going NAF (Hubert-Ferrari et al., 2002; Şengör and Canıtez, 1982; Şengör et al., 2005).

5.2.1 Faulting in the Marmara region

As the northern strand enters the Marmara Sea through the Izmit Gulf, it bifurcates into two main traces: the SMF and the MMF, the latter of which intersects the NMF further west (Figure 5.3 A). A compiled record of earthquakes from a 100-year record (KOERI-UDIM, 2012), the World Seismic Map (WSM) (Heidbach et al., 2008), and the International Seismological Centre (ISC) (International Seismological Centre, 2011) (Figure 5.3 A) depict limited seismicity in the region. The MMF seems to be the most seismically active across its entire trace, with minor amounts of seismic activity around the NMF; however, the SMF seems to be only active in its eastern and western portions. The lack of seismicity was noted by Le Pichon et al. (2014), who through the use of seismic reflection profiles and drill holes penetrating the sedimentary cover down to the Upper Cretaceous basement, argue that the central portion of the SMF has been inactive for the last 3.5 Ma. Additionally, Armijo et al. (2002) do not include the SMF in their kinematic model of the modern Marmara Sea, arguing that the presence of the SMF distorts the velocity field of their model relative to the GPS velocity field. Yet, the importance of the SMF hinges heavily on the tectonic interpretation of the Marmara Sea, which is suggested to be an unconventional negative flower structure, rather than a pull-apart (Aksu et al., 2000). In the classical pull-apart basin, the negative flower structure is oblique to the strike of the buried master fault (buried northern strand of the NAF), but in an unconventional negative flower basin, the symmetry of the basin is in-line with the buried master fault (Aksu et al., 2000). As a result, Aksu et al. (2000)

argue that the SMF plays a significant role as the southern boundary of the principal deformation zone in the Marmara Sea.

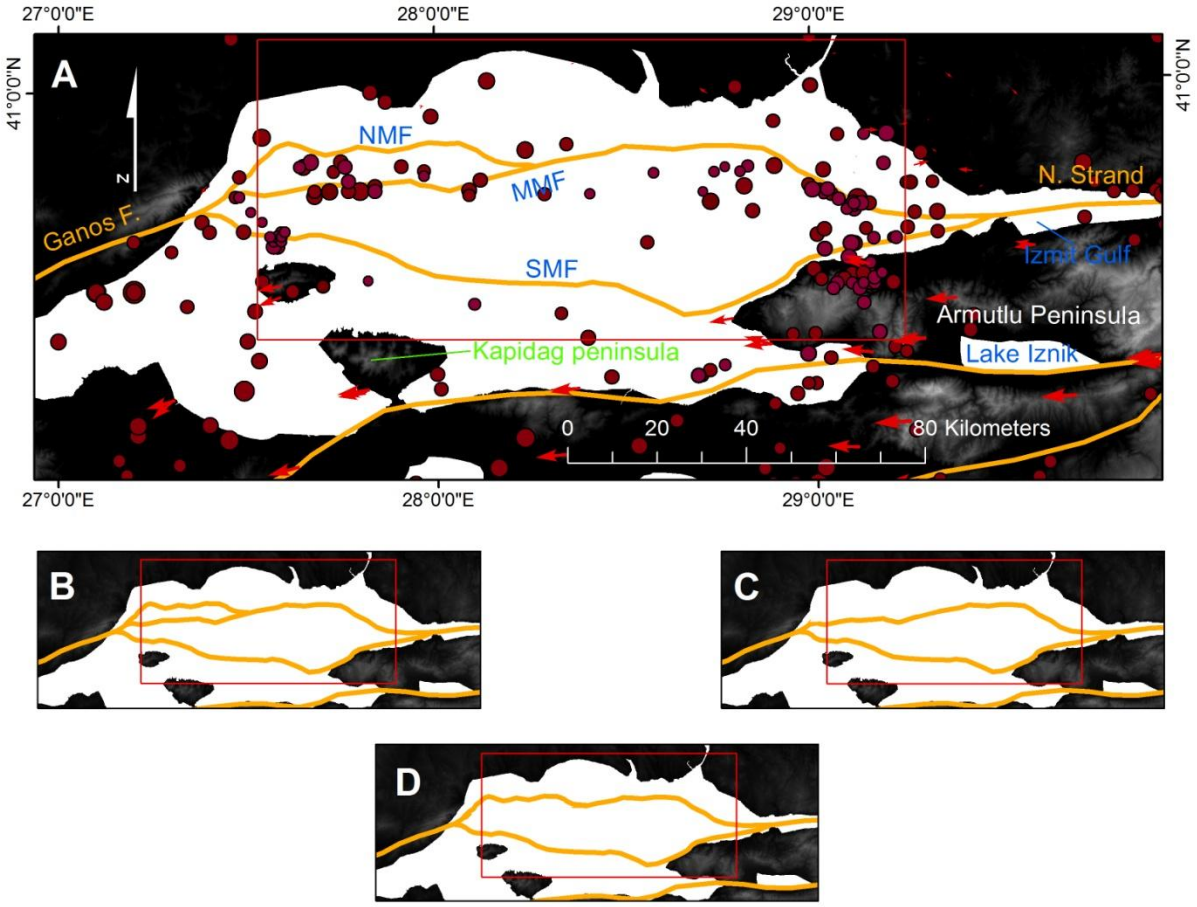

Figure 5.3 Marmara region possible faults, seismicity, and GPS velocities. A) Possible faulting in the Marmara Sea with GPS vectors as red arrows (Aktug et al., 2009; Ozener et al., 2009) and the location of compiled earthquake data sized by magnitude (maroon points) from a 100-year record of earthquakes (KOERI-UDIM, 2012), the WSM (Heidbach et al., 2008), and the ISC (International Seismological Centre, 2011). B-D) The three possible through-going active fault geometries. The red boxes represent the modeled region.

Using these arguments for active strands of the Marmara Sea faults, three possible through-going active fault geometries are possible. In the first geometry, the SMF, MMF, and

SMF are all part of the through-going active fault geometry of the northern strand (Figure 5.3 B) (Marmara 1). To develop a 3-D model that is consistent with kinematic observations, and stress data, Hergert et al. (2011) use recent images of the fault system beneath the Marmara Sea as initial input of a model with faults as frictional surfaces with varying strike and dip. The MMF, SMF, and NMF are all present as prominent features in their model which matched GPS velocities, fault slip rates, and an observed pattern of subsidence and uplift (Hergert et al., 2011). The same geometry, modeled to predict the stress field within the Marmara Sea, matched motion observations from focal mechanism solutions, the orientation of maximum horizontal stress, and the distribution of seismicity in the Marmara Sea (Hergert and Heidbach, 2011). The geometry of the northern trace, composed of the MMF and NMF, was utilized by Armijo et al. (2002) as model input to match the predicted modern velocity field to the GPS velocity field. Şengör et al. (2014) suggest an active fault geometry based on seismic reflection profiles and an analysis of fault maps produced for the Marmara Sea by other researchers (Grall et al., 2012; Le Pichon et al., 2003; Parke et al., 1999; Parke et al., 2002; Rangin et al., 2004; Sorlien et al., 2012) that correspond with the traces of the SMF, MMF, and the majority of what would be the trace of the NMF.

The fault geometries for the Marmara region determined from seismic profiles, models, and maps acknowledge the presence of small fault traces along the presumed NMF. However, none extend the NMF as a single through-going feature except for in the displacement models of Armijo et al. (2002). This indicates that the NMF may not be a significant component of the through-going active fault geometry, suggesting a second possible geometry: the SMF and the MMF make up the active fault geometry without the presence of the NMF (Figure 5.3 C) (Marmara 2). This geometry is supported by observations of fault traces made from a high

resolution bathymetric map highlighting the importance of the SMF and MMF (Le Pichon et al., 2001). Finally, in the third possible geometry, the SMF is accompanied by the MMF until its junction with the NMF, at which point the NMF is the preferred active fault geometry (Figure 5.3 D) (Marmara 3). This geometry is favored by Aksu et al. (2000) who identify the geometry of the northern trace as an expression of the northern boundary of the principal zone of deformation in the Marmara Sea. Each of these different geometries of the through-going active fault within the Marmara Region has implications for the modern distribution of stress identified though seismic focal mechanisms as well as the predicted stress orientations estimated through stress modeling. By comparing the two we can discriminate which geometry for the through-going active northern strand of the NAF produces the best match between the predicted and modeled stress fields.

5.2.2 Faulting in the Biga Peninsula region

The southern strand of the NAF bifurcates at the town of Pamukova east of the Marmara sea, and gains further complexity in the Biga Peninsula region (Figure 5.2 B) (Akşay et al., 2002; Flerit et al., 2003; Konak, 2002; Le Pichon et al., 2014; Şengör et al., 2005; Türkecan and Yurtsever, 2002). Earthquakes from a 100-year record (KOERI-UDIM, 2012), the World Seismic Map (WSM) (Heidbach et al., 2008), and the International Seismological Centre (ISC) (International Seismological Centre, 2011) (Figure 5.5 A) depict limited seismicity in the region. The northern trace in the Biga Peninsula (Etili fault) exhibits very little seismic data, and the southern trace (Edremit fault) exhibits some seismic data near the eastern boundary of the region and along the southern shore of the Biga Peninsula. The linking feature between the Etili and Edremit faults of the southern strand exhibits some amount of seismicity, indicating that it may be part of the

through-going active fault geometry. Even with limited seismic data for the two main faults, both strands are considered currently active due to their youthful morphology (Ambraseys, 1970; Sengor and Canitez, 1982). Shuttle Radar Topography Mission (SRTM) elevation data of 90 m pixels (Jarvis et al., 2008) indicates that the Etili follows narrow river valleys and areas of rapid elevation change from high to low topography (Figure 5.4). The southern trace shares these topographic expressions until it is 40 km from the Edremit Gulf. In this area, the southern trace loses all topographic expression until it reemerges near the coast of the gulf, where it follows the southern shores of the Biga Peninsula. The linking fault is expressed by a narrow river valley extending west-southwest from the southernmost trace; however, it loses its topographic expression as it nears the Etili fault. The absence of topographic expression and seismic data along the southern portion of the southern trace, and the loss of topographic expression for the linking feature, raises three possible geometries for the complexity of the southern strand of the NAF in the Biga Peninsula region.

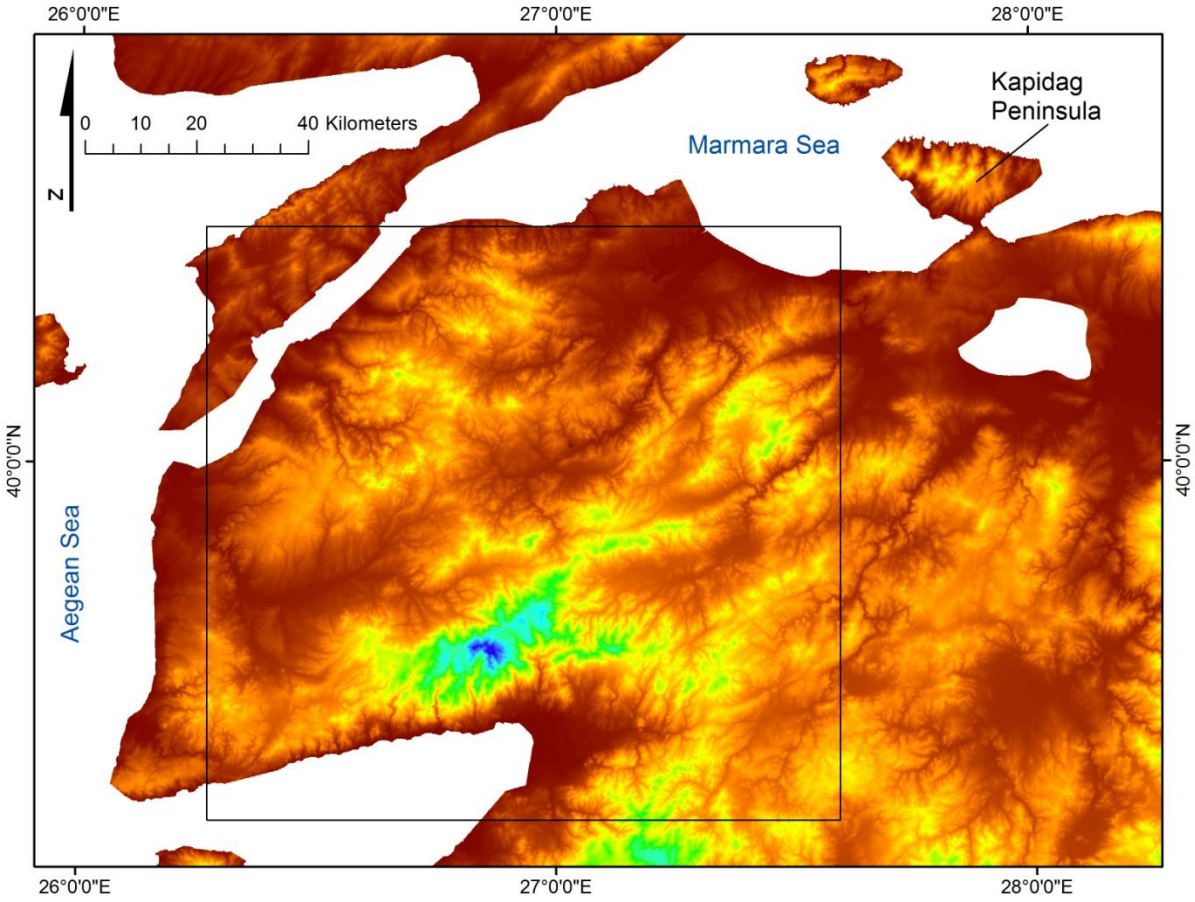

Figure 5.4 Topographic data for the Biga Peninsula and surrounding regions. Faults are most often expressed as narrow river valleys and rapid transitions from high to low topography.

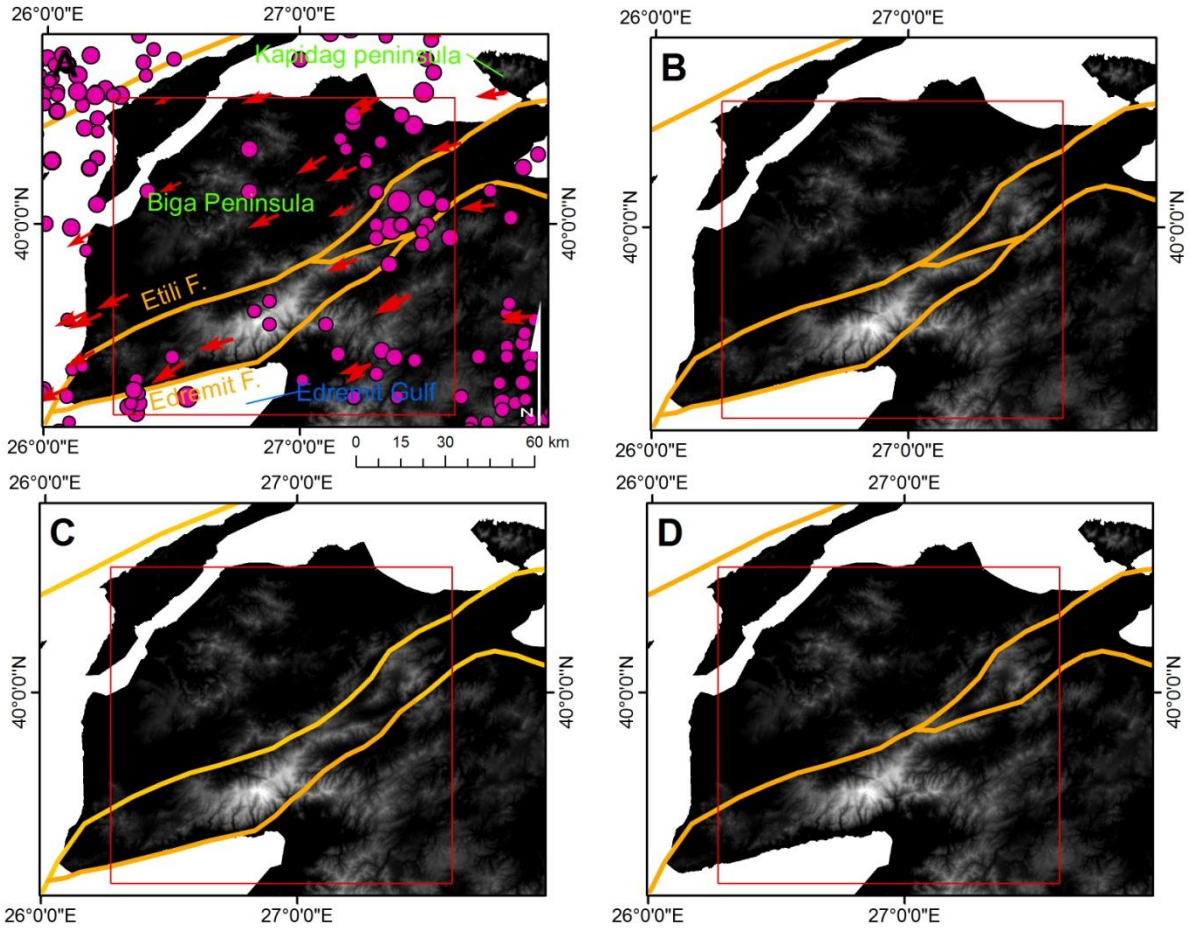

Figure 5.5 Biga Peninsula region possible faults, seismicity, and velocities. A) Possible faulting in the Biga Peninsula region with GPS vectors as red arrows (Aktug et al., 2009; Ozener et al., 2009) and the location of compiled earthquake data sized by magnitude (pink points) from a 100-year record of earthquakes (KOERI-UDIM, 2012), the WSM (Heidbach et al., 2008), and the ISC (International Seismological Centre, 2011). B-D) The three possible active fault geometries. The red boxes represent the modeled region.

The first geometry considers all the faults to be part of the greater through-going active fault geometry (Figure 5.5 B) (Biga 1). This geometry is proposed by surface mapping of faults by Şengör et al. (2005), and by descriptions of the southern strand geometry (Le Pichon et al., 2014; Şengör et al., 2014). The second geometry includes both major faults, but excludes the linking feature between them (Figure 5.5 C), as it may not fully link the Edremit with the Etili

fault due to the lack of topographic expression as it nears the Etili fault (Jarvis et al., 2008) (Biga 2). Additionally, dislocation modeling compared to GPS vectors by Flerit et al. (2003) suggests that the Edremit and Etili faults are vital to the through-going active fault geometry, but the linking feature is not. The last geometry includes the Etili fault and the northern portion of the Edremit fault until its intersection with the linking feature, which connects it to the Etili fault (Figure 5.5 D) (Biga 3). This geometry is supported by the lack of topographic expression by the Edremit fault south of the linking feature, and mapping of active fault traces (Akşay et al., 2002; Türkecan and Yurtsever, 2002). Because of several possible southern strand geometries in the Biga Peninsula region, modeling the possible through-going active fault geometries and comparing the modeled stress output to stress orientations of focal mechanisms and maximum horizontal stress as inferred from a lineament analysis can aid in discriminating between the permissible geometries.

5.3 STRESS MODELING

5.3.1 Fault parameters

A wide range of proposed static friction coefficients (μ_s) have been suggest for the NAF, with no consensus on the role of cohesion (C) on the fault interface (Hergert and Heidbach, 2011; Jiménez-Munt et al., 2006; Kasapoglu and Toksöz, 1983; Provost et al., 2003; Stein et al., 1997). Karimi it al., (in revision) constrain ranges of static friction and cohesion by comparing model rupture times of faults east of the Marmara Sea to fault recurrence intervals and maximum slip following the August 1999 Izmit earthquake sequence. They find that static friction coefficients

≤0.85 can be used to satisfy geologic conditions when paired with an appropriate cohesion value (Karimi et al., in revision): high static friction of 0.65-0.85 requires a cohesion of 300 kPa, static friction from 0.25-0.55 requires a cohesion of 400 kPa, and weak static friction of 0.0-0.2 requires a cohesion of 500 kPa (Karimi et al., in revision). A comprehensive review of experimentally derived shear strengths of filled discontinuities found clay infilling to have a cohesive force ~C=400kPa (Barton, 1974). This clay infilling is associated with schists, quartzites, and siliceous schists with higher friction values (~μ=0.6), and with montmorillonite (smectite group) clay infillings with lower friction values (~μ=0.25) (Barton, 1974). Assuming that the NAF is statically weak due to weak clay infilling of the fault gouge, Karimi et al. (in revision) suggest that the static fault conditions for the NAF could be μ_s=0.2 and C=500 kPa. We apply this pairing of static coefficient of friction and cohesion to all faults in all models, as it best replicates fault rupture times and maximum slip in the region.

5.3.2 Geometry and rock properties

The faults of the through-going active fault geometries within the Marmara and Biga Peninsula regions are used to define fault blocks (zones) and rock properties (ρ, V_p, and V_s) associated with each zone. Since the developed models are two dimensional, we use geologic data corresponding to the top kilometer of crust. Where available, we use surficial geologic data to constrain the rock properties, and where there is no surficial geology available, we use tomographic data to assign rock properties to the zones (Bayrakci et al., 2013). The resulting densities, Vp, and Vs of the zones within each region were applied to their respective blocks in models for processing with a finite element method.

5.3.2.1 Marmara region

As mentioned in section 5.2.1, three possible orientations of the active fault geometries exist within the Marmara region (Figure 5.6). In the first geometry, the through-going geometry is composed of the NMF, MMF, and SMF (Marmara 1) (Figure 5.6 A). For the second possible geometry, the NMF is no longer considered to be part of the active fault geometry (Marmara 2) (Figure 5.6 B), and in the third geometry, the SMF is accompanied by the trace of the MMF until its intersection with the NMF, where the NMF continues on as an active fault (Marmara 3) (Figure 5.6 C). We treat the faults as distinct boundaries which separate three distinct blocks/zones within the Marmara region: the Northern Marmara Zone (NMZ) north of the MMF and NMF which is part of the Eurasian tectonic plate, the Central Marmara Zone (CMZ) between the MMF, NMF, and SMF, and the Southern Marmara Zone (SMZ) south of the SMF. Since the Marmara Sea has no map of surficial rocks, we use the 3-D tomographic results of Bayrakci et al. (2013) to constrain rock properties for each zone. By evaluating the top kilometer of crust from a tomographic profile running north across the central Marmara Sea (Figure 5.7), we are able to assign compressional wave velocities (V_p) to each zone: 3600 m/s for the NMZ and SMZ, and 2700 m/s for the CMZ.

To determine the density (ρ) of each zone, we use the Database of Global Rock Properties by Dalhousie University/Geological Survey of Canada High Pressure Laboratory (DU/GSC, 2001) and find an empirical relationship between V_p and ρ for rocks under 10 MPa compression (representative of the upper kilometer of crust). Using this empirical relationship, we are able to calculate the associated density for each zone (Table 5.1). We use a V_p/V_s ratio of 1.7, which is the prescribed ratio for hard (zero-porosity) rocks (Barton, 2007) to calculate the shear wave velocity (V_s) of each zone (Table 5.1).

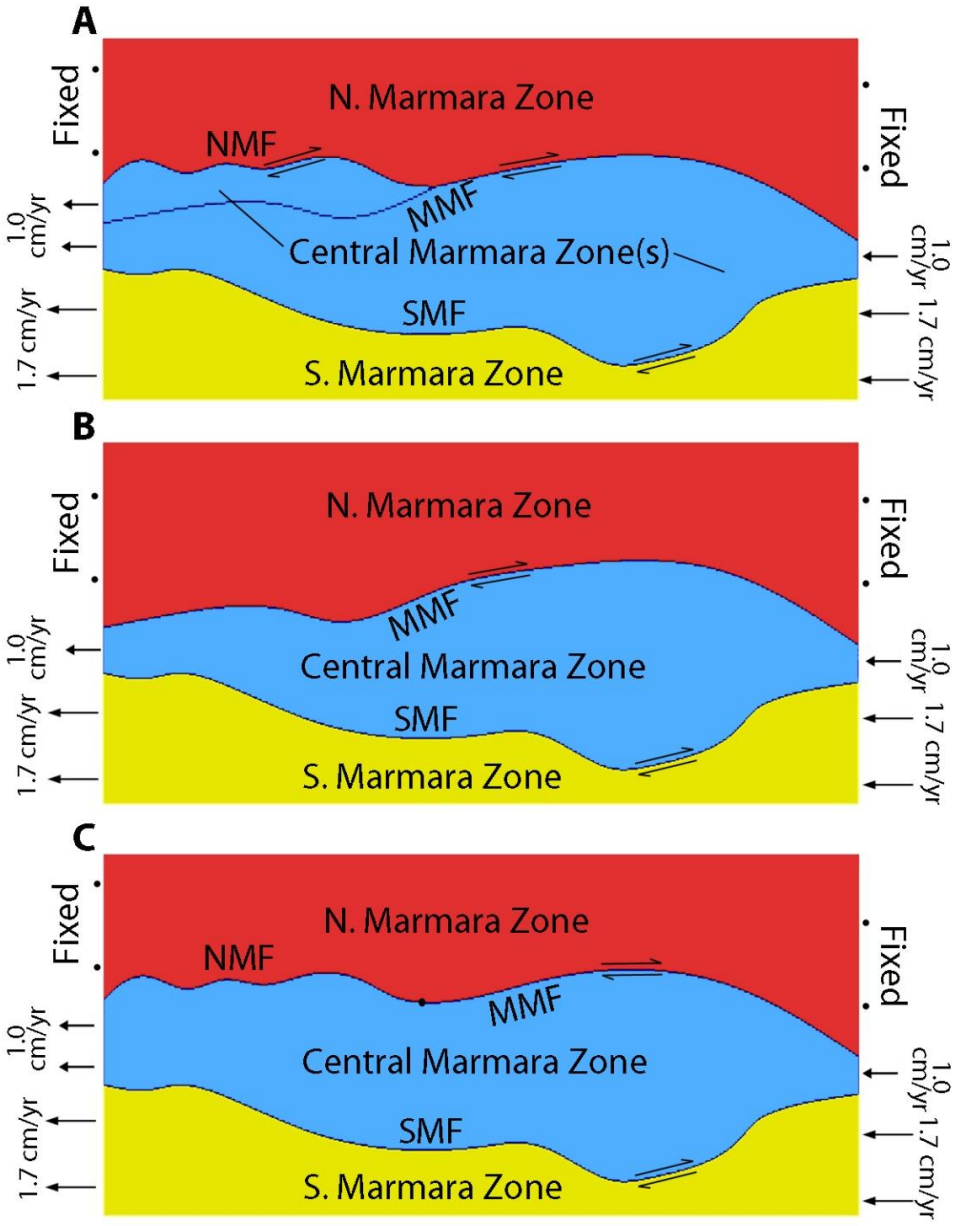

Figure 5.6 Simplified fault models of the Marmara region. A-C) Simple models of the possible fault geometries in the Marmara region depicting the three fault separated zones with velocity boundary conditions. The N. Marmara zone is always fixed and the relative rates used to push/pull the boundaries of the different blocks are consistent for all geometries. The dot on the northern trace in (C) shows the transition from the MMF to the NMF.

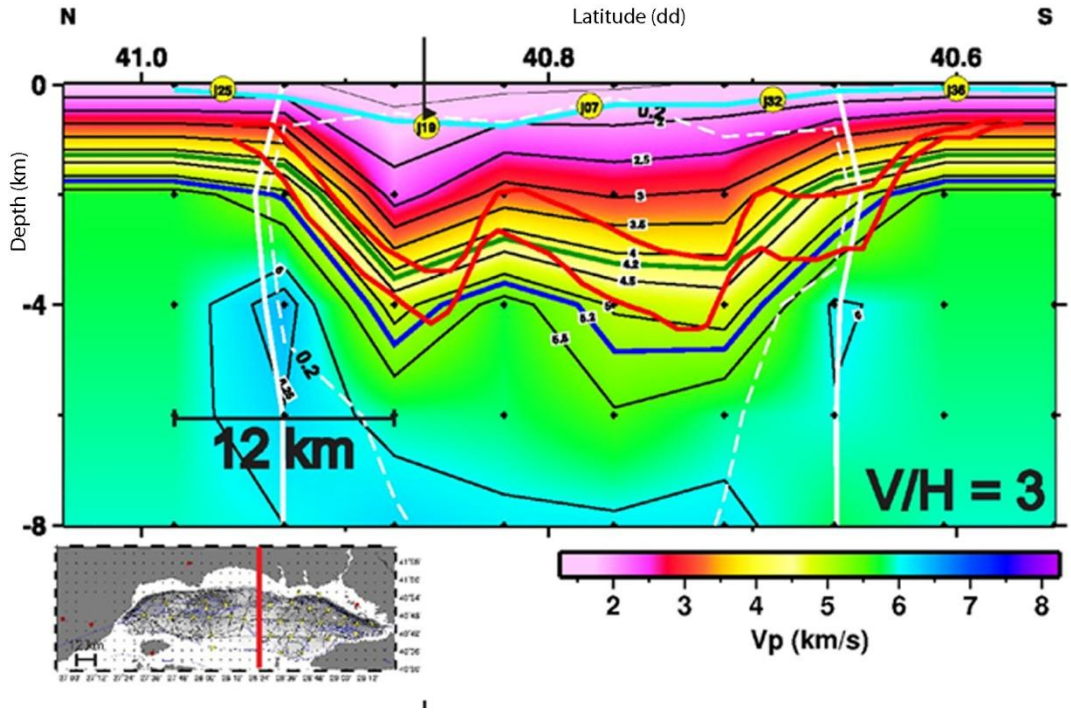

Figure 5.7 Tomographic results of a north trending line cutting through the central Marmara Sea [adapted from Bayrakci et al. (2013)]. The light blue line is the bathymetric profile.

Table 5.1 Seismic wave velocities and rock properties determined for the three zones of the Marmara region from the empirical relationship between density, V_p and V_s for a depth associated with 10 MPa compression.

Zone	Vp [m/s]	Density [kg/m^3]	Vs (1.7) [m/s]
NMZ	3600	2554	2118
CMZ	2700	2452	1588
SMZ	3600	2554	2118

5.3.2.2 Biga Peninsula region

There are three possible orientations for the active fault geometry within the Biga Peninsula region (Figure 5.8). In the first geometry, the through-going geometry is composed of the Etili, Edremit, and linking faults (Biga 1). The second geometry is similar, but without the linking feature (Biga 2), and the third geometry includes the Etili and linking fault, as well as the Edremit fault until its intersection with the linking feature (Biga 3). The faults separate three

distinct blocks/zones within the Biga Peninsula region: the Northern, Central, and Southern zones. With the availability of surficial geologic maps in this region (Konak, 2002; Türkecan and Yurtsever, 2002), the density of each zone was calculated (Table 5.2). Each block's density was calculated by weighting the general densities of the three basic rock types by their percentage of block area: 2775 kg m^{-3} for igneous rocks (Bell, 2007), 2400 kg m^{-3} for sedimentary rocks (Boyd, 2003), and 2800 kg m^{-3} for metamorphic rocks (Boyd, 2003). The densities calculated for each block were then used to extract V_p using the empirical relationship of V_p to density for rocks under 10 MPa compression described in section 3.2.1. There is very little variation of density between the regions, and thus very little variation of the seismic wave velocities.

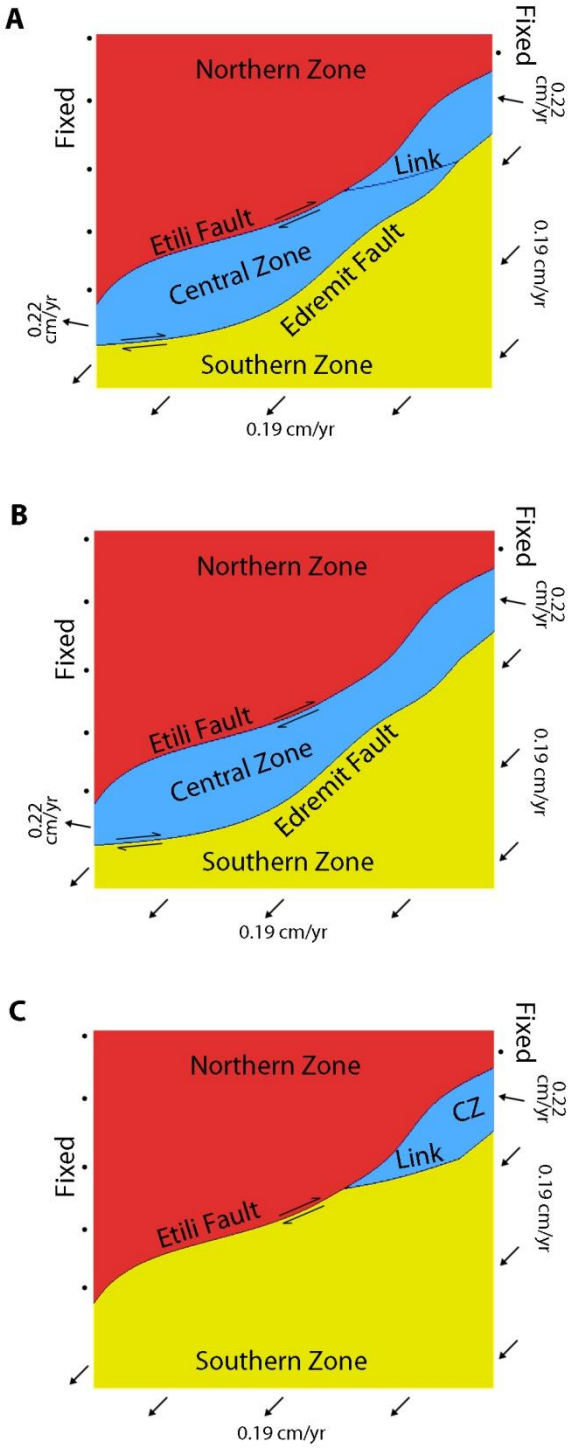

Figure 5.8 Simplified fault models the Biga Peninsula region. A-C) Simple models of the possible fault geometries in the Biga Peninsula region depicting the three fault separated zones with velocity boundary conditions. The Northern Zone is always fixed and the relative rates used to push/pull the boundaries of the different blocks are consistent for all geometries. "CZ" refers to the Central Zone.

Table 5.2 Surficial geology seen within the Biga Peninsula region for each block and rock physics parameters - density, P-wave velocity, and S-wave velocity determined for the three blocks/zones using an empirical relationship between density and V_p at 10 MPa (DU/GSC, 2001), and a V_p/V_s ratio of 1.7 (Barton, 2007). The zones share similar surface geology and therefore have density values very similar to one another.

Zone	Surficial Geology	Density [kg/m^3]	Vp [m/s]	Vs (1.7) [m/s]
Northern	Nearly equal distributions of Paleozoic-Tertiary igneous rocks and Jurassic-Quaternary sedimentary rocks. Very little Paleozoic metamorphic rocks.	2615	4141	2436
Central	Mostly Paleozoic igneous rocks, with some Paleozoic metamorphic rocks. Small amount of Jurassic-Quaternary sedimentary rocks.	2702	4905	2885
Southern	Mostly Paleozoic-Tertiary igneous rocks, some Jurassic-Quaternary sedimentary rocks, and small amounts of Paleozoic metamorphic rocks.	2672	4636	2727

5.3.3 Plate motions

The NAF, together with the conjugate East Anatolian Fault (EAF), accommodates the westward extrusion of the Anatolian plate toward the Aegean subduction zone (Hubert-Ferrari et al., 2008). The NAF and EAF meet at a triple junction of the Anatolian, Eurasian, and Arabian plates near the town of Karliova (Figure 5.1 A). Lateral forces acting upon the Anatolian plate are the NNW motion of the Arabian plate at the eastern flank of the Anatolian plate, the northern motion of the African plate in the south and west, and the relatively fixed Eurasian plate in the north. The extrusion of the Anatolian plate began some 10-12 Ma during a late phase of collision between Arabia and Eurasia (Dewey et al., 1986; Hubert-Ferrari et al., 2008; McQuarrie et al., 2003), thus initiating motion along the NAF (Barka, 1992; Şengör et al., 2005). GPS data show that the Anatolian plate has a northwest motion along the EAF, and rotates counterclockwise to a southwest orientation in the south Aegean region (McClusky et al., 2000; Reilinger et al., 2006).

Velocities in the central Anatolian plate are 24 mm/yr and 30 mm/yr in the southwest part of the plate at the Hellenic trench (Gülen et al., 2002; McClusky et al., 2000; Reilinger et al., 2006).

5.3.3.1 Marmara region

Within the Marmara region, GPS velocities in a Eurasia-fixed reference indicates 22 ± 3 mm/yr due west near the southern coast of the Marmara Sea (Straub et al., 1997). Using GPS data collected by Ozener et al. (2009), and Aktug et al. (2009), we determined velocities along the southern coast of the Marmara Sea to be ~ 20 mm/yr due west. As the model extents do not reach as far south as the southern Marmara Sea coast, we averaged the direction and velocities of GPS data within the SMZ and were able to determine a velocity of 17 mm/yr due west. In the absence of available GPS data in the CMZ, we used a velocity of 10 mm/yr due west determined from a 50 km modeled displacement for the central Marmara Sea over the last 5 Ma (Armijo et al., 1999). The NMZ is assumed to be fixed as part of the Eurasian plate, based on GPS velocity data (Aktug et al., 2009; Ozener et al., 2009). These velocities are applied to the eastern and western bounds of the blocks to push and pull the regions past one another (Figure 5.6).

5.3.3.2 Biga Peninsula region

The Biga Peninsula region is near the south Aegean, and the GPS data within this region exhibits a general NE-SW trend (Aktug et al., 2009; Ozener et al., 2009); however, variations in direction do exist in the three zones. We determine the velocities of the three zones by using GPS data from Aktug et al. (2009) and Ozener et al. (2009). None of the zones within the region are fixed, so we assign relative velocities to a fixed Northern zone (Table 5.3) to cut down on the computation time for model processing. This is done by calculating the difference in velocities for the Central and Southern zones to the Northern zone. The northern, eastern, and western

boundaries of the Northern zone are fixed, velocities are applied to the eastern and western boundaries of the Central zone, and the Southern zone has its corresponding velocity applied to its eastern, western and southern boundaries.

Table 5.3 Components of the GPS velocities for each zone in the Biga Peninsula region (Aktug et al., 2009; Ozener et al., 2009). Velocity components of the blocks are also determined for a fixed Northern Zone. A negative value in easting is westward, and a negative northing component is southward.

	Velocity Components		Velocity Components (fixed northern zone)	
Zone	E [mm/yr]	N [mm/yr]	E [mm/yr]	N [mm/yr]
Northern	-18.6	-9.1	Fixed	Fixed
Central	-20.8	-8.7	-2.2	0.4
Southern	-19.7	-10.6	-1.1	-1.5

5.3.4 Simplified models

We simplified the potential fault geometries in each region based on existing geologic maps, studies of fault geometry, and marked changes in topography identified using elevation data (see sections 5.2.1 and 5.2.2). The zones in each modeled region are prescribed a density, P-wave velocity, and S-wave velocity (Tables 5.1 and 5.2). The boundaries, if not fixed, have velocities applied to them to replicate the lateral forces acting on the region (Figures 5.6 and 5.8).

5.4 MODEL PROCESSING

PyLith (Aagaard et al., 2012) was used to process the models using finite elements. A triangular mesh was applied to each model with a grid spacing of 3 km along the outer boundaries and a

finer grid of 2 km near the faults. The grid spacing is used as input to create a finer set of triangular cells near the faults, and then grading into a coarser mesh near the boundaries. The models are processed using the rock physics and fault parameters described in Section 5.3, and the block's respective velocities in each region are applied as quasi-static dirichlet boundary conditions. Once the static friction and cohesion assigned to the faults is overcome, the blocks slip along the faults at a steady rate. The models are processed for a thousand years, at a five year interval, to allow the stress field to develop enough to cause slip along the full length of the modeled faults while avoiding large distortions within the model areas due to displacements.

We calculate the orientation and magnitude of the maximum principal stress (σ_1) at the center of each triangular cell, or the maximum horizontal stress in a 2-dimensional model. We identify the orientation of the maximum principal stress for the regions by constructing rose-diagrams of the frequency of σ_1 orientation for the models of the two regions, and comparing them to the maximum horizontal stress from a record of focal mechanisms and inferred from a lineament analysis where topographic data is available.

5.4.1 Marmara region results

The rose-diagrams of the maximum horizontal stress orientation frequency for the three models of the Marmara region are shown in Figure 5.9. For Marmara 1 (Figure 5.9 A), the largest peak associated with σ_1 can be seen at the interval from 105°-110°, with a secondary peak at 125°-130°. For Marmara 2 and Marmara 3 (Figures 5.9 C and E, respectively), the largest peaks are at the interval from 105°-110°. Weighting the principal stress orientations by their respective magnitudes (as absolute values), we see that the primary peak for Marmara 1 is now at 090°-095°, with no secondary peak (Figure 5.9 B). The primary peak in Marmara 2 'shifts' slightly to

100°-105°, with two very minor peaks at 085°-095° and 115-120°. Weighting the orientations of the maximum principal stress for both Marmara 2 and 3 by the absolute value of their respective magnitude presents a large peak at 100°-105°, with a minor peak at 080°-095°.

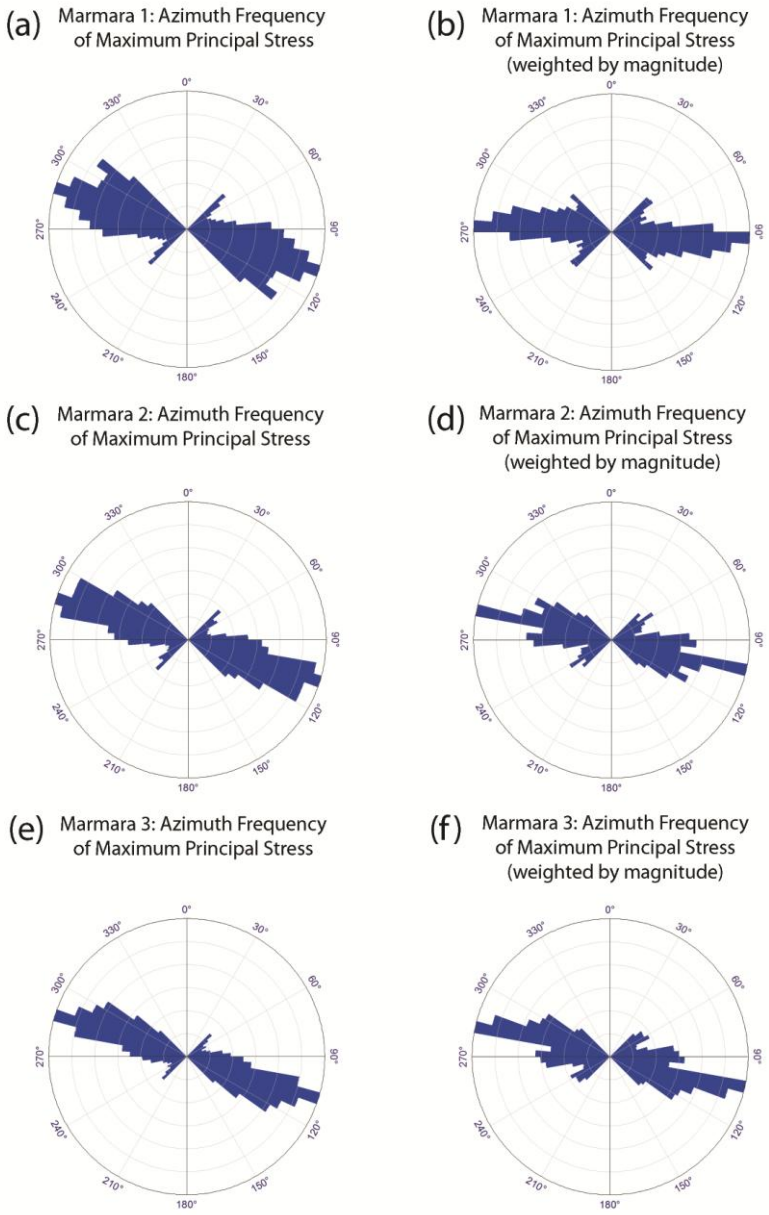

Figure 5.9 Marmara region modeled results. Rose diagrams depicting frequency and magnitude-weighted frequency of modeled azimuths of the maximum principal stress for Marmara 1 (A, B), Marmara 2 (C, D), and Marmara 3 (E, F).

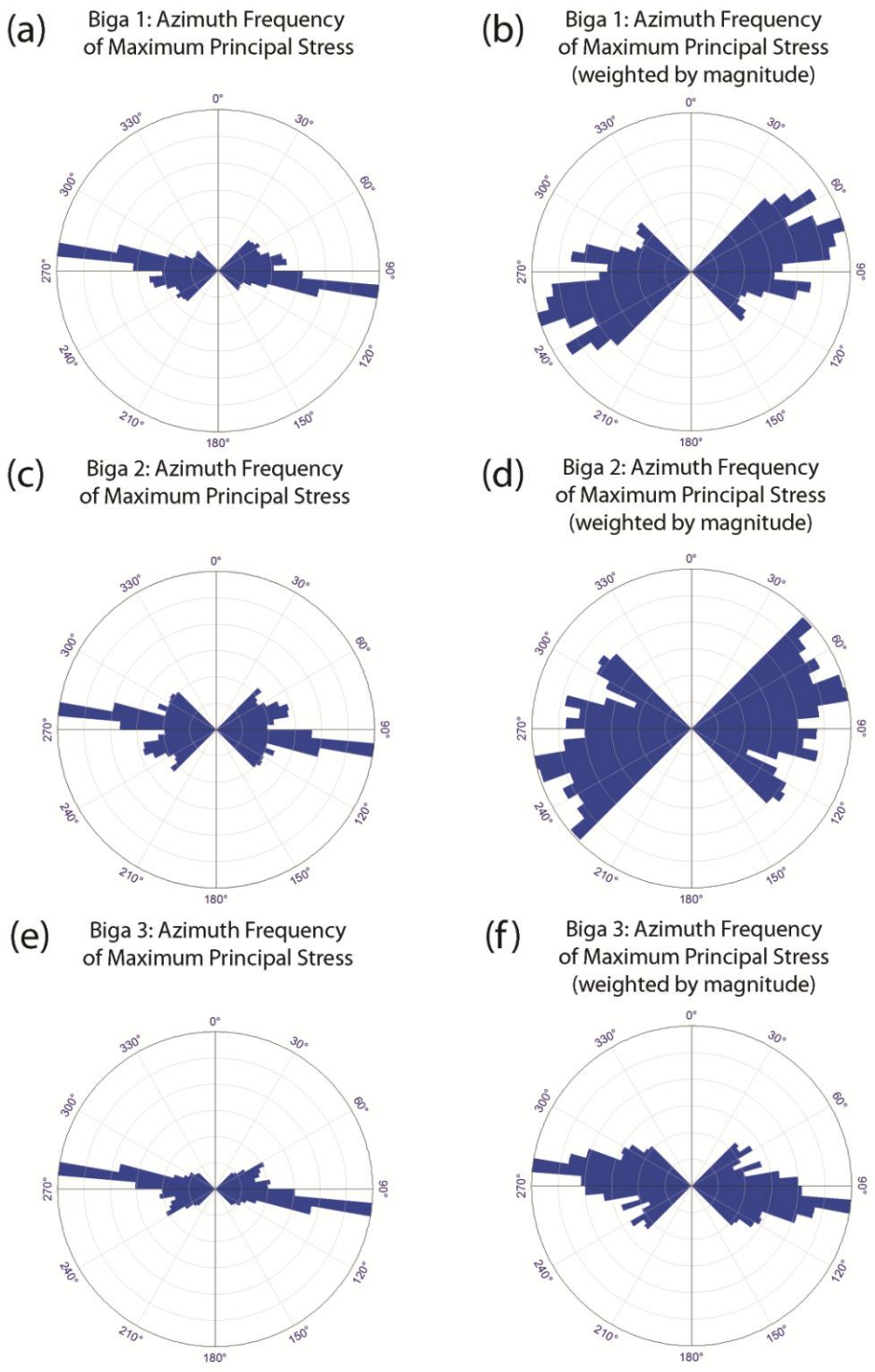

Figure 5.10 Biga Peninsula region modeled results. Rose-diagrams depicting frequency and magnitude-weighted frequency of modeled azimuths of the maximum principal stress for Biga 1 (A, B), Biga 2 (C, D), and Biga 3 (E, F).

5.4.2 Biga Peninsula region results

The rose-diagrams of the maximum horizontal stress orientation frequency for the three models of the Biga Peninsula region are shown in Figure 5.10. For the plot representing the results of Biga 1 (Figure 5.10 A), the largest peak associated with σ_1 can be seen at the interval from 095°-100°. Biga 2 also results in a peak at 095°-100° (Figure 5.10 C), a dominant orientation shared by Biga 3 (Figure 5.10 E). Weighting the principal stress orientations by their respective magnitudes (as absolute values), the primary peak for Biga 1 is now at 060°-085°, with a secondary peak at 050°-060°, and a tertiary peak at 95°-105° (Figure 5.10 B). The magnitude weighted results of Biga 2 share three peak orientations as well: a primary peak at 070°-080°, a secondary peak at 045°-050°, and a tertiary peak at 060°-065° (Figure 5.10 D). The primary peak between the unweighted and weighted maximum principal stress orientations for Biga 3 do not vary (Figure 5.10 F).

5.5 INTERPRETATION

5.5.1 Marmara region

We collected seventy-five focal mechanism data associated with several seismic events located within a 10 km buffer of the modeled Marmara region from the International Seismological Centre (International Seismological Centre, 2011) and the World Stress Map (Heidbach et al., 2008). Data from these two sources are recordings from global stations. To determine the maximum horizontal stress, we first found the orientation of kinematic axes for the region by

evaluating the axes with contours. These orientations, separated by 90°, were used to construct a regional focal mechanism to determine the orientation of maximum horizontal stress, which is approximately 115° within 10 km of our modeled region. Our calculated maximum horizontal stress orientation is smaller than those determined for regions broader than that of our modeled area: 125° inferred from a maximum horizontal stress grid developed by Hergert and Heidbach (2011), 145° determined by Kiratzi et al. (2002), and the approximation of 130° suggested by Örgülü (2011). For comparison to the model, we use an average of 128° based on our results and those of the various studies (Hergert and Heidbach, 2011; Kiratzi, 2002; Örgülü, 2011). The unweighted results of all the models of the region have primary peaks with trends (105°-110°) (Figure 5.9) in the general direction of maximum horizontal stress orientation inferred from focal mechanism data. Weighting the stress orientations produces a primary trend due east-west in Marmara 1, which much more strongly deviates from the regional 128° from focal mechanism data. Marmara 2 and 3 orientations both continue to have primary peaks at 100°-105° when the frequency of orientations is weighted by magnitude. With so little difference between Marmara 2 and 3, we looked at the modeled stress orientations within a 5 km buffer of their respective modeled fault geometries, and found that in the unweighted frequency orientations a primary peak is evident at 100°-105°. When the frequency of orientations for the two models are weighted by magnitude, a primary peak is still evident at 100°-105°, and a secondary peak appears at 050°-065°. Since there is very little difference between the modeled stress field orientations of the two models, we cannot differentiate between Marmara 2 and Marmara 3 as the through-going active fault geometry. It is likely that both are not equally active based on the stress orientations from Marmara 1, which has both the MMF and NMF present. However, we observe that Marmara 3 best represents the through-going active fault geometry within the

Marmara region, which resemble the traces of northern and southern bounds for a principal zone of deformation associated with the developing Marmara basin (Aksu et al., 2000).

5.5.2 Biga Peninsula region

5.5.2.1 Lineament analysis

Tectonic features such as faults and fractures may exert a strong control on topographic patterns due to these features creating pathways for weathering and erosion. Using elevation data, we can highlight topographic lineaments and evaluate the potential control of tectonic induced deformation on topography. Lineament mapping was manually performed using a 90 m resolution Shuttle Radar Topography Mission (SRTM) image (Jarvis et al., 2008) of elevation for the Biga Peninsula region. Hill-shades were applied to the SRTM image to highlight topographic changes. The hill-shades were performed at a 45° vertical sun-angle, as linear features were most evident at this angle. The azimuthal direction of the incoming solar radiation was rotated around the image at 45° increments, creating a series of filtered images.

Manually picking lineaments allowed us to preferentially pick lineaments that are not man-made structures, such as roads, or railways. While there may be lineaments picked that do not have a tectonic source, they are outnumbered and outweighed by lineaments that share similar orientations to mapped faults (Konak, 2002; Türkecan and Yurtsever, 2002). To account for the curvature of lineaments, we split each feature into 10 sections and calculated the azimuth for each of those sections. Using these 10 azimuths, we calculated an average azimuth and standard deviation for the orientation of each line. All the manually picked lineaments in the Biga Peninsula Region had standard deviations close to zero, with the greatest deviation being about 10°.

The main fault (MF) feature in the results of orientation frequency (Figure 5.11 A) is located between 045° and 060°. There is a secondary peak located at 025°-030°, and a third peak at 080°-090°. Without knowing if any of the faults within the region are reactivated structures, we assume that the structures that are reactivated are optimally oriented in the driving stress field. Additionally, we assume that the main feature is the orientation of the faults within the Biga Peninsula region. The mapped faults have an average trend of 065°, which is only slightly higher than the maximum main feature orientation of 060°. Peaks other than that of the primary feature are likely associated with Riedel shear features such as R-sears, R'-shears, P-shears, and extensional fractures (Figure 5.10). With Riedel shearing, the maximum principal stress is 45° clockwise (for right-lateral faults) from the main faults, intersecting the R- and R'-shears that are characteristic of strike-slip faulting (Davis, 1999; Riedel, 1929; Wilcox et al., 1973). With a clockwise rotation of 45° from the main lineament feature, the stress orientation would be between 090° and 105°. This inferred stress orientation overlaps with a minor peak (080°-095°), that is an appropriate orientation to represent extensional fracturing. By weighing the lineaments according to their length (Figure 5.11 B), the array of peaks diminishes and resolves into one very prominent feature trending 050°-060°. This tightens our σ_1 orientation to 095°-105°. We propose that the feature at 050°-060° is the "main fault" (MF) trend and plot the orientation of Riedel shears (Figure 5.11): R-shears at 65°, R'-shears at 125°, and P-shears at 40°. Both the average frequency as well as the frequency weighted by length show prominent features in potential orientations of R and P shears. The presence of these orientations corresponding to these shears helps validate the resolved orientation of σ_1 (090°-105°). This is supported by studies of stress along the NAF system, which suggest that the maximum compressive stress is generally oriented at 35°-45° with respect to the fault trend (Dresen et al., 2007; Kiratzi, 2002).

The resolved orientation of σ_1 (090°-105°) from the lineament analysis overlaps the primary peaks in the unweighted frequency orientations for all models of the Biga Peninsula region. When weighting the modeled stress orientations by their magnitude, the primary peak disappears in the rose plots of Biga 1 and 2, but remains as the dominant feature in Biga 3. For the weighted results of Biga 1 and 2, the northeast-southwest trending prominent features do not overlap with any prominent lineament features. The overlap of both the unweighted and weighted modeled stress field orientations of Biga 3 with the results of the lineament analysis indicates that Biga 3 is the best candidate for the representation of fault geometry. To confirm this, we compare the FEM stress orientation results with data from seismic events in the next section.

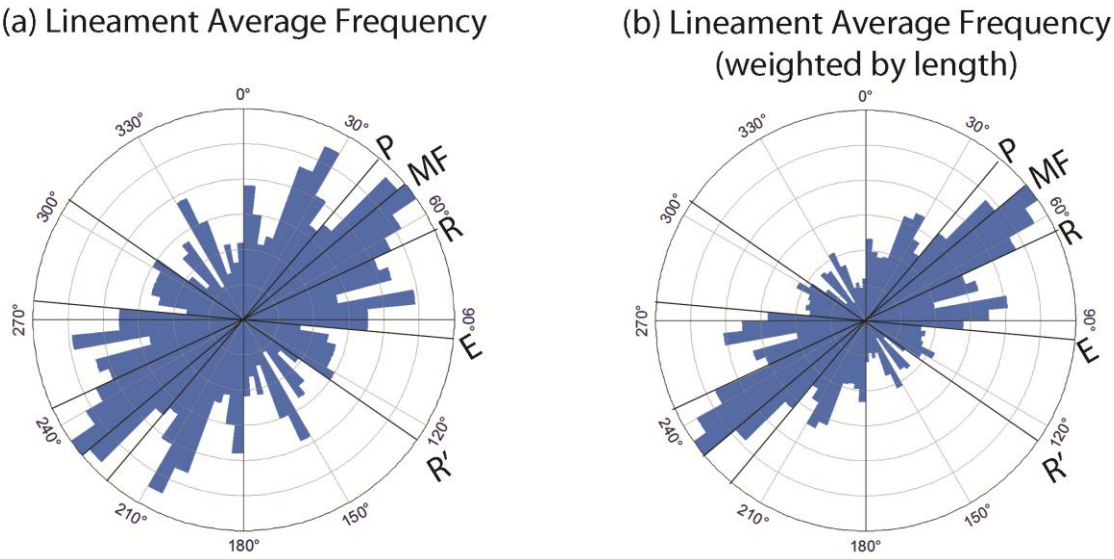

Figure 5.11 Biga Peninsula region lineament analysis results. A) Rose-diagram of lineament frequency orientation, and B) of lineament frequency orientation weighted by length. Both plots are overlain by Riedel shear orientations (R and R'), P-shears, and extensional features (E) at angles to the main fault (MF) trend, as expected in shear zones.

5.5.2.2 Focal mechanism data

We collected seventeen focal mechanism data from global stations associated with several seismic events located within a 10 km buffer of the modeled Biga Peninsula region from the International Seismological Centre (International Seismological Centre, 2011) and the World Stress Map (Heidbach et al., 2008). We determined the trend of the maximum horizontal stress by first determining the orientation of the P kinematic axis, which we assumed to be synonymous with σ_1. Applying density contours to the P kinematic axes, we were able to procure a nearly horizontal (<5°) orientation for the regional P axis at approximately 110°. This orientation matches the regional maximum horizontal stress orientation of 110° inferred from a horizontal stress grid developed by Hergert and Heidbach (2011), but is slightly greater than the 100° inferred for the region from horizontal stresses for the Northern Aegean and Anatolia southwest of the Biga Peninsula by Kiratzi et al. (2002). The unweighted results of all the models of the region have primary peaks with similar trends (095°-100°) (Figure 5.10); however, weighting the stress orientations shifts the prominent features to a northeast-southwest trend for Biga 1 and 2. This trend is not seen in the focal mechanism data and is fault-parallel in the immediate area around the faults, except for the northernmost portion of the Etili Fault north of the linking feature. Biga 3 does not share this mis-oriented feature, and its range of stress orientation (080°-110°) with its prominent 095°-100° orientation overlaps the maximum horizontal stress determined from focal mechanism data (Heidbach et al., 2008; International Seismological Centre, 2011), and regional stress studies (Hergert and Heidbach, 2011; Kiratzi, 2002). We confirm that Biga 3 is the geometry of the through-going active faults in the Biga Peninsula region, as it best matched the inferred maximum horizontal stress orientation inferred from a lineament analysis and a study of focal mechanisms.

5.6 THROUGH-GOING ACTIVE FAULT GEOMETRY

West of the town of Bolu, the NAF splits into a northern and southern strand which converge at the Mudurnu Valley and then diverge to border the northern and southern shores of the Marmara Sea (Figure 5.1). The two strands are linked at their convergence through the Mudurnu Valley (Karimi et al., 2014). Further west, the northern strand bifurcates in the Gulf of Izmit, where comparison of modeled stress fields to a record of focal mechanisms indicates that the through-going active northern trace of the bifurcated northern strand continues on as the MMF until its intersection with the NMF, at which point the northern trace could either continue on as the NMF or the MMF. Because the continuation of the MMF as the NMF describes a northern side wall of a principal zone of deformation for an unconventional negative flower structure (Aksu et al., 2000), we suggest it as the best representation of the northern components fault geometry. The two traces converge as a single trace at the western edge of the Marmara Sea as the Ganos Fault, and the northern strand cuts across land into the Saros Gulf and into the Northern Aegean. The southern strand splits into two main traces at the town of Pamukova. The northernmost trace continues to border the southern coast of the Marmara Sea until the Kapidag Peninsula, where it deviates to a southwest orientation as the Etili fault in the Biga Peninsula. The southernmost trace borders the southern coasts of lakes Ulubat and Kuş, after which it trends southwest, as the Edremit fault, until it follows the southern shore of the Biga Peninsula. Stress modeling, compared to maximum horizontal stress orientations from a record of focal mechanisms and inferred from a lineament analysis, suggests that the active fault geometry includes the convergence of the southern trace to the Etili fault through a linking structure centralized in the Biga Peninsula. The now converged traces of the southern strand continue on as the Etili fault, which extends into the Aegean (Figure 5.12).

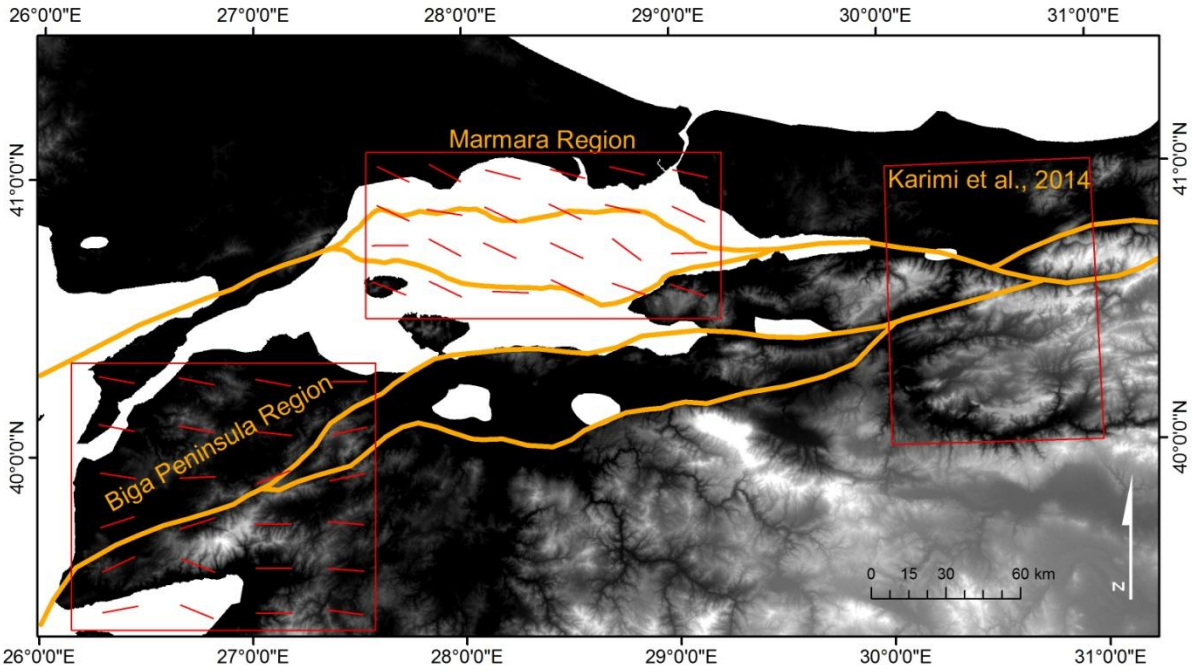

Figure 5.12 The geometry of the through-going NAF with the two studied regions, and the region east of the Marmara Sea studied by Karimi et al. (2014) in red boxes. The NAF in the Marmara region is composed of active fault traces, which bound the principal deformation zone for the developing Marmara basin. In the Biga Peninsula region, the active traces of the NAF converge through a linking feature and continue to the Aegean Sea through the Biga Peninsula at its southwest corner. In both the Marmara and Biga Peninsula regions, a generalized stress field of the final selected models is depicted as red lines oriented in the orientation of the maximum modeled stress.

5.7 CONCLUSION

Through stress modeling constrained by a record of focal mechanism data and paleostress inferred from lineament analyses, the through-going active fault geometry of the NAF was determined for the Marmara and Biga Peninsula regions. The NAF bifurcates near the town of Bolu into two strands, which are linked as they near each other through the Mudurnu Valley.

West of the valley, the northern strand heads into the Marmara Sea, bifurcating in the Gulf of Izmit. The two traces associated with the bifurcation of the northern strand bound the principal deformation zone associated with the developing Marmara basin, and then converge again into a single trace as the Ganos fault and into the Gulf of Saros and the Aegean Sea. The southern strand bifurcates at the town of Pamukova, and its northern component follows the southern Marmara Sea coast until the Kapidag Peninsula, where it trends southwest across the Biga Peninsula and exits into the Aegean Sea. The southernmost trace parallels the first trace, but below Lakes Kuş and Ulubat. West of Lake Kuş, it trends southwest and links to the first trace via a linking structure in a valley within the Biga Peninsula. We proposed this fault geometry as a working hypothesis of the through-going active geometry of the larger western NAF. To further test this geometry, a stress model over the entirety of the western NAF should be developed to leave no gaps in the development of the stress field between the city of Bolu and the Aegean Sea.

APPENDIX A

FOCAL MECHANISM DATA

Table A.1 Focal mechanism data east of the Marmara Sea (Heidbach et al., 2008; International Seismological Centre, 2011).

EVENT_ID	AUTHOR	LAT	LON	DEPTH	MO	MW	T_PL	T_AZM	P_PL	P_AZM	N_PL	N_AZM
566916	NEIS	40.1270	29.3770	14.00	1.64	5.40	0.00	172.00	0.00	82.00	90.00	180.00
1655218	MOS	40.8490	30.0130	10.00	9.50	7.30	0.00	225.00	16.00	135.00	74.00	315.00
1655218	ZUR_RMT	40.6400	29.8300	12.00	2.12	7.50	2.00	42.00	24.00	312.00	66.00	136.00
1655218	NEIC	40.7480	29.8640	17.00	1.40	7.40	6.00	50.00	6.00	319.00	81.00	187.00
1655218	HRVD	41.0100	29.9700	17.00	2.90	7.60	13.00	45.00	10.00	138.00	73.00	262.00
1655290	MED_RCMT	40.5700	30.5700	10.00	10.54	4.60	20.00	263.00	60.00	33.00	21.00	164.00
1655292	MED_RCMT	40.6700	29.0300	10.00	1.20	4.70	12.00	18.00	76.00	162.00	8.00	286.00
1655294	HRVD	40.6800	29.1000	15.00	6.30	5.10	4.00	204.00	69.00	104.00	21.00	295.00
1655332	MED_RCMT	40.5000	29.1700	19.70	2.18	4.80	1.00	21.00	55.00	112.00	35.00	290.00
1655596	ZUR_RMT	40.7900	29.9400	12.00	5.63	5.10	5.00	20.00	47.00	284.00	42.00	114.00
1655596	HRVD	40.4300	30.2500	15.00	6.60	5.10	27.00	191.00	47.00	314.00	31.00	84.00
1655598	MED_RCMT	40.6800	29.9300	15.80	7.34	4.50	15.00	182.00	55.00	294.00	31.00	83.00
1718165	MED_RCMT	40.8000	29.2500	15.00	11.62	4.00	19.00	39.00	32.00	297.00	52.00	155.00
1655942	ZUR_RMT	40.7000	30.0180	12.00	6.47	5.80	5.00	216.00	4.00	307.00	83.00	79.00
1655942	NEIC	40.7090	30.0450	13.00	6.70	5.80	36.00	242.00	30.00	128.00	40.00	9.00
1655942	HRVD	40.3100	30.2900	15.00	6.00	5.80	18.00	226.00	24.00	128.00	59.00	350.00
1656016	MED_RCMT	40.4200	28.6900	17.20	2.07	4.80	12.00	197.00	58.00	86.00	29.00	294.00
1656586	HRVD	40.5500	29.6900	15.00	6.90	5.20	23.00	26.00	34.00	279.00	47.00	144.00
1644746	MED_RCMT	41.1700	29.0400	10.00	5.55	5.10	27.00	239.00	20.00	339.00	56.00	100.00
1649575	HRVD	40.5700	31.3600	15.00	3.20	4.90	61.00	203.00	24.00	346.00	15.00	83.00
1649955	ZUR_RMT	40.8000	30.2600	12.00	3.26	5.60	0.00	253.00	1.00	343.00	89.00	148.00
1649955	CSEM	40.8000	30.2600	12.00	3.80	5.70	20.00	258.00	10.00	165.00	68.00	49.00
1649955	NEIC	40.7440	30.2660	22.00	3.50	5.60	32.00	257.00	27.00	148.00	45.00	26.00
1649955	HRVD	40.9500	30.1000	15.20	3.60	5.60	24.00	262.00	31.00	156.00	49.00	23.00
1649955	HRVD	40.9400	30.1300	15.00	3.60	5.60	23.00	260.00	30.00	157.00	48.00	19.00
1734154	ZUR_RMT	40.8030	30.2440	21.00	6.61	4.50	8.00	14.00	1.00	283.00	81.00	184.00
1734154	MED_RCMT	41.0000	30.2800	10.00	7.09	4.50	39.00	357.00	41.00	133.00	24.00	246.00
1747181	ZUR_RMT	40.8000	29.2600	15.00	6.02	4.50	5.00	40.00	82.00	275.00	7.00	131.00
1739330	MED_RCMT	40.7900	30.7600	15.20	8.58	5.20	1.00	28.00	20.00	298.00	70.00	120.00
1739330	HRVD	40.6800	30.7200	15.30	1.00	5.30	10.00	205.00	35.00	108.00	53.00	309.00
1739330	ZUR_RMT	40.6800	30.7200	30.00	1.98	5.50	0.00	204.00	10.00	294.00	80.00	112.00
6845500	ZUR_RMT	40.8240	30.9650	18.00	4.58	4.40	7.00	208.00	3.00	118.00	82.00	8.00
6845500	MED_RCMT	40.8900	31.0300	24.30	3.22	4.30	1.00	213.00	3.00	123.00	87.00	321.00
11122235	GCMT	40.4600	28.9800	14.30	4.67	5.00	4.00	6.00	44.00	100.00	45.00	272.00

Table A.2 Focal mechanism data for the Marmara Sea region(Heidbach et al., 2008; International Seismological Centre, 2011).

EVENT_ID	AUTHOR	LAT	LON	DEPTH	MO	MW	T_PL	T_AZM	P_PL	P_AZM	N_PL	N_AZM
11122235	GCMT	40.46	28.98	14.30	4.67	5.00	4.00	6.00	44.00	100.00	45.00	272.00
1655292	MED_RCMT	40.67	29.03	10.00	1.20	4.70	12.00	18.00	76.00	162.00	8.00	286.00
1655332	MED_RCMT	40.50	29.17	19.70	2.18	4.80	1.00	21.00	55.00	112.00	35.00	290.00
1718165	MED_RCMT	40.80	29.25	15.00	11.62	4.00	19.00	39.00	32.00	297.00	52.00	155.00
1747181	ZUR_RMT	40.80	29.26	15.00	6.02	4.50	5.00	40.00	82.00	275.00	7.00	131.00
7759214	ZUR_RMT	40.61	27.70	24.00	1.74	4.10	4.00	85.00	18.00	354.00	72.00	188.00
1656016	MED_RCMT	40.42	28.69	17.20	2.07	4.80	12.00	197.00	58.00	86.00	29.00	294.00
1655294	HRVD	40.68	29.10	15.00	6.30	5.10	4.00	204.00	69.00	104.00	21.00	295.00
603494283	GCMT	40.80	27.72	12.00	5.36	5.10	20.00	208.00	33.00	312.00	49.00	93.00
2932753	MED_RCMT	40.85	27.76	16.90	5.03	4.40	2.00	215.00	67.00	310.00	23.00	124.00
441447	HRVD	40.77	28.73	15.00	10.42	5.30	6.00	221.00	21.00	314.00	68.00	115.00
1644746	MED_RCMT	41.17	29.04	10.00	5.55	5.10	27.00	239.00	20.00	339.00	56.00	100.00
SEA1211		40.90	29.20	33.00			11.00	28.00	77.00	241.00	7.00	120.00
SEA3554		40.67	29.03	10.00			12.00	18.00	76.00	162.00	8.00	286.00
SEA3567		40.42	28.69	17.20			13.00	197.00	58.00	86.00	29.00	294.00
SEA4093		40.68	29.10	15.00			4.00	204.00	69.00	105.00	21.00	296.00
SEA7461		40.69	27.57	11.00			41.00	220.00	26.00	105.00	39.00	353.00
SEA7462		40.71	27.59	11.00			40.00	211.00	24.00	99.00	40.00	347.00
SEA7463		40.69	29.21	14.00			36.00	36.00	34.00	277.00	36.00	157.00
SEA7464		40.83	27.97	11.00			38.00	223.00	25.00	335.00	41.00	89.00
SEA7465		40.72	27.59	11.00			23.00	232.00	37.00	123.00	45.00	346.00
SEA7466		40.78	29.03	16.00			21.00	67.00	28.00	325.00	54.00	190.00
SEA7470		40.77	29.07	11.00			13.00	258.00	25.00	162.00	62.00	13.00
SEA7471		40.70	27.57	11.00			19.00	84.00	58.00	208.00	25.00	345.00
SEA7472		40.79	29.00	8.00			24.00	254.00	3.00	345.00	65.00	81.00
SEA7473		40.79	29.04	11.00			4.00	252.00	6.00	162.00	83.00	19.00
SEA7475		40.76	29.12	11.00			11.00	68.00	8.00	160.00	76.00	286.00
SEA7476		40.75	29.11	11.00			16.00	65.00	15.00	159.00	68.00	289.00
SEA7477		40.76	29.11	11.00			8.00	67.00	6.00	158.00	80.00	281.00
SEA7478		40.83	28.58	14.00			60.00	115.00	23.00	337.00	18.00	239.00
SEA7479		40.75	29.09	5.00			5.00	64.00	29.00	156.00	60.00	325.00
SEA7480		40.84	28.83	11.00			12.00	239.00	16.00	332.00	70.00	114.00
SEA7481		40.76	29.13	13.00			18.00	60.00	6.00	152.00	71.00	261.00
SEA7482		40.83	28.81	11.00			12.00	61.00	41.00	321.00	47.00	165.00
SEA7483		40.84	28.77	11.00			1.00	237.00	47.00	147.00	43.00	328.00
SEA7484		40.79	28.41	5.00			1.00	56.00	20.00	146.00	70.00	323.00
SEA7485		40.76	29.11	15.00			6.00	50.00	10.00	319.00	79.00	170.00
SEA7486		40.76	27.51	8.00			18.00	229.00	4.00	138.00	72.00	36.00
SEA7487		40.57	28.10	15.00			29.00	230.00	4.00	138.00	61.00	40.00

(continued)

SEA7488		40.62	27.82	11.00			4.00	222.00	20.00	313.00	70.00	121.00
SEA7491		40.86	27.67	12.00			8.00	34.00	57.00	291.00	32.00	129.00
SEA7492		40.85	27.64	17.00			31.00	29.00	14.00	127.00	55.00	239.00
SEA7494		40.83	28.74	5.00			27.00	214.00	1.00	305.00	63.00	38.00
SEA7496		40.69	29.16	7.00			29.00	23.00	14.00	121.00	57.00	233.00
SEA7497		40.90	29.14	8.00			4.00	209.00	27.00	117.00	62.00	307.00
SEA7499		40.70	27.57	11.00			42.00	216.00	13.00	115.00	45.00	11.00
SEA7501		40.44	28.76	17.00			23.00	208.00	19.00	110.00	60.00	344.00
SEA7505		40.71	27.58	5.00			29.00	185.00	56.00	40.00	16.00	284.00
SEA7508		40.84	29.19	5.00			18.00	13.00	52.00	128.00	32.00	271.00
SEA7510		40.79	27.48	11.00			20.00	194.00	69.00	357.00	5.00	102.00
SEA7514		40.69	29.22	5.00			16.00	4.00	31.00	264.00	54.00	117.00
SEA7519		40.71	27.56	5.00			19.00	181.00	2.00	90.00	71.00	353.00
SEA7521		40.70	27.59	5.00			55.00	187.00	5.00	89.00	35.00	355.00
SEA7522		40.71	27.59	8.00			38.00	169.00	13.00	269.00	49.00	15.00
SEA7527		40.72	27.60	14.00			56.00	189.00	9.00	85.00	33.00	349.00
SEA7528		40.79	28.71	20.00			65.00	102.00	24.00	265.00	7.00	358.00
SEA7536		40.80	27.84	12.00			47.00	335.00	14.00	80.00	40.00	182.00
SEA7540		40.72	27.60	5.00			23.00	165.00	4.00	257.00	66.00	357.00
SEA7544		40.74	27.54	14.00			60.00	189.00	14.00	74.00	26.00	337.00
SEA7546		40.82	27.77	12.00			12.00	335.00	58.00	226.00	29.00	72.00
SEA7767		40.85	27.76	16.90			2.00	215.00	67.00	309.00	23.00	124.00
SEA9700		40.46	28.98	14.30			4.00	6.00	44.00	100.00	45.00	272.00
TUR125		40.60	29.16	2.00			22.00	40.00	67.00	206.00	5.00	308.00
TUR128		40.64	29.15	11.00			17.00	212.00	42.00	106.00	43.00	319.00
TUR129		40.60	29.10	2.00			1.00	33.00	65.00	125.00	25.00	302.00
TUR134		40.61	29.16	6.00			2.00	208.00	56.00	114.00	34.00	299.00
TUR139		40.60	29.06	5.00			4.00	21.00	70.00	121.00	20.00	290.00
TUR145		40.59	29.05	2.00			2.00	14.00	72.00	109.00	18.00	283.00
TUR146		40.65	29.09	1.00			13.00	196.00	68.00	321.00	17.00	102.00
TUR153		40.56	29.13	5.00			13.00	11.00	72.00	144.00	13.00	278.00
TUR155		40.59	29.12	5.00			4.00	352.00	66.00	91.00	24.00	260.00
TUR156		40.60	29.13	5.00			4.00	349.00	23.00	81.00	67.00	250.00
TUR158		40.62	29.18	8.00			22.00	349.00	58.00	119.00	22.00	249.00
TUR86		40.50	29.17	19.70			1.00	21.00	54.00	112.00	36.00	290.00
TUR90		41.17	29.04	10.00			27.00	239.00	19.00	339.00	56.00	101.00

Table A.3 Focal mechanism data for the Biga Peninsula region(Heidbach et al., 2008; International Seismological Centre, 2011).

EVENT_ID	AUTHOR	LAT	LON	DEPTH	MO	MW	T_PL	T_AZM	P_PL	P_AZM	N_PL	N-AZM
SEA5758	HARVARDCMT	40.190	26.020	15.00		5.20	70.00	240.00	9.00	124.00	18.00	32.00
SEA5759	HARVARDCMT	40.170	26.170	15.00		4.70	76.00	189.00	5.00	298.00	13.00	30.00
SEA6823	HARVARDCMT	40.340	26.040	12.00		4.70	77.00	49.00	5.00	297.00	12.00	206.00
TUR123	ZANCAN1993	39.600	27.370	15.00		5.40	59.00	217.00	4.00	315.00	31.00	47.00
TUR137	KIRALO2003	40.230	26.800	11.00		5.40	64.00	169.00	15.00	293.00	21.00	29.00
TUR138	ZANCAN1993	39.500	26.350	26.00		5.10	59.00	299.00	30.00	107.00	5.00	200.00
TUR21	TAYMJA1991	40.080	27.500	5.00		5.60	14.00	77.00	7.00	345.00	74.00	230.00
TUR30	EVAXRI1988	40.330	27.400	12.00		4.90	12.00	202.00	0.00	112.00	78.00	22.00
TUR8	MCKEXX1972	40.070	27.390	0.00		7.20	75.00	209.00	4.00	103.00	14.00	15.00
TUR98	PONDET2002	39.480	27.210	10.00		4.50	41.00	293.00	46.00	137.00	12.00	34.00
1739714	AUTHOR	39.380	27.660	15.00	9.50	4.60	6.00	27.00	32.00	294.00	57.00	126.00
6993128	MED_RCMT	40.170	26.170	15.00	0.92	5.20	14.00	30.00	5.00	299.00	75.00	190.00
6993080	HRVD	40.190	26.020	15.00	4.42	5.70	18.00	31.00	9.00	124.00	70.00	239.00
1080141	HRVD	39.480	27.210	10.00	1.86	4.80	12.00	34.00	46.00	137.00	41.00	293.00
1908127	MED_RCMT	39.330	27.500	10.00	7.02	4.50	37.00	174.00	46.00	317.00	20.00	69.00
7356843	MED_RCMT	40.340	26.040	12.00	7.67	5.20	12.00	206.00	5.00	297.00	77.00	49.00
6993080	HRVD	40.400	26.120	15.00	5.21	5.70	6.00	212.00	31.00	306.00	59.00	111.00

BIBLIOGRAPHY

Aagaard, B., Kientz, S., Knepley, M., Strand, L., Williams, C., 2012. PyLith User Manual, Version 1.7.1, Computational Infrastructure of Geodynamics.

Akşay, A., Şükrü, P., Gedik, I., Bilginer, E., Duru, M., Akbaş, B., Altun, I., 2002. Zonguldak, in: Şenel, M. (Ed.), Türkiye Jeoloji Haritası.

Aksu, A.E., Calon, T.J., Hiscott, R.N., 2000. Anatomy of the North Anatolian Fault Zone in the Marmara Sea, Western Turkey: Extensional Basins Above a Continental Transform. GSA Today June 2000, 5.

Aktug, B., Nocquet, J.M., Cingöz, A., Parsons, B., Erkan, Y., England, P., Lenk, O., Gürdal, M.A., Kilicoglu, A., Akdeniz, H., Tekgül, A., 2009. Deformation of western Turkey from a combination of permanent and campaign GPS data: Limits to block-like behavior. Journal of Geophysical Research: Solid Earth 114, B10404.

Akyüz, H.S., Hartleb, R., Barka, A., Altunel, E., Sunal, G., Meyer, B., Armijo, R., 2002. Surface Rupture and Slip Distribution of the 12 November 1999 Düzce Earthquake (M7.1), North Anatolian Fault, Bolu, Turkey. Bulletin of the Seismological Society of America 92, 61-66.

Allen, C., 1982. Comparisons Between the North Anatolian Fault of Turkey and the San Andreas Fault of California, in: Işikara, A.M., Vogel, A. (Eds.), Multidisciplinary Approach to Earthquake Prediction. Vieweg+Teubner Verlag, pp. 67-85.

Ambraseys, N.N., 1970. Some characteristic features of the Anatolian fault zone. Tectonophysics 9, 22.

Ambraseys, N.N., Zatopek, A., 1969. The Mudurnu Valley, West Anatolia, Turkey, earthquake of 22 July 1967. Bulletin of the Seismological Society of America 59, 68.

Andrews, D.J., 1976. Rupture propagation with finite stress in antiplane strain. Journal of Geophysical Research 81, 3575-3582.

Armijo, R., Meyer, B., Hubert, A., Barka, A., 1999. Westward Propagation of the North Anatolian Fault into the Northern Aegean: Timing and kinematics. Geology 27, 267-270.

Armijo, R., Meyer, B., Navarro, S., King, G., 2002. Slip partitioning in the Sea of marmara pull-apart: a clue to propagation processes of the North Anatolian Fault. Terra Nova 14, 80-86.

Ates, A., Kayıran, T., Sincer, I., 2003. Structural interpretation of the Marmara region, NW Turkey, from aeromagnetic, seismic and gravity data. Tectonophysics 367, 41-99.

Barka, A., Akyüz, H.S., Altunel, E., Sunal, G., Çakir, Z., Dikbas, A., Yerli, B., Armijo, R., Meyer, B., de Chabalier, J.B., Rockwell, T., Dolan, J.R., Hartleb, R., Dawson, T., Christofferson, S., Tucker, A., Fumal, T., Langridge, R., Stenner, H., Lettis, W., Bachhuber, J., Page, W., 2002. The Surface Rupture and Slip Distribution of the 17 August 1999 Izmit Earthquake (M7.4), North Anatolian Fault. Bulletin of the Seismological Society of America 92, 43-60.

Barka, A.A., 1992. The North Anatolian fault zone. Annales Tectonicae (Suppl.) 6, 164-195.

Barka, A.A., 1999. The 17 August 1999 Izmit Earthquake. Science 285, 2.

Barka, A.A., Kadinsky-Cade, K., 1988. Strike-Slip Fault Geometry in Turkey and its Influence on Earthquake Activity. Tectonics 7, 663-684.

Barton, N., 2007. Rock Quality, Seismic Velocity, Attenuation and Anisotropy. Taylor & Francis/Balkema, Leiden, The Netherlands.

Barton, N.R., 1974. Review of the Shear Strength of Filled Discontinuities. Norwegian Geotechnical Institute Publication No. 105.

Bayrakci, G., Laigle, M., Bécel, A., Hirn, A., Taymaz, T., Yolsal-Çevikbilen, S., team, S., 2013. 3-D sediment-basement tomography of the Northern Marmara trough by a dense OBS network at the nodes of a grid of controlled source profiles along the North Anatolian fault. Geophysical Journal International 194, 1335-1357.

Bell, F.G., 2007. Basic Environmental and Engineering Geology. Whittles Publishing Limited, Dunbeath, Scotland.

Ben-Zion, Y., Peng, Z., Okaya, D., Seeber, L., Armbruster, J.G., Ozer, N., Michael, A.J., Baris, S., Aktar, M., 2003. A shallow fault-zone structure illuminated by trapped waves in the Karadere-Duzce branch of the North Anatolian Fault, western Turkey. Geophysical Journal International 152, 699-717.

Bilham, R., King, G., 1989. The Morphology of Strike-Slip Faults: Examples from the San Andreas Fault, California. Journal of Geophysical Research 94, 10204-10216.

Bohnhoff, M., Bulut, F., Dresen, G., Malin, P.E., Eken, T., Aktar, M., 2013. An earthquake gap south of Istanbul. Nat Commun 4.

Bohnhoff, M., Grosser, H., Dresen, G., 2006. Strain partitioning and stress rotation at the North Anatolian fault zone from aftershock focal mechanisms of the 1999 Izmit Mw= 7.4 earthquake. Geophysical Journal International 166, 12.

Boutareaud, S., Calugaru, D.-G., Han, R., Fabbri, O., Mizoguchi, K., Tsutsumi, A., Shimamoto, T., 2008. Clay-clast aggregates: A new textural evidence for seismic fault sliding? Geophysical Research Letters 35, L05302.

Bowman, D.D., King, G.C.P., 2001. Accelerating seismicity and stress accumulation before large earthquakes. Geophysical Research Letters 28, 4039-4042.

Boyd, T.M., 2003. Density Variations of Earth Materials, in: Thomas, L. (Ed.), Introduction to Geophysical Exploration, Gravity Module, University of Melbourne.

Boztepe-Güney, A., Yılmaz, Y., Demirbağ, E., Ecevitoğlu, B., Arzuman, S., Kuşçu, İ., 2001. Reflection seismic study across the continental shelf of Baba Burnu promontory of Biga Peninsula, northwest Turkey. Marine Geology 176, 75-85.

Byerlee, J., 1978. Friction of Rocks. Pageoph 116, 615-626.

Carpenter, B.M., Marone, C., Saffer, D.M., 2011. Weakness of the San Andreas Fault revealed by samples from the active fault zone. Nature Geoscience 4, 251-254.

Carpenter, B.M., Saffer, D.M., Marone, C., 2012. Frictional properties and sliding stability of the San Andreas fault from deep drill core. Geology 40, 759-762.

Chang, S., Barbot, S., Avouac, J., Lee, J., 2011. Frictional properties of the San Andreas Fault determined from dynamic modeling of afterslip. American Geophysical Union, Fall Meeting 2011 Abstract #T23C-2415.

Chéry, J., Zoback, M.D., Hassani, R., 2001. An integrated mechanical model of the San Andreas fault in central and northern California. Journal of Geophysical Research 106, 22051-22066.

Chéry, J., Zoback, M.D., Hickman, S., 2004. A mechanical model of the San Andreas fault and the SAFOD Pilot Hole stress measurements. Geophysical Research Letters 31, 1-5.

Collettini, C., Niemeijer, A., Viti, C., Marone, C., 2009. Fault zone fabric and fault weakness. Nature 462, 907-910.

Collettini, C., Sibson, R.H., 2001. Normal faults, normal friction? Geology 29, 927-930.

Davis, G.H., 1999. Structural Geology of the Colorado Plateau Region of Southern Utah, with Special Emphasis on Deformation Bands. Geological Society of America Special Papers 342, 1-157.

Davis, G.H., Reynolds, S.J., Kluth, C.F., 2012. Structural Geology of Rocks and Regions, Third ed. John Wiley & Sons, Inc., United States of America.

Dewey, J.F., Hempton, M.R., Kidd, W.S.F., Şaroğlu, F., Şengör, A.M.C., 1986. Shortening of continental lithosphere: the neotectonics of eastern Anatolia-A young collision zone. Geological Society of London, Special Publication In: Coward, M.P. & Ries, A.C. (eds.) Collision Tectonics, 3-36.

Dewey, J.F., Şengör, A.M.C., 1979. Aegean and surrounding regions: complex multiplate and continuum tectonics in a convergent zone. Geol. Soc. Am. Bull. 90, 84-92.

Di Toro, G., Hirose, T., Nielsen, S., Pennacchioni, G., Shimamoto, T., 2006. Natural and Experimental Evidence of Melt Lubrication of Faults During Earthquakes. Science 311, 647-649.

Dieterich, J., 1978. Time-dependent friction and the mechanics of stick-slip. pure and applied geophysics 116, 790-806.

Dieterich, J.H., 1979. Modeling of rock friction: 1. Experimental results and constitutive equations. Journal of Geophysical Research: Solid Earth 84, 2161-2168.

Dieterich, J.H., 1981. Constitutive Properties of Faults With Simulated Gouge, Mechanical Behavior of Crustal Rocks: The Handin Volume. American Geophysical Union, pp. 103-120.

Dooley, T., McClay, K., 1997. Analog modeling of pull-apart basins. AAPG Bulletin 81, 1804-1826.

Dresen, G., Aktar, M., Bohnhoff, M., Eyidoğan, H., 2007. Drilling the North Anatolian Fault. Scientific Drilling, 3.

DU/GSC, 2001. Database of Global Rock Properties, in: Laboratory, D.U.G.S.o.C.H.P. (Ed.), Halifax, Nova Scotia, Canada.

Ellis, S., Beavan, J., Eberhart-Phillips, D., Stöckhert, B., 2006. Simplified models of the Alpine Fault seismic cycle: stress transfer in the mid-crust. Geophysical Journal International 166, 386-402.

Ergintav, S., Burgmann, R., McClusky, S., Cakmak, R., Reilinger, R., Lenk, O., Barka, A., Ozener, H., 2002. Postseismic Deformation Near the Izmit Earthquake (08/17/1999, M=7.5) Rupture Zone. Bulletin of the Seismological Society of America 92, 194-207.

Ergün, M., Özel, E., 1995. Structural relationship between the Sea of Marmara Basin and the North Anatolian Fault Zone. Terra Nova 7, 278-288.

Faulkner, D.R., Mitchell, T.M., Healy, D., Heap, M.J., 2006. Slip on 'weak' faults by the rotation of regional stress in the fracture damage zone. Nature 444, 922-925.

Flerit, F., Armijo, R., King, G.C.P., Meyer, B., Barka, A., 2003. Slip partitioning in the Sea of Marmara pull-apart determined from GPS velocity vectors. Geophysical Journal International 154, 1-7.

Fukuyama, E., Mikumo, T., Olsen, K.B., 2003. Estimation of the Critical Slip-Weakening Distance: Theoretical Background. Bulletin of the Seismological Society of AMerica 93, 1835-1840.

Grall, C., Henry, P., Tezcan, D., Mercier de Lepinay, B., Bécel, A., Géli, L., Rudkiewicz, J.-L., Zitter, T., Harmegnies, F., 2012. Heat flow in the Sea of Marmara Central Basin: Possible implications for the tectonic evolution of the North Anatolian fault. Geology 40, 3-6.

Gülen, L., Pinar, A., Kalafat, D., Ozel, N., Horasan, G., Yilmazer, M., Isikara, A.M., 2002. Surface Fault Breaks, Aftershock Distribution, and Rupture Process of the 17 August 1999 Izmit, Turkey, Earthquake. Bulletin of the Seismological Society of America 92, 230-244.

He, J., Chéry, J., 2008. Slip rates of the Altyn Tagh, Kunlun and Karakorum faults (Tibet) from 3D mechanical modeling. Earth and Planetary Science Letters 274, 50-58.

Heidbach, O., Tingay, M., Barth, A., Reinecker, J., Kurfeß, D., Müller, B., 2008. The World Stress Map database release 2008.

Hergert, T., Heidbach, O., 2010. Slip-rate variability and distributed deformation in the Marmara Sea fault system. Nature Geoscience, 132-135.

Hergert, T., Heidbach, O., 2011. Geomechanical model of the Marmara Sea region - II. 3-D contemporary background stress field. Geophysical Journal International 185, 1090–1102.

Hergert, T., Heidbach, O., Bécel, A., Laigle, M., 2011. Geomechanical model of the Marmara Sea region - I. 3-D contemporary kinematics. Geophysical Journal International 185, 17.

Hirose, T., Shimamoto, T., 2005. Slip-Weakening Distance of Faults during Frictional Melting as Inferred from Experimental and Natural Pseudotachylytes. Bulletin of the Seismological Society of AMerica 95, 1666-1673.

Hisarli, M.Z., Çinku, M.C., Orbay, N., 2011. Paleomagnetic evidence of complex tectonic rotation pattern in the NW Anatolian region: Implications for the tectonic history since the Middle Eocene. Tectonophysics 505, 13.

Holdsworth, R.E., 2004. Weak Faults--Rotten Cores. Science 303, 181-182.

Hubert-Ferrari, A., Armijo, R., King, G.C.P., Meyer, B., Barka, A., 2002. Morphology, displacement and slip rates along the North Anatolian Fault (Turkey). Journal of Geophysical Research 107, 1-33.

Hubert-Ferrari, A., Barka, A.A., Jacques, E., Nalbant, S.S., Meyer, B., Armijo, R., Tapponnier, P., King, G.C.P., 2000. Seismic hazard in the Marmara Sea region following the 17 August 1999 Izmit earthquake. Nature Geoscience 404, 5.

Hubert-Ferrari, A., King, G., Van Der Woerd, J., Villa, I., Altunel, E., Armijo, R., 2008. Long-term evolution of the North Anatolin fault (Turkey). Geological Society of London Special publication, 42.

Ide, S., Takeo, M., 1997. Determination of constitutive relations of fault slip based on seismic wave analysis. Journal of Geophysical Research: Solid Earth 102, 27379-27391.

International Seismological Centre, 2011. On-line Bulletin, in: Cent., I.S. (Ed.), Thatcham, United Kingdom.

Jarvis, A., Reuter, H.I., Nelson, A., Guevara, E., 2008. Hole-filled seamless SRTM data v4, in: (CIAT), I.C.f.T.A. (Ed.), http://srtm.csi.cgiar.org.

Jiménez-Munt, I., Sabadini, R., Gardi, A., 2006. Active deformation in the Mediterranean from Gibraltar to Anatolia inferred from numbercal modelling and geodetic and seismological data. Journal of Geophysidcal Research 108, 1-24.

Johnson, K.M., Burgmann, R., Larson, K., 2006. Frictional Properties on the San Andreas Fault near Parkfield, California, Inferred from Models of Afterslip following the 2004 Earthquake. Bulletin of the Seismological Society of America 96, S321-S338.

Jolivet, R., Lasserre, C., Doin, M.-P., Peltzer, G., Avouac, J.-P., Sun, J., Dailu, R., 2013. Spatio-temporal evolution of aseismic slip along the Haiyuan fault, China: Implications for fault frictional properties. Earth and Planetary Science Letters 377-378, 23-33.

Karimi, B., McQuarrie, N., Lin, J.-S., in revision. Modeling estimates of static coefficients of friction and cohesion: An example from the North Anatolian Fault East of the Marmara sea. Geophysical Research Letters.

Karimi, B., McQuarrie, N., Lin, J.-S., Harbert, W., 2014. Determining the geometry of the North Anatolian Fault East of the Marmara Sea through integrated stress modeling and remote sensing techniques. Tectonophysics 623, 14-22.

Kasapoglu, K.E., Toksöz, M.N., 1983. Tectonic consequences of the collision of the Arabian and Eurasian plates: Finite element models. Tectonophysics 100, 71-95.

King, G., 1986. Speculations on the Geometry of the Initiation and Termination Processes of Earthquake Rupture and its Relation to Morphology and Geological Structure. Pageoph 124, 567-585.

King, G., Nábëlek, J., 1985. Role of Fault Bends in the Initiation and Termination of Earthquake Rupture. Science 228, 984-987.

Kiratzi, A.A., 2002. Stress tensor inversions along the westernmost North Anatolian Fault Zone and its continuation into the North Aegean Sea. Geophysical Journal International 151, 360-376.

KOERI-UDIM, 2012. Historical Earthquakes Catalog, in: Centre, B.U.K.O.a.E.R.I.-N.E.M. (Ed.), Istanbul, Turkey.

Konak, N., 2002. Izmir, in: Şenel, M. (Ed.), Türkiye Jeoloji Haritası.

Koulakov, I., Bindi, D., Parolai, S., Grosser, H., Milkereit, C., 2010. Distribution of Seismic Velocities and Attenuation in the Crust beneath the North Anatolian Fault (Turkey) from Local Earthquake Tomography. Bulletin of the Seismological Society of America 100, 207-224.

Kröner, A., Stern, R.J., 2004. Pan-African Orogeny. Encyclopedia of Geology 1, 1-12.

Lachenbruch, A.H., Sass, J.H., 1980. Heat-flow and energetics of the San Andreas fault zone. Journal of Geophysical Research 85, 6185-6222.

Le Pichon, X., Chamot-Rooke, N., Rangin, C., Şengör, A.M.C., 2003. The North Anatollian Fault in the Sea of Marmara. Journal of Geophysical Research 108, 2179-2198.

Le Pichon, X., İmren, C., Rangin, C., Şengör, A.M.C., Siyako, M., 2014. The South Marmara Fault. International Journal of Earth Sciences 103, 219-231.

Le Pichon, X., Şengör, A.M.C., Demirbağ, E., Rangin, C., İmren, C., Armijo, R., Görür, N., Çağatay, N., Mercier de Lepinay, B., Meyer, B., Saatçılar, R., Tok, B., 2001. The active Main Marmara Fault. Earth and Planetary Science Letters 192, 595-616.

Lesne, O., Calais, E., Deverchére, J., 1998. Finite element modelling of crustal deformation in the Baikal rift zone: new insights into the active-passive rifting debate. Tectonophysics 289, 327-340.

Lockner, D.A., Morrow, C., Moore, D., Hickman, S., 2011. Low strength of deep San Andreas fault gouge from Safod core. Nature 472, 82-85.

Marone, C., Kilgore, B., 1993. Scaling of the critical slip distance for seismic faulting with shear strain in fault zones. Nature 362, 618-621.

McClusky, S., Balassanian, S., Barka, A., Demir, C., Ergintav, S., Georgiev, I., Gurkan, O., Hamburger, M., Hurst, K., Kahle, H., Kastens, K., Kekelidze, G., King, R., Kotzev, V., Lenk, O., Mahmoud, S., Mishin, A., Nadariya, M., Ouzounis, A., Paradissis, D., Peter, Y., Prilepin, M., Reilinger, R., Sanli, I., Seeger, H., Tealeb, A., Toksöz, M.N., Veis, G., 2000. Global Positioning System constraints on plate kinematics and dynamics in the eastern Mediterranean and Caucasus. Journal of Geophysical Research: Solid Earth 105, 5695-5719.

McElfresh, S.B.Z., Harbert, W., Ku, C.-Y., Lin, J.-S., 2002. Stress modeling of tectonic blocks at Cape Kamchatka, Russia using principal stress proxies from high-resolution SAR: new evidence for the Komandorskiy Block. Tectonophysics 354, 239-256.

McKenzie, D., Jackson, J., 1983. The relationship between strain rates, crustal thickening, palaeomagnetism, finite strain and fault moments within a deforming zone. Earth and Planetary Science Letters 65, 182-202.

McQuarrie, N., Stock, J.M., Verdel, C., Wernicke, B.P., 2003. Cenozoic evolution of neothethys and implicaitons for the causes of plate motions. Geophysical Research Letters 30.

Mikumo, T., Olsen, K.B., Fukuyama, E., Yagi, Y., 2003. Stress-Breakdown Time and Slip-Weakening Distance Inferred from Slip-Velocity Functions on Earthquake Faults. Bulletin of the Seismological Society of AMerica 93, 264-282.

Moore, D.E., Rymer, M.J., 2007. Talc-bearing serpentinite and the creeping section of the San Andreas fault. Nature 448, 795-797.

Muhuri, S.K., Dewers, T.A., Scott, T.E.J., Reches, Z.e., 2003. Interseismic fault strengthening and earthquake-slip instability: Friction or cohesion? Geology 31, 881-884.

Muller, J.R., Aydin, A., Maerten, F., 2003. Investigating the transition between the 1967 Mudurnu Valley and 1999 Izmit earthquakes along the North Anatolian fault with static stress changes. Geophysical Journal International 154, 11.

Neugebauer, J., Löffler, M., Berkhemer, H., Yatman, A., 1997. Seismic observations at an overstep of the western North-Anatolian Fault (Abant-Sapanca region, Turkey). International Journal of Earth Sciences 86, 9.

Ohnaka, M., 1992. Earthquake source nucleation: A physical model for short-term precursors. Tectonophysics 211, 149-178.

Okay, A.I., Demirbağ, E., Kurt, H., Okay, N., Kuşçu, İ., 1999. An active, deep marine strike-slip basin along the North Anatolian fault in Turkey. Tectonics 18, 129-147.

Okay, A.I., Kaşlılar-Özcan, A., İmren, C., Boztepe-Güney, A., Demirbağ, E., Kuşçu, İ., 2000. Active faults and evolving strike-slip basins in the Marmara Sea, northwest Turkey: a multichannel seismic reflection study. Tectonophysics 321, 189-218.

Örgülü, G., 2011. Seismicity and source parameters for small-scale earthquakes along the splays of the North Anatolian Fault (NAF) in the Marmara Sea. Geophysical Journal International 184, 385-404.

Özalaybey, S., Ergin, M., Aktar, M., Tapırdamaz, C., Biçmen, F., Yörük, A., 2002. The 1999 Izmit Earthquake Sequence in Turkey: Seismological and Tectonic Aspects. Bulletin of the Seismological Society of AMerica 82, 376-386.

Ozener, H., Dogru, A., Unlutepe, A., 2009. An Approach for Rapid Assessment of Seismic Hazards in Turkey by Continuous GPS Data. Sensors 9, 602-615.

Öztürk, K., Yaltirak, C., Alpar, B., 2009. The Relationship Between the Tectonic Setting of the Lake Iznik Basin and the Middle Strand of the North Anatolian Fault. Turkish Journal of Earth Sciences 18, 209-224.

Palyvos, N., Pantosti, D., Zabci, C., D'Addezio, G., 2007. Paleoseismological Evidence of Recent Earthqaukes on the 1967 Mudurnu Valley Earthquake Segment of the North Anatolian Fault. Bulletin of the Seismological Society of America 97, 15.

Pantosti, D., Pucci, S., Palyvos, N., De Martini, P.M., D'Addezio, G., Collins, P.E.F., Zabci, C., 2008. Paleoearthquakes of the Düzce fault (North Anatolian Fault Zone): Insights for large surface faulting earthquake recurrence. Journal of Geophysical Research 113, 1-20.

Parke, Minshull, Anderson, White, McKenzie, Kuşçu, Bull, Görür, Şengör, 1999. Active faults in the Sea of Marmara, western Turkey, imaged by seismic reflection profiles. Terra Nova 11, 223-227.

Parke, J.R., White, R.S., McKenzie, D., Minshull, T.A., Bull, J.M., Kuşçu, I., Görür, N., Şengör, C., 2002. Interaction between faulting and sedimentation in the Sea of Marmara, western Turkey. Journal of Geophysical Research: Solid Earth 107, 2286.

Parsons, T., 2004. Recalculated probability of M ≥ 7 earthquakes beneath the Sea of Marmara, Turkey. Journal of Geophysical Research 109.

Provost, A.-S., Chéry, J., Hassani, R., 2003. 3D mechanical modeling of the GPS velocity field along the North Anatolian fault. Earth and Planetary Science Letters 209, 361-377.

Rabinowicz, E., 1951. The Nature of the Static and Kinetic Coefficients of Friction. Journal of Applied Physics 22, 1373-1379.

Rangin, C., Le Pichon, X., Demirbag, E., Imren, C., 2004. Strain localization in the Sea of Marmara: Propagation of the North Anatolian Fault in a now inactive pull-apart. Tectonics 23, TC2014.

Reilinger, R., McClusky, S., Vernant, P., Lawrence, S., Ergintav, S., Cakmak, R., Ozener, H., Kadirov, F., Guliev, I., Stepanyan, R., Nadariya, M., Hahubia, G., Mahmoud, S., Sakr, K., ArRajehi, A., Paradissis, D., Al-Aydrus, A., Prilepin, M., Guseva, T., Evren, E., Dmitrotsa, A., Filikov, S.V., Gomez, F., Al-Ghazzi, R., Karam, G., 2006. GPS constraints on continental deformation in the Africa-Arabia-Eurasia continental collision zone and implications for the dynamics of plate interactions. Journal of Geophysical Research: Solid Earth 111, B05411.

Rice, J.R., Tse, S.T., 1986. Dynamic motion of a single degree of freedom system following a rate and state dependent friction law. Journal of Geophysical Research: Solid Earth 91, 521-530.

Riedel, W., 1929. Zur Mechanik geologischer Bruscherscheinungen: ein Beitrag zum Problem der "Fiederspälten". Centralblatt für Mineralogie, Geologie, und Paleontologie Part B, 14.

Scawthorn, C., Johnson, G.S., 2000. Preliminary report: Kocaeli (Izmit) earthquake of 17 August 1999. Engineering Structures 22, 727-745.

Scholz, C.H., 1988. The critical slip distance for seismic faulting. Nature 336, 761-763.

Schwartz, D.P., Coppersmith, K., 1986. Seismic hazards: new trends in analysis using geologic data. Active Tectonics, 215-230.

Şengör, A.M.C., 1979. The North Anatolian Transform Fault: its age, offset and tectonic significance. J. Geol. Soc. London 136, 269-282.

Sengor, A.M.C., Canitez, N., 1982. The North Anatolian fault, Alpine-Mediterranean Geodynamics. AGU, Washington, DC, pp. 205-216.

Şengör, A.M.C., Canıtez, N., 1982. The North Anatolian Fault, Boulder, CO: Geol. Soc./Washington, DC: Am. Geophys. Union.

Şengör, A.M.C., Görür, N., Şaroğlu, F., 1985. Strike-slip faulting and related basin formation in zones of tectonic escape: Turkey as a case study.

Şengör, A.M.C., Grall, C., İmren, C., Le Pichon, X., Görür, N., Henry, P., Karabulut, H., Siyako, M., 2014. The geometry of the North Anatolian transform fault in the Sea of Marmara and its temporal evolution: implications for the development of intracontinental transform faults1. Canadian Journal of Earth Sciences 51, 222-242.

Şengör, A.M.C., Natal'in, B.A., 1996. Turkic-Type Orogeny and its Role in the Making of the Continental Crust. Annual Review of Earth and Planetary Sciences 24, 263-337.

Şengör, A.M.C., Tüysüz, O., İmren, C., Sakinç, M., Eyidoğan, H., Görür, N., Le Pichon, X., Rangin, C., 2005. The North Anatolian Fault: A New Look. Annual Review of Earth and Planetary Sciences 33, 37-112.

Sibson, R.H., 1986. Earthquakes and Lineament Infrastructure. Philosophical Transactions of the Royal Society 317, 63-79.

Sibson, R.H., 1994. An assessment of field evidence for 'Byerlee' friction. pure and applied geophysics 142, 645-662.

Slemmons, D.B., Depolo, C.M., 1986. Evaluation of active faulting and associated hazards. Studies in geophysics—active tectonics: National Academy Press, Washington, DC, 45-62.

Sorlien, C.C., Akhun, S.D., Seeber, L., Steckler, M.S., Shillington, D.J., Kurt, H., Çifçi, G., Poyraz, D.T., Gürçay, S., Dondurur, D., İmren, C., Perinçek, E., Okay, S., Küçük, H.M., Diebold, J.B., 2012. Uniform basin growth over the last 500ka, North Anatolian Fault, Marmara Sea, Turkey. Tectonophysics 518–521, 1-16.

Stein, R.S., Barka, A.A., Dietrich, J.H., 1997. Progressive failure on the North Anatolian fault since 1939 by earthquake stress triggering. Geophysical Journal International 128, 594-604.

Straub, C., Kahle, H.-G., Schindler, C., 1997. GPS and geologic estimates of the tectonic activity in the Marmara Sea region, NW Anatolia. Journal of Geophysical Research 102, 15.

Tembe, S., Lockner, D.A., Solum, J.G., Morrow, C.A., Wong, T.-f., Moore, D.E., 2006. Frictional strength of cuttings and core from SAFOD drill hole phases 1 and 2. Geophysical Research Letters 33, L23307.

Tenthorey, E., Cox, S.F., 2006. Cohesive strengthening of fault zones during the interseismic period: An experimental study. Journal of Geophysical Research 111, 1-14.

Tsutsumi, A., Shimamoto, T., 1997. High-velocity frictional properties of gabbro. Geophysical Research Letters 24, 699-702.

Tullis, T., Weeks, J., 1986. Constitutive behavior and stability of frictional sliding of granite. pure and applied geophysics 124, 383-414.

Türkecan, A., Yurtsever, A., 2002. Istanbul, in: Şenel, M. (Ed.), Türkiye Jeoloji Haritası.

USGS, 2008. GLSDEM tile for N040_E030, Global Land Survey Digital Elevation Model (GLSDEM). Global Land Cover Facility, University of Maryland, College Park, Maryland.

Wibberley, C.A.J., Shimamoto, T., 2005. Earthquake slip weakening and asperities explained by thermal pressurization. Nature 436, 689-692.

Wilcox, R.E., Harding, T.P., Seely, D.R., 1973. Basic wrench tectonics. American Association of Petroleum Geologists Bulletin 57, 22.

Wong, H.K., Lüdmann, T., Ulug, A., Görür, N., 1995. The Sea of Marmara: a plate boundary sea in an escape tectonic regime. Tectonophysics 244, 231-250.

Wyllie, D.C., 1999. Foundations on Rock, Second Edition ed. Routledge, New York, NY.

Yılmaz, Y., Karacık, Z., 2001. Geology of the northern side of the Gulf of Edremit and its tectonic significance for the development of the Aegean grabens. Geodinamica Acta 14, 12.

Yılmaz, Y., Tüysüz, O., Yiğitbaş, E., Genç, Ş.C., Şengör, A.M.C., 1997. Geology aned Tectonic Evolution of the Pontides, in: AAPG (Ed.), AAPG Memoir 68: Regional and Petroleum Geology of the Black Sea and Surrounding Region. AAPG, pp. 183-226.

Zoback, M.D., Zoback, M.L., Mount, V.S., Suppe, J., Eaton, J.P., Healy, J.H., Oppenheimer, D., Reasenberg, P., Jones, L., Raleigh, C.B., Wong, I.G., Scotti, O., Wentworth, C., 1987.

New Evidence on the State of Stress of the San Andreas Fault System. Science 238, 1105-1111.